FLOW BOILING HEAT TRANSFER IN A SMALL, VERTICAL, UNIFORMLY HEATED TUBE

FLOW BOILING HEAT TRANSFER IN A LONG, SMALL DIAMETER, VERTICALLY ORIENTED, UNIFORMLY HEATED TUBE

by
B.A. Statham,

A Thesis
Submitted to the School of Graduate Studies
in Partial Fulfilment of the Requirements for the Degree
M.A.Sc. in Engineering Physics

McMaster University

MASTER OF APPLIED SCIENCE (2009)
(Engineering Physics)

MCMASTER UNIVERSITY
Hamilton, Ontario, Canada

Title: Flow Boiling Heat Transfer in a Long, Small Diameter, Vertically Oriented, Uniformly Heated Tube

Author: Bradley Allan Statham, B. Eng. Society (McMaster University)

Supervisor: Dr. D.R. Novog

Number of Pages: xx, 157

Abstract

A thermalhydraulics experiment was constructed at McMaster University that is capable of measuring heat transfer data for test sections up to 1 m long at pressures up to 10.0 MPa. The test section was powered by a 96 kW DC power supply with digital control. Inlet temperature was controlled using a 40 kW RMS AC welding power supply. The experiment was pressurized using a 3.79 L bladder-type accumulator charged by a 13.8 MPa nitrogen cylinder and controlled using Swagelok pressure-reducing and back-pressure regulators. Up to 870 kPa of pump head was supplied using a Micropump GC-M25 pump.

Commissioning data was gathered using a 93.2 cm long by 4.6 mm inside diameter Inconel 600 test section at 2.0 MPa with inlet temperatures from 126–180^{o}C, representing inlet qualities of -0.2 to -0.08, and mass fluxes of 1500 and 2000 kg m^{-2} s^{-1}. Maximum outlet quality was 0.07. Heat transfer was measured using electrically isolated thermocouples 2, 4, 9, 14, 24, 34, and 44 cm from the test section outlet. Using the most reliable thermocouple 4 cm from the test section outlet, and including only data that had a heat balance error of less than $\pm 2\%$, the Petukhov-Popov and Gnielinski correlations for single phase heat transfer overpredicted experimental results with mean errors of 10.2% and 19.1% and standard deviations of ±3.0% and ±3.3% respectively. Several subcooled boiling correlations showed good predictive capability for the present results. The Thom correlation predicted subcooled boiling heat transfer 4 cm from the test section outlet particularly well with a mean error of 0.5% and a standard deviation of ±14.1%. Low mass quality saturated boiling data was predicted with a mean error of 15.3% and a standard deviation of 18.0% by the modified Chen correlation. Overall the preliminary results show good quantitative agreement with existing correlations. More data will be gathered in the near future to corroborate these results and verify the experimental capabilities at a wider range of pressures and flow rates.

The experiment will be used in the future to gather transient critical heat flux data. The experimental measurement accuracy, measurement speed, maximum inlet temperature, and flow control will be improved. This will be achieved by improving the thermocouple shielding and isolation, modifying and adding new data acquisition instrumentation, adding a heat exchanger at the test section outlet for inlet preheating, and adding an electronically controlled variac to control the pump voltage.

Acknowledgements

The author would like to acknowledge the financial support of the Natural Sciences and Engineering Research Council, Ontario Graduate Scholarships, and the University Network of Excellence in Nuclear Engineering.

I would also like to thank Dr. S.T. Yin for his advice on experimental hardware design, R. Fortman and all at Stern Laboratories for materials and calibration services, and finally my supervisor, Dr. D.R. Novog for his support and advice over the last two years.

Contents

List of Figures

List of Tables

List of Symbols

Bo	Boiling Number
Bo_*	Modified Boiling number for Klimenko's correlation
c_p	Specific heat capacity
Co	Convection Number
D	Characteristic dimension—usually inside diameter for tubular channels
f	Fanning friction factor
F	Constant paramter for Shah's saturated boiling correlation
F	Chen's two-phase convective enhancement factor
$F(M)$	Molecular weight factor from Steiner-Taborek correlation
F_{fl}	Fluid-specific multiplier for Kandlikar's subcooled boiling correlation
F_{nbf}	Nucleate boiling multiplier from Steiner-Taborek correlation
F_{pf}	Pressure multiplier from Steiner-Taborek correlation
F_{tp}	Two-phase convection multiplier from Steiner-Taborek correlation
G	Mass flux
h	Heat transfer coefficient
h_*	Kandlikar's superheat-only subcooled boiling heat transfer coefficient
h_b	Bulk fluid enthalpy

h_{bo}	Boiling heat transfer coefficient for Klimenko's correlation
h_c	Convective heat transfer coefficient for Klimenko's correlation
h_l	Liquid heat transfer coefficient; liquid mass flux only
h_L	Liquid saturation enthalpy
h_{LO}	Liquid-only heat transfer coefficient; all mass flux treated as liquid
$h_{nb,o}$	Base subcooled boiling HTC for the Steiner-Taborek correlation
h_{tp}	Two-phase heat transfer coefficient
h_V	Vapour saturation enthalpy
k	Fluid thermal conductivity
K_p	Dimensionless parameter for Klimenko's correlation
L	Axial channel length
M	Molecular weight
$nf(p_r)$	Steiner-Taborek correlation heat flux correction factor exponent
N_{cb}	Convective boiling number for Klimenko's correlation
Nu	Nusselt number
p_r	Reduced pressure; local pressure divided by critical pressure
P	Pressure
Pe_*	Modified Peclet number for Klimenko's correlation
Pr	Prandtl number
Pr_L	Prandtl number for saturated liquid
$\ddot{q}$	Heat flux
$\ddot{q}_{of}$	Steiner-Taborek base nucleate boiling heat flux
$\ddot{q}_{ONB}$	Heat flux at the onset of nucleate boiling
$\ddot{q}_{snb}$	Subcooled nucleate boiling heat flux

r_{cr}	Critical bubble radius from Steiner-Taborek correlation
R_a	Surface roughness from Steiner-Taborek correlation
Re	Reynolds number
Re_L	Reynolds number for saturated liquid mass flux only
Re_m	Modified Reynolds number for Klimenko's correlation
Re_{tp}	Two-phase Reynolds number
S	Chen's nucleate boiling suppression factor
T_b	Bulk fluid temperature
T_{sat}	Saturation temperature
u	Fluid velocity
x	Thermodynamic equilibrium mass quality
x_a	Flow quality, defined in Equation 2.2
x_{OSV}	Thermodynamic quality where OSV is reached
X_{tt}	Turbulent-liquid turbulent-vapour Martinelli parameter

Greek Letters

ρ	Density
ρ_L	Saturated liquid density
ρ_V	Saturated vapour density
ψ	Multiplication factors for the Shah correlations
σ	Surface tension
μ	Dynamic viscosity

Chapter 1

Introduction

Thermo- and fluid dynamics have been important to human beings for as long as they have existed. Animals demonstrate a primal understanding of thermodynamics when they leave the hot sun to cool off in a lake. People have been applying heuristic knowledge of thermal and fluid dynamics for as long as they have cooked with fire and travelled on waterways. The formal study of these phenomena began with the Greek philosophers and they remain open fields of inquiry whose further understanding will continue to benefit civilization [1]. Modern applications of thermal and fluid dynamics are becoming more and more specialized but are based on essential discoveries and theories formulated by scientists like Newton, Fourier, Reynolds, and Prandtl [2, 3].

Knowledge of heat transfer—heating and cooling—is essential in nearly every aspect of industrial processes. Raw materials must be heated to make steel. Tooling and workpieces must be cooled during milling and manufacturing. High-powered electronics must be cooled to prevent melting and to operate efficiently. Energy is transported from fuel to generator as heat in thermal power plants. The environments inside of buildings are controlled by heating ventilation and air conditioning (HVAC) systems. Research in thermal and fluid dynamic systems has developed in parallel with all of these and many other technologies that improve the quality of human life on Earth.

Heat transfer is especially important in nuclear power plants. Nuclear fission releases heat energy in ceramic fuel. This energy must then be transported to the turbine which drives a generator to produce electricity. The process of heat transfer in the fuel, from fuel to coolant, and from the coolant to the 'heat sink' must be understood in order to design and operate the reactor safely and efficiently. During accidents heat transfer processes are even more important. The fuel temperature must be limited to prevent the release of fission products and prevent damage to the reactor. Heat transfer processes place limits for the safe operation of nuclear power plants.

Nuclear energy is capable of providing large quantities of clean, carbon-dioxide emission free electricity. It currently provides over 50% of the electricity in Ontario on average. As evidence mounts in support of climate change due to anthropogenic emissions consumers will turn to electrically powered vehicles and utilities may opt to close coal-fired generating stations. Continued improvement in the safety of nuclear power plants is essential to minimize risk to public health and maintain public and government support for this reliable energy source as existing plants age and new ones are built. The heat transfer research presented in this thesis is highly relevant to improving the safety analysis and design of nuclear power plants.

Heat refers to thermal energy *being transported* through or between different physical mediums. Thermal energy is the kinetic energy due to the motion of the molecular constituents of a medium along 1 or more of their degrees of freedom including translation, vibration, and rotation. Most often heat transfer is studied at the macroscopic level—a scale which can nominally be seen with the naked eye. In this case a continuum mechanics approach can be taken and whole, statistical populations of particles can be observed that have continuum thermodynamic properties like temperature, pressure, or heat capacity.

Thermal energy can be transported in three fundamental ways: ***radiation***, ***conduction***, and ***convection***. These concepts are covered in the introduction to [2]. In all three cases, in the absence of external drivers, heat moves from mediums with high temperature to those with low temperature. In convection, the heat transferred per unit area or *heat flux* is directly proportional to the difference in temperature and the *heat transfer coefficient* (HTC). This is expressed mathematically as 'Newton's Law of Cooling' shown in Equation 1.1.

$$\ddot{q} = h(T_w - T_b) \tag{1.1}$$

The heat transfer coefficient is a complex function of fluid properties—that are themselves dependent upon pressure and internal energy—and the fluid kinematics in the vicinity of the heated surface. Except in a few exceptional cases they cannot be derived from theory and must be calculated using empirical correlations fitted to experimental data.

This thesis presents new experimental results from a convective heat transfer experiment that was constructed as part of the author's Master's research. Pure water was pumped through an electrically heated Inconel 600 tube with an internal diameter of 4.6 mm. The test section was was operated with an outlet pressure of

2.0 MPa with inlet mass fluxes from 1500 to 2000 $\frac{kg}{m^2 s}$ and inlet flow qualities from -0.20 to -0.08. Data was collected for single phase heat transfer, subcooled (nucleate) boiling heat transfer, and saturated boiling heat transfer. Future experiments will measure critical heat flux (CHF) and post-dryout (PDO) heat transfer.

The experimental facility is being developed to remedy a perceived lack of experimental heat transfer and CHF data for tubes with diameters less than 8 mm and CHF data for all sizes of tubes at intermediate pressures [4, 5, 6, 7]. In some cases data has been gathered for small tubes but the experiments were performed using a refrigerant as the working fluid [8, 5]. In order to use these data for applications using water—or any other fluid—a fluid-to-fluid modeling technique must be used—which adds an additional level of uncertainty [9].

More robust experimental heat transfer and CHF data for small tubes and low to medium pressures is important for several reasons. The effect of tube diameter—while keeping other parameters constant—on CHF is significant [10]. There is a large amount of CHF data available for pressures of 6.9 MPa (1000 psi) and above—the nominal operating range of most nuclear power plants. Data for low and medium pressures are needed because accidents may result in transients to lower pressures or occur while the reactor is at low pressure during a shut down.

Power, flow, and pressure transients may occur during potential nuclear reactor accidents; the experimental facility described herein has been designed to capture transient data. Depending on the type of accident these transients may occur independently of one another or simultaneously. Comparing the results of very fundamental experiments to the output of the thermalhydraulic system codes used in the nuclear industry will demonstrate how well they are able to predict the interactions of these phenomena. Details of the design and construction of the experimental apparatus are presented in Chapter 3.

1.1 Background

1.1.1 Modes of Convection Heat Transfer

Forced convection means that the fluid heat transfer medium is being driven through the heated channel by a mechanical force. The mechanical force is often a pressure gradient along the longitudinal axis of the channel that is generated by a pump. For a given fluid, geometry, and set of thermal boundary conditions steeper pressure gradients will generally result in higher average fluid velocities and more rapid transport of thermal energy from the channel. In contrast, fluid motion is generated by buoyancy forces during *free* or *natural* convection. Cooler, denser fluid is drawn downward by gravity. This results in a flow pattern as fluid is heated, rises, then cools and sinks. Free and forced convection heat transfer are covered in detail in [2].

Single phase flow means simply that only one phase—gas or liquid but not both—of one type of fluid is present. In *boiling* fluids the heated surface temperature is sufficiently high that vapour is generated. Boiling can occur even if the mean or 'bulk' fluid temperature is not yet at the boiling point or 'saturation temperature' for a given pressure. To extend this definition a *multiphase* flow could refer to anything from the gas and liquid phases of a single fluid flowing together, boiling or not, to the flow of multiple different gases, liquids, and solids together. For the remainder of this thesis 'boiling' will refer to flows where vapour is being generated from a single species of fluid. Two-phase flow refers to the flow of the liquid and gas phases of a single species flowing together regardless of whether or not vapour is being generated. Collier has written a definitive reference on forced convection boiling and condensation in channels [11]. The physics of liquid-vapour interfaces and phase change is covered in detail in Carey [12].

Heat transfer in single and multiphase flows is often estimated using correlations of experimental data based on dimensionless parameters. These are usually in the form of an expression that relates fluid properties and other system parameters to the dimensionless temperature gradient at the interface between the heated surface and the fluid called the Nusselt number, *Nu*. The Nusselt number is defined in Equation 1.2. The thermal conductivity is evaluated at the bulk fluid temperature at a given axial position.

$$Nu = \frac{hD}{k_b} \tag{1.2}$$

Convection is a complex phenomena that involves both fluid properties like thermal conductivity that vary non-linearly with presure and temperature and fluid kinematics that are nearly infinitely variable. In two- and multi-phase flows this is further complicated by interphase thermodynamic disequilibrium, discontinuities in fluid properties, and discontinuities in momentum forces between the different phases. As a result heat transfer coefficients cannot, in most caes, be easily or accurately predicted without using empirical correlations based on experimental results.

1.1.2 Momentum and Thermal Boundary Layers

In forced convection heat is transported into the fluid from a heating surface and then convected away with the fluid as it travels through and leaves the channel. At the heating surface there is friction between the solid wall and the fluid. In the vast majority of cases a 'no-slip' boundary condition is used at the wall whereby $u(y) = 0$ when $y = 0$ where u is the velocity as a function of distance from the wall, y.

Single-phase flows are nominally separated into two regimes: laminar and turbulent with a transition region in between. In the former case the momentum forces are relatively 'small' and the viscous forces are sufficient to damp out small scale velocity fluctuations. The Reynolds number *Re*, shown in Equation 1.3, is a dimensionless ratio of momentum forces to viscous forces that is used to characterize flows as either laminar or turbulent, or in the transition regime. Single phase flow regime transition criteria are shown in Table 1.1.

$$Re = \left(\frac{\rho u D}{\mu}\right) \tag{1.3}$$

$0 < Re \leq 2300$	Laminar Flow
$2300 < Re \leq 10^5$	Transition Region
$10^5 < Re$	Turbulent Flow

Table 1.1: Nominal single phase internal flow laminar-turbulent transition criteria

Turbulent flows are formed when viscous forces are unable to damp perturbations to laminar flow. Turbulent flows are characterized by 'random' 3-dimensional velocity fluctuations at the macroscopic level and very strong 'mixing' of the fluid in the bulk flow. In turbulent flow there is a small region near the wall where the fluid velocity is small. This region near the wall in turbulent flow is a laminar 'sub-region' of what is called the 'boundary layer' that must be treated separately from the bulk turbulent flow.

The boundary layer mentioned above is called the 'momentum' boundary layer where the fluid velocity develops near the wall. The fluid velocity as a function of distance from the wall can be related to the viscous shear stress by Newton's law of viscosity shown in Equation 1.4. The shear stress can be thought of as the 'friction' between infinitely thin concentric layers of fluid.

$$\tau = \mu \frac{\partial u}{\partial y} \tag{1.4}$$

There is also a 'thermal' boundary layer where the temperature as a function of distance from the heated wall changes rapidly. The fluid has a near-uniform temperature outside the thermal boundary layer and, for turbulent flow, a near-uniform velocity outside the momentum boundary layer. The Prandtl number, shown in Equation 1.5, is a dimensionless ratio of the effectiveness of momentum to thermal transport properties, represented by the dynamic viscosity and thermal conductivity respectively. The Prandtl number, Pr, is an indicator of the relative 'thicknesses' of the momentum and thermal boundary layers.

$$Pr = \left(\frac{c_p \mu}{k}\right) \tag{1.5}$$

In turbulent flow the boundary layer is crucial to the understanding of convective heat transfer. Heat is 'conducted' through the laminar sublayer and transported away by the bulk turbulent flow. The fluid velocity profile becomes flattened in the centre. This is shown in Figure 1.1. As *Re* increases and the velocity profile flattens the boundary layer becomes thinner. The thermal resistance of the smaller boundary layer is reduced and heat is more quickly transported to the turbulent bulk flow. As a result, heat transfer from the wall is increased. Schetz provides a thorough introduction to boundary layer theory in [3].

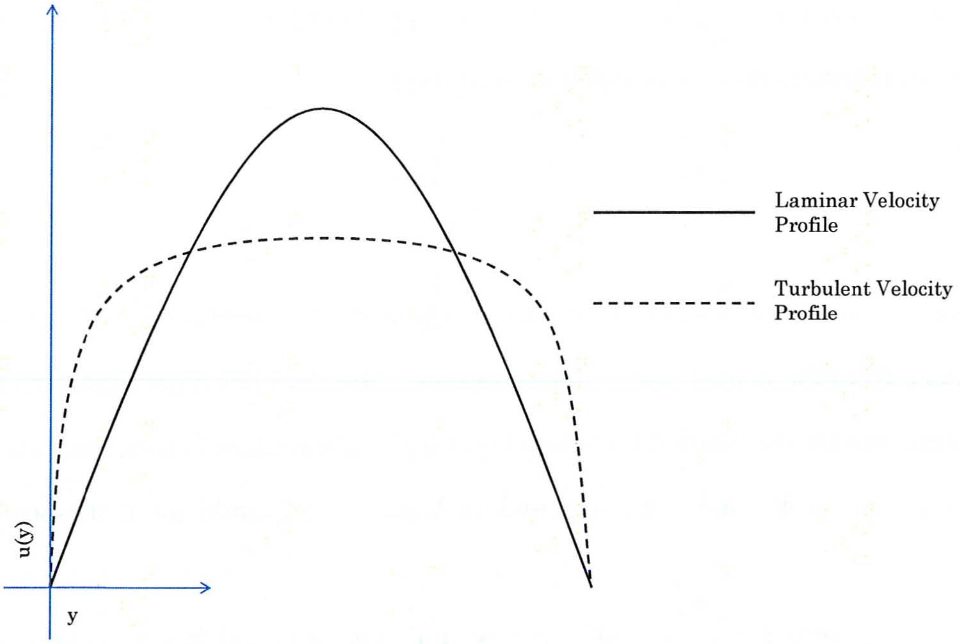

Figure 1.1: Laminar and Turbulent velocity profiles for pipe flow

1.1.3 Boiling in Convection

In order for boiling to occur on a heated surface several conditions must be met: the wall temperature must exceed the saturation temperature of the fluid at the local pressure. If the heat flux—the heat energy per unit area normal to the heated surface—is sufficiently high boiling will occur near the heated wall even if the bulk temperature of the fluid is lower than the saturation temperature—or 'subcooled.'

Second, there must be small 'pores' in the heated surface called 'nucleation sites' where vapour 'seeds' can form vapour bubbles. Nucleation at a heated surface at these sites is called 'heterogeneous' nucleation. This can occur at relatively low wall superheats–when the wall temperature exceeds the saturation temperature by a small amount. Otherwise boiling will not occur until 'homogeneous' nucleation—spontaneous generation of vapour bubbles in the midst of the fluid—is initiated which is unlikely until the bulk fluid temperature far exceeds the saturation temperature.

Boiling in convection is associated with heat transfer rates up to double or triple those of single phase turbulent convection heat transfer. Several properties of boiling flow contribute to these high heat transfer rates. Nucleating bubbles leave a turbulent wake behind them when they detach from the surface. This turbulent mixing in the near-wall boundary layer enhances heat transfer—see [13] for more on single phase turbulent mixing and [14] on boiling enhancement of near-wall turbulent mixing. Secondly, a significant amount of energy, called the *latent heat of vapourisation* (h_{LV}) is required for a liquid to change phase into vapour. The energy content of vapour is much higher than that of liquid despite the fact that at the saturation point they have the same temperature. Latent heat allows for very high quality energy to be transported efficiently away from the heated surface.

Finally, when there is bulk vapour generation and total mass flux is constant—vapour does not condense in the bulk liquid because it is saturated—vapour may be accelerated to very high velocities. The degree of vapour acceleration depends on many factors including but not limited to the local void fraction and the ratio of the liquid and vapour densities. The high vapour velocities increase turbulent mixing and the mean velocity of the of the two-phase mixture significantly. These phenomenon enhance saturated forced convective heat transfer.

1.1.4 Two-Phase Flow Regimes

As mentioned above two-phase flows are complex because of the presence not only of two phases with different properties but also the interfaces between them. Depending on the relative amount of each phase and the relative values of their thermodynamic properties the size and distribution of the interface(s) between phases can change drastically.

The vapour *quality* or mass fraction is a measure of the fraction of the total mass flow made up by vapour. Its definition, at thermodynamic equilibrium, is shown in Equation 1.6 where *h* represents the fluid enthalpy in $\frac{kJ}{kg}$.

$$x = \frac{h_b - h_L}{h_{LV}} \tag{1.6}$$

Although thermodynamically $0 \leq x \leq 1$ it is often extended to negative values to indicate the level of subcooling below the liquid saturation enthalpy. In addition, even though the bulk fluid may be subcooled there may be vapour present due to nucleation in this case the thermodynamic or 'equilibrium' quality is still negative but the flow quality, x_a, at some points in the flow field may be positive [15].

Similarly, the *void fraction* refers to the area fraction of vapour at the local cross section of a channel. The void fraction can only be estimated 'analytically' for homogeneous flow—where the liquid and vapour phases flow with the same velocity and temperature—at thermodynamic equilibrium. Thermodynamic equilibrium rarely exists in flows that are being heated or cooled and liquid-vapour phase homogeneity is a stylized approximation that is only valid for a narrow range of parameters. Void fraction is, like heat transfer, a very complex phenomenon in two-phase flows that is related to many thermo- and fluid dynamic properties. It is usually estimated using empirical correlations based on experimental data.

As liquid and vapour velocities within two-phase flows change, the liquid-vapour interfaces take on characteristic structures called flow regimes. For vertical upward flow the flow regimes include: bubbly flow, slug flow, churn flow, annular flow and drop flow [16]. In diabatic flow the flow regime can vary in the axial direction as the void fraction increases so that two or more of these flow regimes may be observed in a single channel. Each of the flow regimes that may be present in vertical upward co-current flow is described below and shown in Figure 1.2.

Bubbly flow: Bubbly flow contains many small uniformly distributed vapour bubbles that travel at a higher velocity than the bulk liquid. In subcooled boiling vapour bubbles are distributed mostly near to the wall before they condense in the bulk liquid.

Slug flow: In slug flow vapour bubbles coalesce and create large ‘slugs’ of vapour. The ‘slugs’ travel at high velocity through the centre of the channel at regular intervals leaving a layer of liquid on the surface as they pass. A turbulent wake of bubbly flow may follow each slug before the next one passes. Flow reversal may take place in the liquid film as the slug passes before it is drawn into the slug bubble’s wake.

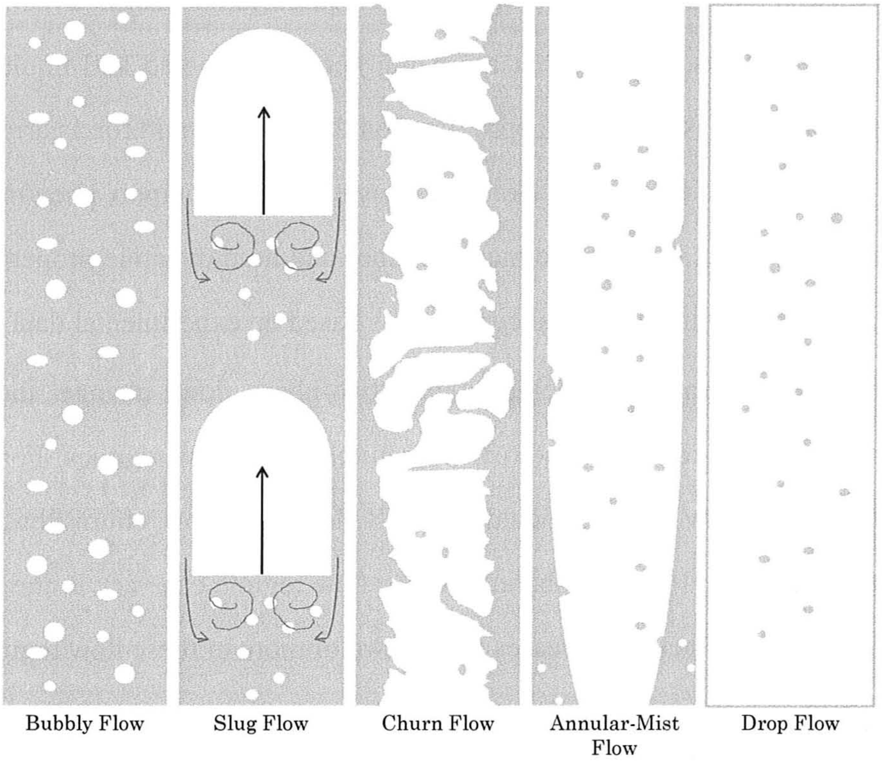

Figure 1.2: Two Phase Flow Regimes

Churn flow: Churn flow is similar to slug flow in some ways. In churn flow the bubbles may be significantly elongated and irregularly sized. The liquid-vapour interface betweeen the fluid on the wall and the vapour in the centre is very violent and contains many disturbance waves. The vapour core may contain many entrained droplets and liquid film flow may be reversed.

Annular flow: In the annular flow regime there is a 'core' of vapour flowing at high velocity in the centre of the channel surrounded by a liquid film on the channel surface. The liquid-vapour interface is relatively smooth. The liquid film flow direction is uniformly in the positive axial direction. Irregular perturbations of the interface cause waves to be 'ripped' into the vapour core resulting in entrained droplets. These disturbances are rapidly damped [17]. When there are entrained droplets in the vapour core this flow regime is described as 'annular mist' flow.

Drop flow: Drop flow can be visualized as an inverse to bubbly flow. All of the remaining liquid flows as droplets entrained in the vapour core. The channel wall or heated surface is nominally 'dry' and free from persistent liquid.

As may be expected each of these flow regimes has different heat transfer characteristics and void fraction. This is reflected in the diversity of predictive correlations that will be described in detail in the literature review that follows in Chapter 2. Usually flow boiling heat transfer is divided into two components that are not mutually exclusive: nucleate boiling and convective boiling.

In subcooled and saturated nucleate boiling the flow regime is bubbly. When the liquid film in annular flow is thin the heat transfer can be thought of as pure convective boiling at the liquid-vapour interface. In slug flow, churn flow, and annular flows where the thermal resistance of the liquid film is high—'thick' enough to increase wall superheat to levels that permit nucleate boiling [17]—the heat transfer enhancement is a mix of these two components to varying degrees depending on the local conditions.

1.2 Outline

Chapter 1 introduces the topic of the thesis and provides some necessary background information on forced convection boiling heat transfer. Chapter 2 presents a literature review for turbulent convection heat transfer, subcooled boiling heat transfer, and saturated flow boiling heat transfer. In Chapter 3 the specifications for the experimental apparatus are detailed. An outline of the experimental procedure and standard operating procedure is included. Data reduction and error analysis procedures are discussed in brief. Chapter 4 presents the experimental results for single and two-phase heat transfer. The results presented in Chapter 4 are analyzed and discussed in Chapter 5. Conclusions, suggestions for future research, and contributions to knowledge are included as Chapter 6.

Chapter 2

Literature Review

Due to the complexities outlined in Section 1.1 it requires significant computational effort to physically model convection heat transfer processes. In some cases it may not be feasible at all. This is especcially true of flow boiling. No mechanistic models of nucleate boiling exist except at very fundamental levels [18]. One-dimensional empirical correlations are often used to predict wall temperatures and pressure drop in engineering applications. Correlations can provide relatively accurate estimates of pressure gradients and heat transfer coefficients with less computational cost than a full thermo-fluid dynamic model. The applications of the empirical correlations are limited by the validity of the data they are based on.

The following sections contain reviews of the literature for single-phase turbulent convection, subcooled flow boiling, and saturated flow boiling.

Author(s) ***Year***	**Form of Correlation**	**Parametric Ranges**
Dittus and Boelter *1930*	$Nu = 0.023Re^{0.8}Pr^{0.4}$	$10^4 < Re$ $0.7 \leq Pr \leq 160$ $10 > (\frac{L}{D})$
Petukhov and Popov *1963*	$Nu = \frac{\frac{f}{8}RePr}{k_1(f)+k_2(Pr)\sqrt{\frac{f}{8}}(Pr^{\frac{2}{3}}-1)}$ $k_1(f) = 1 + 3.4f$ $k_2(Pr) = 11.7 + \frac{1.8}{Pr^{\frac{2}{3}}}$ $f = (1.82log_{10}(Re) - 1.64)^{-2}$	$10^4 < Re < 5 \times 10^6$ $0.1 < Pr < 2000$
Gnielinski *1976*	$Nu = \frac{\frac{f}{8}(Re-1000)Pr}{1+12.7\sqrt{\frac{f}{8}}(Pr^{\frac{2}{3}}-1)}K_1K_2$ $K_1 = 1 + (\frac{D}{L})^{\frac{2}{3}}$ $K_2 = \left(\frac{Pr}{Pr_w}\right)^{0.11}$ $f = (1.82log_{10}(Re) - 1.64)^{-2}$	$2300 < Re < 5 \times 10^6$ $0.1 < Pr < 2000$

Table 2.1: Single Phase Turbulent Heat Transfer Correlations

2.1 Single-Phase Turbulent Convection

By far the most widely used and cited correlation for predicting heat transfer coefficients in single phase turbulent flow is the Dittus-Boelter correlation from 1930, in the form first presented by McAdams [19]. The form of this correlation, and all other single phase turbulent convection correlations discussed in this section, is shown in Table 2.1. This correlation was empirically derived from data for tubular automotive radiators. It remains popular because of its simplicity, wide range of applicability, and reasonable accuracy which is usually estimated at $\pm$ 25% [2].

Petukhov and Popov's 1963 correlation provides a significant improvement in accuracy with a slight increase in complexity. The increase in cost is modest–the turbulent friction factor and two constants that are functions of Pr must be calculated. They derived a mostly analytic expression for the heat transfer coefficient that took into consideration the variation of fluid properties as a function of distance from the wall. Their solution assumed that the enthalpy gradient in the energy conservation equation and the pressure and momentum gradient in the conservation of momentum equation were constant over the cross section normal to any axial position. They then fitted their analytic expression to a dimensionless correlation, shown in Table 2.1, using contant physical properties. For $0.5 \leq Pr \leq 200$ and $10^4 \leq Re \leq 5 \times 10^5$ the correlation matched the derived expression within 1% and within 1-2% for $200 \leq Pr \leq 2000$ and $5 \times 10^5 \leq Re \leq 5 \times 10^6$. For the same ranges they found the correlation predicted their experiment values within 5-6% and $<10\%$ respectively, assuming constant values for $k_1 = 1.07$ and $k_2 = 12.7$ [20].

Gnielinski modified the Petukhov and Popov correlation to extend it to flows in the laminar-turbulent transition region with $2300 \leq Re \leq 10^4$. Gnielinski also added correction factors for shorter tubes to account for entrance effects and very high radial fluid temperature gradients. Gnielinksi states that "nearly 90% of the approximately 800 experimental values ... differ by less than ± 20[%]from the calculated values" [21].

In a recent investigation of heat transfer in laminar, transition, and turbulent flow Abraham, Sparrow, and Tong proposed a new correlation for $2300 \leq Re \leq 3100$ but recommended the Gnielinski correlation for $Re > 3100$ [22].

2.2 Subcooled Boiling Convection Heat Transfer

Boiling at the surface is possible when the temperature of a heated surface exceeds the saturation temperature at the local conditions of the fluid. The degree to which

Author(s) ***Year***	**Form of Correlation**	**Parametric Ranges**
Jens and Lottes *1951*	$h_{tp} = \frac{\ddot{q}}{(T_w - T_{sat}) + (T_{sat} - T_b)}$ $T_w - T_{sat} = 25\left(\frac{\ddot{q}}{1000}\right)^{0.25}\exp(-\frac{P}{6.2})$	$0.7 \le P \le 17.2MPa$ $-1.6 \le x < 0.0$ $11 \le G \le 10500\frac{kg}{m^2s}$ $3.63 \le D \le 5.74mm$ $0 < \ddot{q} \le 12500\frac{kW}{m^2}$
Thom *et al* *1965*	$T_w - T_{sat} = 22.65\left(\frac{\ddot{q}}{1000}\right)^{0.5}\exp(-\frac{P}{8.7})$	$0.5 < P \le 13.8MPa$ $-0.4 < x < 0.04$ $1000 < G < 3800\frac{kg}{m^2s}$ $5.1 \le D \le 12.7mm$ $\ddot{q} \le 2000\frac{kW}{m^2}$
Rassokhin *et al* *1970*	$T_w - T_{sat} =$ $0.304(10P)^{-\frac{1}{4}}\ddot{q}^{\frac{1}{3}}$ $0.1 < P \le 8$ MPa $T_w - T_{sat} =$ $34.7(10P)^{-\frac{4}{3}}\ddot{q}^{\frac{1}{3}}$ $8 < P \le 20$ MPa	$0.1 < P < 20MPa$
Labuntsov *1972*	$T_w - T_{sat} = \frac{1-0.045P}{3.4(10P)^{0.18}}\ddot{q}^{\frac{1}{3}}$	$0.1 < P < 20MPa$
Shah *1977*	$T_w - T_{sat} = \frac{\ddot{q}}{\psi h_L}$ $\psi = \begin{cases} \psi_o & x \le 0 \\ \psi_o + \frac{T_{sat} - T_b}{T_w - T_{sat}} & x << 0 \end{cases}$ $\psi_o =$ $\begin{cases} 230Bo^{0.5} & Bo > 0.3 \times 10^{-4} \\ 1 + 46Bo^{0.5} & Bo < 0.3 \times 10^{-4} \end{cases}$	$0.1 \le P \le 13.8MPa$ $0 \le (T_{sat} - T_b) \le 153°C$ $5.56 \le G < 24167\frac{kg}{m^2s}$ $10 \le \ddot{q} \le 22900\frac{kW}{m^2}$ $2.4 \le D \le 27.1mm$
Kandlikar *1998*	$h^* = 1058.0Bo^{0.7}F_{fl}h_{LO}$ $h^* = \frac{\ddot{q}}{T_w - T_{sat}}$ $h_{tp} = h^*\left(\frac{T_w - T_{sat}}{T_w - T_b}\right)$ $Bo = \left(\frac{\ddot{q}}{Gh_{LV}}\right)$ $F_{fl(H_2O)} = 1.0$ $h_{LO} = h_{(Petukhov-Popov)}\left(\frac{\mu_b}{\mu_w}\right)^{0.11}$	$P < 0.62MPa$

Table 2.2: Subcooled Flow Boiling Heat Transfer Correlations

the wall temperature exceeds the local saturation temperature is called superheat. When bubbles begin to form–the 'onset of nucleate boiling' or ONB–they may initially collapse or form at irregular intervals. This is called 'partial nucleate boiling.' Once boiling intensifies 'fully developed boiling' begins. The determination of heat transfer coefficients and the construction of boiling curves in the transition from partial to full nucleate boiling is discussed in more detail in Bergles and Rohsenow, Collier and Thome, Guglielmini *et al* and Kandlikar (1998) [23, 11, 24, 25].

The exact conditions at which boiling will occur have been correlated by several authors. Collier and Thome provides a review of some of these correlations in a chapter on 'Subcooled Boiling Heat Transfer' [11]. Collier indicates that the 1963 correlation of Bergles and Rohsenow–for water only–agrees with the analytical derivation of Davis and Anderson (1966). Kandlikar [25] recommends the 1961 Hsu and Graham correlation–based on a critical bubble radius and the condition that $T_L \geq T_V$ at the apex of the bubble–which agrees well with his experimental data from past publications.

Several fully-developed boiling correlations are shown in Table 2.2. The general form of the correlations is that of a wall superheat equated to a constant or pressure-dependent term multiplied by the wall heat flux raised to an exponent. It should also be noted that the wall superheat is independent of local subcooling for all correlations in Table 2.2 except that of Shah.

The Jens-Lottes correlation was based on the authors' experimental data. Collier and Thome notes that Thom *et al* found that the Jens-Lottes correlation underpredicted wall superheats for their data and modified the correlation accordingly [11]. As Kandlikar notes, Rohsenow found that while the correlation of Thom *et al* fitted data for low heat fluxes well its results were poor for high heat fluxes [26].

The Shah correlation for subcooled boiling is in the form of a multiplier for a single phase heat transfer coefficient calculated assuming the total mass flux is flowing as a liquid. The correlation was developed by fitting data on a plot of the proposed form of the correlation against the boiling number. Shah developed the initial correlation for fully developed boiling of fluids at the saturation temperature. For fluids that are near saturation, subcooling was found to have no effect. A high subcooling region, where the form of the correlation changes, was identified by plotting the ratio of subcooling to superheat against the boiling number [27].

Shah's correlation was based on approximately 500 data points from 29 data sets. The correlation fitted the data with a mean deviation of 9.5%. 97.5% of all the data were fitted within ±30%. The form of the correlation and its range of application is shown in Table 2.2.

Guglielmini *et al* conducted a review of many ONB, partial nucleate boiling, and fully developed boiling correlations in 1980. They compared each of the correlations to data in the pressure ranges 0.1-0.7 MPa, 3-4 MPa, 6-7 MPa, 13-14 MPa, and at 18.1 MPa. At low pressures most of the correlations predicted the data reasonably well but the correlations of Müller, Rassokhin *et al* and of Labuntsov provided the best results over the whole pressure range tested. None of the correlations performed well in the pressure range from 13-14 MPa and no possible explanation was given. The correlations of Rassokhin *et al* and Labuntsov are shown in Table 2.2. The correlation of Müller is not shown due to its considerable complexity with no improvement in accuracy [24].

In 1998, Kandlikar proposed a new fully developed boiling correlation based on the nucleate boiling term of his saturated boiling correlation which is discussed below. The subcooled boiling correlation is shown in Table 2.2. He demonstrated that it predicted a limited range of experimental results with various refrigerants at pressures less than 1 MPa much better than the Shah correlation for subcooled boiling. A qualitiative comparison between the Kandlikar, Shah, Thom *et al*, and Mikiç and Rohsenow correlations was also made demonstrating its goodness of fit with the 1964 data of Bergles and Rohsenow for water [25].

Kandlikar also suggests a new flow boiling regime: 'Significant Void Flow.' In this region, as the subcooled fluid approaches saturation the vapour bubbles may remain in the flow instead of condensing. He proposes this region begins when the Saha-Zuber condition for the onset of significant void 'OSV' begins [15].

$$x_{OSV} = \begin{cases} -0.0022 Bo Re_{LO} Pr_L & Re_{LO} Pr < 70000 \\ -154 Bo & Re_{LO} Pr > 70000 \end{cases} \tag{2.1}$$

The liquid-only Reynolds number, Re_{LO} is defined it Table 2.3. When the local conditions exceed the point of OSV but the fluid is not yet saturated thermodynamic disequilibrium exists. When this condition is reached the flow quality should be computed using Equation 2.2.

$$x_a = \frac{x - x_{OSV} \exp(\frac{x}{x_{OSV}} - 1)}{1 - x_{OSV} \exp(\frac{x}{x_{OSV}} - 1)} \tag{2.2}$$

The flow quality should then be applied to the nucleate boiling term of Kandlikar's saturated boiling correlation [25].

It is possible that Kandlikar's approach for the near-saturated nucleate boiling region could be applied to a saturated boiling heat transfer correlation of the user's choice. Saturated boiling correlations are discussed in the next section.

2.3 Saturated Boiling Convection Heat Transfer

Author(s) *Year*	**Form of Correlation**	**Parametric Ranges**
Chen *1966*	$h = h_{mac}F + h_{mic}S$ $h_{mac} = 0.023Re_L^{0.8}Pr_L^{0.4}\left(\frac{k_L}{D}\right)$ $Re_L = \left(\frac{GD(1-x)}{\mu_L}\right)$ $Pr_L = \left(\frac{c_{pL}\mu_L}{k_L}\right)$ $F = \left[1 + X_{tt}^{-0.5}\right]^{1.78}$ $h_{mic} = 0.00122 \left(\frac{k_L^{0.79}c_{pL}^{0.45}\rho_L^{0.49}}{\sigma^{0.5}\mu_L^{0.29}h_{LV}^{0.24}\rho_V^{0.24}}\right)(\Delta T)^{0.24}(\Delta P)^{0.75}$ $S = 0.9622 - 0.5822\left[\tan^{-1}\left(\frac{Re_{tp}}{6.18\times10^4}\right)\right]$ $Re_{tp} = F^{1.25}Re_L$ $X_{tt} = \left(\frac{1-x}{x}\right)^{0.9}\left(\frac{\rho_V}{\rho_L}\right)^{0.5}\left(\frac{\mu_L}{\mu_V}\right)^{0.1}$	$0.1 < P < 3.5MPa$ $0.06 < \bar{u}_z < 4.5\frac{m}{s}$ $0.01 < x < 0.71$ $44 < \ddot{q} < 2400\frac{kW}{m^2}$
Gungor and Winterton *1986*	$h_{tp} = Eh_l + Sh_{pool}$ $h_l = 0.023{Re_L}^{0.8}{Pr_L}^{0.4}\left(\frac{k_L}{D}\right)$ $h_{pool} = 55p_r^{0.12}(-log(p_r))^{-0.55}M^{-0.5}\ddot{q}^{0.67}$ $E = 1 + 24000Bo^{1.16} + 1.37(X_{tt})^{-0.86}$ $S = \left(1 + 1.15\times10^{-6}E^2{Re_L}^{1.17}\right)^{-1}$ $Bo = \frac{\ddot{q}}{Gh_{LV}}$ $\ddot{q}_{snb} = h_l(T_w - T_b) + Sh_{pool}(T_w - T_s)$	$0.1 \leq P \leq 7.0MPa$ $59 < G < 8180\frac{kg}{m^2s}$ $-0.5 < x < 0.7$ $4.7 < \ddot{q} \leq 4579\frac{kW}{m^2}$

Table 2.3: Two-Phase Heat Transfer Correlations—‘Additive’ forms (1)

Tables 2.3–2.5 show several saturated boiling heat transfer coefficients. The correlations in the first two tables contain ‘additive’ correlations. These correlations are expressed as the sum of nucleate boiling and two-phase convection terms. Each term nominally represents the contribution of nucleate boiling and two-phase

Author(s) ***Year***	**Form of Correlation**	**Parametric Ranges**
Steiner and Taborek *1992*	$h = ((h_{nb,o}F_{nbf})^n + (h_{LO}F_{tp})^n)^{\frac{1}{n}}$ $n = 3$ $h_{LO} =$ Liquid-only heat transfer coefficient $F_{tp} = \left[(1-x)^{1.5} + 1.9(x)^{0.6}\left(\frac{\rho_L}{\rho_V}\right)^{0.35}\right]^{1.1}$ $h_{nb,o(H_2O)} = \begin{cases} 25.58\frac{kW}{m^2} & \ddot{q} \geq \ddot{q}_{ONB} \\ 0 & \ddot{q} < \ddot{q}_{ONB} \end{cases}$ $F_{nbf} =$ $F_{pf}\left[\frac{\ddot{q}}{\ddot{q}_{of}}\right]^{nf(pr)} \times$ $\left[\frac{D}{D_o}\right]^{-0.4}\left[\frac{R_a}{R_{a,o}}\right]^{0.133} F(M)$ $F_{pf}(p_r \leq 0.95) =$ $\left\{2.816(p_r)^{0.45} + \left[3.4 + \frac{1.7}{1-(p_r)^7}\right](p_r)^{3.7}\right\}$ $\ddot{q}_{of(H_2O)} = 150\frac{kW}{m^2}$ $D_o = 0.010m$ $R_{a,o} = 1\mu m$ $nf(pr) = 0.8 - (0.1)e^{1.75p_r}$ $F(M)_{(H_2O)} = 0.72$ $\ddot{q}_{ONB} = \frac{2\sigma T_{sat}h_{LO}}{r_{cr}\rho_V h_{LV}}$ $r_{cr} = 0.3 \times 10^{-6}m$	$0.001 \leq p_r \leq 0.95$ $0 < x \leq 0.6$ $0.1D_o \leq d \leq 2D_o$ $3.5 < \left(\frac{\rho_L}{\rho_V}\right) < 5000$

Table 2.4: Two-Phase Heat Transfer Correlations—'Additive' forms (2)

convection to heat transfer. Table 2.5 contains 'conditional' correlations. These correlations are use a series of checks on the local conditions to determine the dominant mode of heat transfer and the exact form of the correlation. Most of the latter type of correlations are multipliers for single phase heat transfer coefficients. These correlations are discussed below.

Like the Dittus-Boelter corelation, the Chen (1966) correlation—shown in Table 2.3—is widely cited and recommended for use in saturated boiling flow. Chen proposed the superposition of a 'macroscopic' convective boiling component and a 'microscopic' nucleate boiling component to calculate an overall flow boiling heat transfer coefficient.

The convective boiling component was calculated using the Dittus-Boelter correlation and multiplied by an 'enhancement factor', F, to account from the enhancement to convective heat transfer due to the increased vapour velocity. Similarly the nucleate boiling component was calculated using the Forster-Zuber correlation for pool boiling and multiplied by a nucleate boiling 'suppression factor', S. The suppression factor accounted for the fact that the wall superheat may be reduced because of the effects of the enhanced convective boiling [28].

Chen compared his correlation to several experimental data sets for water and other organic fluids. The mean relative error for all data was 11.6% and varied from 8.5-15.4% for the water data. Klimenko [29] criticizes the Chen correlation for its use of the Forster-Zuber pool boiling correlation which, in the intervening years, had been shown to be dated and to be too weakly dependent on heat flux. Klimenko indicates that $h \propto \ddot{q}^{0.7}$ whereas the pool boiling model Chen used is proportional to $\ddot{q}^{0.5}$. This is consistent with the analysis of Steiner and Taborek [30].

F and S were iteratively derived from empirical data and presented graphically in their original form. The fitted functions shown in Table 2.3 are from a later paper by Edelstein, Pérez and Chen that is commonly referred to as the 'modified' Chen correlation [31]. Other authors have also fitted functions to the original graphical functions, such as the forms derived by Butterworth as presented by Groeneveld *et al* [32].

Gungor and Winterton took the additive form of the Chen correlation and proposed new forms for the enhancement and suppression factors—the resulting correlation is shown in Table 2.3. They relabelled the convective boiling enhancement factor *E*. Their bank of experimental data included subcooled boiling data thereby extending the range of applicability. The Dittus-Boelter correlation is retained from the Chen correlation as the liquid-only convection heat transfer coefficient but the enhancement factor was re-derived as a sum of unity plus power law terms for the boiling number and the turbulent-turbulent Martinelli parameter. The choice of pool boiling correlation was updated to that of Cooper [33].

The Martinelli parameter can be roughly described as a measure of the degree of inter-phase friction. Gungor and Winterton used it to represent the effect of increased vapour velocity and thermal boundary layer thinning due to increased turbulence. Similarly they respresented thermal boundary layer perturbation using the boiling number, *Bo*, which relates the local vapour generation rate in proportion to the total mass flux. The suppression factor was derived to be strongly dependent on the inverse of *E* and less strongly on *Re*. The coefficients of the expressions for *E* and *S* were derived by iteratively fitting their forms to experimental data.

For saturated boiling Gungor and Winterton's correlation predicted water data with a standard deviation of 17.1% and on average underpredicted heat transfer coefficients by 5.2%. For subcooled boiling the standard deviation was 25% with an underprediction of 8%. For the same data set the original Chen correlation had standard deviations of 30.1% and 27% with mean errors of -25.8% and -2% respectively. Some results with R11 and R12 instead of water were included with the subcooled data [33].

The Shah correlation, shown in Table 2.5, is based on curve fits to an earlier graphical correlation by the same author. The ratio of the two-phase to single phase heat transfer coefficient is computed as a function of the the boiling number *Bo* or the convection number *Co*. In all the author gives a total of seven expressions to calculate the two-phase heat transfer enhancement multiplier. Which expression is used depends first on the value of *Co* then on the value of *Bo* and finally two values of the multiplier are computed and the greater of the two is chosen [34]. The single phase 'liquid-only' heat transfer coefficient is based on the Dittus-Boelter correlation using Re_L.

For the nucleate boiling multiplier, ψ_{nb}, the dependence on *Bo* is relatively weak, raised to the 0.5 power, which, as mentioned above, Klimenko was critical of in the Chen correlation as is Kandlikar whose correlation is discussed below [29, 26]. The correlation also contains a number of correction factors for horizontal flow which are not shown here. Because of its form this correlation's predictions will yield discontinuous results as parameters are varied.

Shah's original graphical correlation was evaluated agains 790 data points with a standard deviation of 14%. The author cites another evalution of heat transfer correlations where it was found to have a standard deviation of 23% compared to 47% for the Chen correlation. No explicit limit on the parameter range is given for pressure, diameter, or mass flux. The only other limits the author places on the correlation is its use after CHF has been reached. This is the reason for the vague range of application given in Table 2.5. Several of the correlations discussed below test this correlation using their data banks with varying results.

Author(s) *Year*	**Form of Correlation**	**Parametric Ranges**
Shah *1982*	$\frac{h_{tp}}{h_{LO}} = \left\{ \begin{array}{ll} \max\{\psi_{cb}, \psi_{nb}\} & Co > 1 \\ \max\{\psi_{cb}, \psi_{bs}\} & Co \leq 1 \end{array} \right.$ $\psi_{cb} = 1.8Co^{-0.8}$ $\psi_{nb} = \left\{ \begin{array}{ll} 230Bo^{0.5} & Bo > 0.3 \times 10^{-4} \\ 1 + 46Bo^{0.5} & Bo < 0.3 \times 10^{-4} \end{array} \right.$ $\psi_{bs} =$ $FBo^{0.5}\exp(2.74Co^{-0.1}) \quad 0.1 < Co \leq 1.0$ $FBo^{0.4}\exp(2.47Co^{-0.15}) \quad Co \leq 0.1$ $F = \left\{ \begin{array}{ll} 14.7 & Bo \geq 11 \times 10^{-}4 \\ 15.43 & Bo < 11 \times 10^{-4} \end{array} \right.$ $Co = \left(\frac{1-x}{x}\right)^{0.8} \left(\frac{\rho_V}{\rho_L}\right)^{0.5}$	$0 \leq x \leq 1$ $\ddot{q} < \ddot{q}_{CHF}$
Klimenko *1986*	$h_{tp} = \left\{ \begin{array}{ll} h_{bo} & N_{cb} < 1.6 \times 10^4 \\ h_c & N_{cb} > 1.6 \times 10^4 \end{array} \right.$ $N_{cb} = Bo_* \left(\frac{\rho_V}{\rho_L}\right)^{\frac{1}{3}}$ $h_{bo} = 7.4 \times 10^{-3} \times$ $Pe_*^{0.6} K_p^{0.5} {Pr_L}^{-\frac{1}{3}} \left(\frac{k_w}{k_s}\right)^{0.15}$ $Pe_* = RePrBo \left(\frac{\sqrt{\frac{\sigma}{g(\rho_L - \rho_V)}}}{D\left(\frac{\rho_V}{\rho_L}\right)} \right)$ $K_p = \frac{P}{\sqrt{\sigma g(\rho_L - \rho_V)}}$ $h_c = 0.087{Re_m}^{0.6}{Pr_L}^{\frac{1}{6}} \left(\frac{\rho_V}{\rho_L}\right)^{0.2} \left(\frac{k_w}{k_s}\right)^{0.09}$ $Re_m = \sqrt{\frac{\sigma}{g(\rho_L - \rho_V)}} \left(\frac{G}{\rho_L}\right) \left[1 + x\left(\frac{\rho_L}{\rho_V} - 1\right)\right]$ $Bo_* = \frac{Gh_{LV}}{\ddot{q}} \left[1 + x\left(\frac{\rho_L}{\rho_V} - 1\right)\right]$ $h_{tp+LO} = (h_{tp}^3 + h_{LO}^3)^{\frac{1}{3}}$	$0.06 < P < 3.04$MPa $50 < G < 2690\frac{kg}{m^2s}$ $0.017 < x < 1.0$ $1.63 < D < 41.3$mm
Kandlikar *1990*	$\frac{h_{tp}}{h_{LO}} =$ $1.1360Co^{-0.9} + 667.2Bo^{0.7} \quad Co < 0.65$ $0.6683Co^{-0.2} + 1058.0Bo^{0.7} \quad Co > 0.65$	$0.1 \leq P \leq 6.42$MPa $67 \leq G \leq 8179\frac{kg}{m^2s}$ $0.001 \leq x \leq 0.699$ $67 \leq \ddot{q} \leq 2280$ $5 \leq D \leq 32$mm

Table 2.5: Two-Phase Heat Transfer Correlations—'Conditional' Forms

Klimenko's correlation for saturated flow boiling is, like the Shah correlation, a conditional correlation whereby a criteria is given to select between correlations for convective boiling or nucleate boiling. It is shown in Table 2.5. The condition is based on a dimensionless quantity he defines as the 'convective boiling number', N_{CB}. The effect of wall thermal conductivity is taken into account. Its effect is stronger for nucleate boiling than convective boiling which is logical since the bubble growth and departure process could result in, on a very small scale, temperature gradients at the wall. It is noted that the thermal conductivity effect is stronger for cryogenic fluids than for results conducted at 'room temperature' but no discussion is made of its effect at relatively high temperatures. Near the threshold value of N_{CB}, rather than using the transition criteria explicitly, the higher of the two values computed using both correlations should be used. [29].

Klimenko's choice of nucleate boiling correlation is interesting because it is based solely on experimental results from cryogenic fluids. Furthermore the influence of *Re* and *Pr* are significantly less than for other boiling correlations with $h \propto Re^{0.6}Pr^{\frac{1}{6}}$. For water he recommends the nucleate boiling correlation of Rassokhin *et al* based on the recommendations of Guglielmini *et al* [24]. It is presumed that in the analysis of his correlation's accuracy he uses the expressions shown in his paper rather than the one he recommends for water. When single phase convection is significant Klimenko recommends superimposing his two-phase value with the single phase value using the power law shown in Table 2.5. This effect will only be significant when the two-phase heat transfer coefficient is small.

For water 99.4% of data points fall within ±35% of Klimenko's prediction with standard deviation of 11.8%. For comparison, the same quantities, using Klimenko's database of water points, were 71% and 23.9% for the Chen correlation and 70.4% and 27.4% for the Shah correlation respectively.

Kandlikar's 1990 correlation, shown in Table 2.5 is in the form of a ratio of the two-phase to liquid-only heat transfer coefficient. Like Klimenko's correlation he uses a condition based on a threshold value of a dimensionless number to determine the form of the correlation for nucleate boiling dominated heat transfer or convective boiling dominated heat transfer. He takes the form of a correlation he developed in an earlier paper using power-law terms for the convection number, *Co*, and *Bo*. The constant and exponent coefficients for each term, and in each regime, were fitting using a database of over 5000 points for water and various refrigerants. On either 'side' of the threshold value of *Co* the form of the correlation remains the same but the coefficients change. Near the threshold value of *Co* the higher value generated using both correlations should be chosen similar to Klimenko's recommendation [26]. The correlation is shown Table 2.5.

Kandlikar notes that his correlation correctly predicts the trend of increasing h with increasing x in the nucleate boiling region for water and vice-versa for refrigerants in agreement with the respective experimental data. This is achieved by using a fluid-specific empirically-determined dimensionless constant on the nucleate boiling term. Like the Shah correlation Kandlikar does not explicitly use a nucleate boiling correlation but relies entirely on empiricism to determine nucleate boiling heat transfer enhancement using the *Bo* term. He does note that, regardless of the regime the *Bo* term's exponent is 0.7 in keeping with the heat flux dependence of most pool boiling correlations.

For his water data 66% are predicted within ±20% and 86% within ±30% with a standard deviation of 15.9% for all water data. In comparison the mean deviations for the Chen (1966), Shah (1982), and Gungor and Winterton (1986) correlations using Kandlikar's water data were 29.6%, 17.9% and 20.7% respectively. Data for horizontal tubes was predicted with higher accuracy than for vertical tubes. However for Froude numbers, *Fr*, less than 0.04 an extra power multiplier for the *Co* term is added. The presence of the extra correlating term may contribute to improved accuracy for horizontal tubes. This condition is not shown in Table 2.5 because it is not relevant for vertical tubes.

Steiner and Taborek's correlation is shown in Table 2.4. The authors use a power law to combine two terms each of which is similar to the terms in the Chen-based correlations. The power law, however, ensures that the predicted value of h_{tp} is dominated by the larger of the two terms with a smooth transition between convective boiling and nucleate boiling when the contributions of each term are relatively equal. All coefficients were fitted using a database of over 13 000 data points [30].

The authors of this correlation derived it with the intent of having proper asymptotic limits over a very wide range of parameters. The authors state the correlation was evaluated and developed for saturated boiling only. Because of its proper asymptotic behaviour and its conditionality on a minimum $\ddot{q}_{ONB}$ it is not unreasonable to extrapolate it to the subcooled boiling region. In the absence of bulk vapour quality and nucleate boiling the correlation reduces to the single-phase turbulent heat transfer coefficient.

For convective boiling the authors allow the user to choose any single-phase convection correlation to calculate the 'liquid-only' heat transfer coefficient. The 'liquid-only' mass flux is the total—vapour and liquid—mass flux assumed to flow as a liquid. The convective boiling enhancement factor is similar to most other correlations. It contains two power-law terms that account for liquid hold-up and vapour acceleration. The nucleate boiling term is highly empirical. Instead of an explicit correlation for nucleate boiling the local heat flux is divided by a fluid-dependent 'base' coefficient and raised to an exponent that varies as an exponential function of pressure from 0.7 at a reduced pressure, $p_r = \frac{P}{P_{crit}}$, of 0 to 0.27 near critical pressures. There are also explicit empirical functions to adjust the boiling heat transfer coefficient for the effects of pressure, diameter, surface roughness, and the fluid's molecular mass. Nucleate boiling heat transfer is assumed to be 0 if the heat flux is less than the minimum heat flux at the onset of nucleate boiling $\ddot{q}_{ONB}$.

Steiner and Taborek do not present a statistical evaluation of the performance of their correlation based on their whole database. Rather they selected several single data sources against which to compare their correlation. For ethanol, 92% of data were predicted within ±20% and 98% within ±30%; for the same tolerances the results are 71% and 82% respectively for R12. The Chen correlation predicted 73% and 85% of ethanol values within the 20 and 30% tolerances but performed very poorly for R12. The Shah, Gungor and Winterton and Kandlikar correlations were also evaluated with very poor results. Although not evaluated explicitly in their paper, Steiner and Taborek's correlation should predict water values very well since their database contained 10 000 water points out of 13 000 in total.

Chapter 3

Experimental Details

A new experimental facility was designed and constructed in order to obtain heat transfer data under transient conditions. Steady-state heat transfer data gathered during commissioning tests is presented in the next Chapter. Its specifications are laid out in this chapter. A schematic diagram of the experiment is shown in Figure 3.1.

A magnetically coupled pump provides the driving head for the loop. A bypass loop and control valve are used for coarse flow control and to damp any hydrodynamic oscillations that may occur. The preheater raises the water to the desired inlet temperature before entering the 'Test Section.' The fluid is heated in the test section and the enters the condenser. The condenser condenses any vapour and cools the fluid to less than 80°C to prevent damage to the pump. Hydrostatic pressure is controlled by a bladder-type accumulator charged with nitrogen from a high-pressure gas cylinder.

The fluid temperature is measured at the inlet and outlet of both the pump and the test section. Absolute pressure measurements are made at the test section outlet

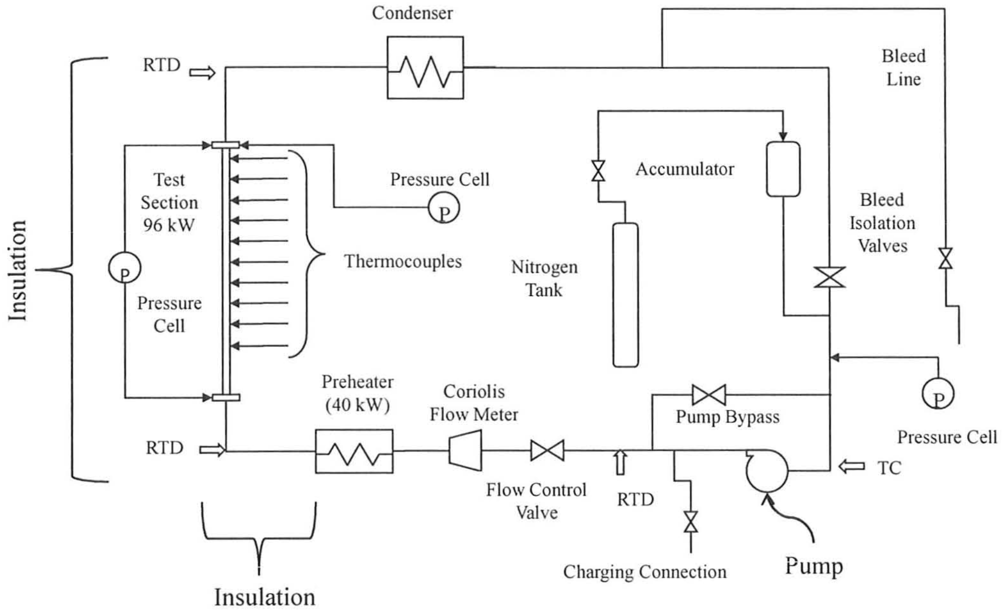

Figure 3.1: Schematic diagram of loop components

and near the pump inlet where the accumulator is coupled to the experiment. The pressure drop is measured between the test section inlet and outlet using a differential pressure sensor. Test section voltage is measured at the test section while the power supply provides a current measurement. Test section power is computed as $Q = IV$. Wall temperature measurements are made at several locations along the test section. The test section is insulated between the inlet and outlet fluid temperature measurements to prevent heat losses that would result in heat balance errors.

3.1 Hydrodynamic Components

3.1.1 Fittings and Tubing

The experiment was constructed using Swagelok stainless steel 316 seamless tubing in 6.4 mm OD, 12.7 mm OD, and 9.5 mm OD sizes. Swagelok stainless steel 316 front-and-back ferrule type fittings were used throughout the loop with a few exceptions. 316 stainless steel was chosen for its corrosion resistance. Swagelok tube fittings were chosen for their leak resistance, reliability, and ease of use. Table 3.1 gives a complete inventory of the tubing used in the experiment, its description, and where it was used. Table 3.3 gives the same information for fittings and Table 3.2 shows the Conax Technologies fittings used for electrical isolation. Their electrical properties are given in Section 3.2. Tables 3.1 and 3.3 refer to Swagelok part numbers except where otherwise noted.

The pressurized loop volume, not including the accumulator, is approximately 1900 cm^3. This includes 14.0 m of 12.7 mm OD, 9.5 m of 6.4 mm OD, and 9.3 m of 9.5 mm OD tubing and flexible hose. Most of the 9.5 mm OD tubing is represented in the preheater and condenser. The gross pressurized loop volume is 5685 cm^3 including the 3785 cm^3 accumulator.

3.1.2 Pump

The exact specifications of the pump are not available because it was salvaged from an earlier experiment that is no longer in use. By inspection of the pump's components and configuration it is likely a Micropump GC-series externally driven suction shoe pump. The specifications of the Micropump GC-series pump with the M25

Part No.	*Amount*	*Description and Use*
SS-T8-S-035-20	13.4 m	•12.7 mm OD by 0.9 mm tubing •Main loop material
SS-T6-S-035-20	9.3 m	•9.5 mm OD by 0.9 mm tubing •Preheater and inner condener tubes
SS-T4-S-035-20	9.0 m	•6.4 mm OD by 0.9 mm tubing •Pressure transducer and accumulator lead and bleed lines •Pressure control system
89865K33 *McMaster-Carr*	6 ft	•6.4 mm OD by 0.9 mm Inconel 600 tubing •Test section material

Table 3.1: Comprehensive table of tubing used in the experiment

Part No.	*No.*	*Description*
EG-375-A-XX-L	2	•9.5 mm electrical feedthrough for preheater
EG-250-A-XX-L	2	•6.4 mm electrical feedthrough for test section

Table 3.2: Conax Technologies fittings for electrical isolation

gear set is given in Table 3.4 [35]. The flow-head curve given by the manufacturer can be linearly interpolated from the flow rate data in the table.

The pump is sealed and coupled magnetically to a 120 VAC powered 0.373 kW DC motor made by Pacific Scientific. The motor has a maximum operating Voltage of 90 VDC and maximum current of 5.3 A.

3.1.3 Pressure Control

Hydrostatic pressure is applied to the experiment by a 3.79 L bladder-type accumulator made by Grier. It consists of an oval-shaped pressure vessel with a 31.8 mm FNPT main connection and a 6.4 mm FNPT bleed connection at the bottom of the vessel. It has a maximum working pressure of 13.79 MPa. Pressure is applied by an internal bladder that is filled via a .305-32" Schrader-type inflating connection at the top of the pressure vessel. A diagram is shown of the pressure control system

Part No.	***No.***	***Description and Use***
SS-810-9	3	•12.7 mm 90° elbow •Uninstrumented 90° corners
SS-810-3	4	•12.7 mm tee •Pump bypass (2) •Condenser outlet bleed line •Accumulator connection to loop
SS-810-3-8-4	3	•12.7 mm tee, 6.4 mm branch •Pressure transducer lead line connections to main loop
SS-400-3	1	•6.4 mm tee •Outlet pressure and differential pressure lead line coupling
SS-400-1-4	9	•6.4 mm tube fitting to 6.4 mm MNPT adapter •Pressure transducer lead and bleed line adapters •Accumulator bleed outlet fitting
SS-810-3TFT SS-6-RB-2 SS-100-1-2	4	•12.7 mm inlet by 12.7 mm branch by 9.5 mm FNPT tee •9.5 mm MNPT to 3.2 mm FNPT straight adapter •3.2 mm MNPT to 1.6 mm tube fitting straight adapter •Seals fluid temperature measurement probes
SS-810-6-6	4	•12.7 mm to 9.5 mm straight tube fitting •Condenser inlet and outlet
SS-810-1-6	2	•9.5 mm MNPT to 12.7 mm tube fitting adapter •Pump connections
SS-810-7-8	2	• 12.7 mm FNPT to 12.7 mm tube fitting •Test section electrical isolation connector
SS-810-7-12	2	• 19.1 mm FNPT to 12.7 mm tube fitting •Preheater electrical isolation connector
SS-20-RB-12 SS-400-1-12	1	•31.8 mm MNPT to 19.1 mm FNPT reducer •19.1 mm MNPT to 6.4 mm tube adapter •Primary connection to accumulator
SS-4-TA-1-4	1	•6.4 mm MNPT to 6.4 mm tube stub •Accumulator bleed line connection.

Table 3.3: Comprehensive table of fittings used in the experiment

Specification	***Performance***
Maximum operating pressure	•10.3 MPa
Maximum differential pressure	•0.87 MPa
Flow Rate at 1 mPa-s	•0.103 $^{L}/_{s}$ at 0.0 MPa(d) •0.078 $^{L}/_{s}$ at 0.87 MPa(d)
Displacement	•1.82 mL per revolution
Operating Speed	•3450 rpm

Table 3.4: Micropump GC-M25 pump specifications

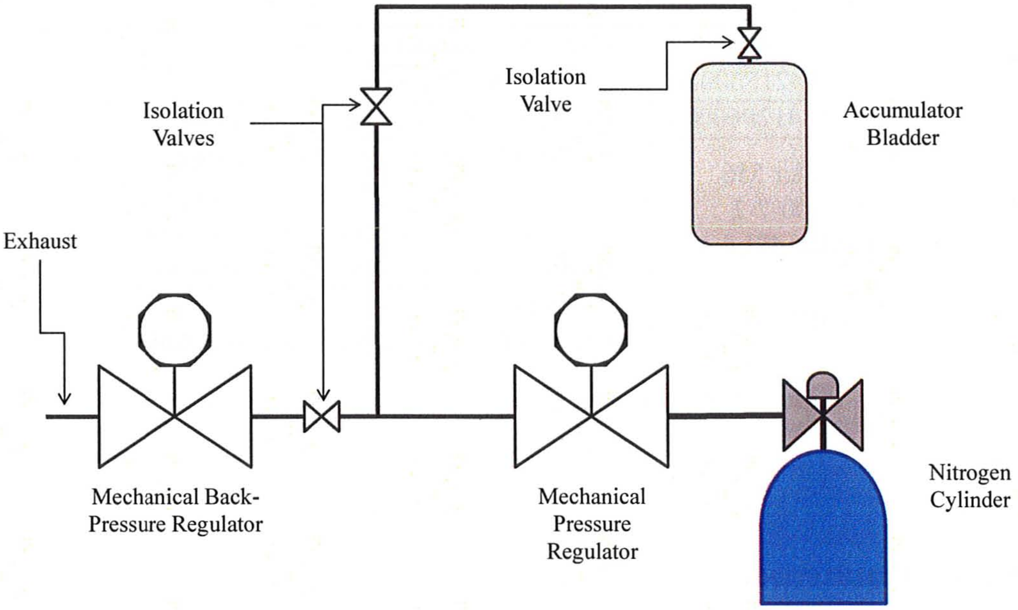

Figure 3.2: Schematic diagram of pressure control system

is shown in Figure 3.2.

The bladder is filled with nitrogen from a high-pressure gas cylinder. Pressure is controlled using a pressure regulator to maintain pressure and a back-pressure regulator to exhaust gas in case of over-pressure. Model numbers for all components in the pressure control system, including the pressure and back-pressure regulators, can be found in Table 3.5.

Using the accumulator and regulators pressure control better than ±20 kPa was achieved. The system is capable of control accuracy up to ±5 kPa if the operator pays close attention to the system pressure display on the data acquisition system output as the system parameters change—e.g. test section power is increased which may cause flow rate and outlet pressure changes.

Component	*Description*
SS-400-3	•6.4 mm tee
SS-400-9	•6.4 mm elbow
CGA-580	•Nitrogen cylinder connector
KPP1NSF421P60020	•0-13.79 MPa pressure regulator
KPB1N0A412P60000	•0-13.79 MPa back pressure regulator
Schrader 556 SS-400-7-2 SS-FM4SL4SL4-18	•3.2 mm MNPT to .305-32 inflating connector •3.2 mm FNPT to 6.4 mm tube fitting •45.7 cm length of 6.4 mm flexible hose •Primary gas connection to accumulator
SS-4P4T-BL	•6.4 mm valve •Accumulator and gas cylinder isolation

Table 3.5: Components used in pressure control system

3.1.4 Condenser

To condense and cool the water after it leaves the test section a counterflow tube and shell heat exchanger was used. Cooling water was supplied to the outer annulus—the shell—using cold tap water. The 'municipal' supply typically provides water at ≈15°C with up to ≈410 kPa of driving pressure.

The heat exchanger was made from 9.5 mm OD by 0.9 mm wall tubing for the inner tube with a 22.2 mm OD copper 'shell'. These tubes were rolled into six 20.3 cm diameter coils. This configuration was able to cool saturated two-phase water at 2.0 MPa—212°C—to less than 50°C at combined test section and preheater powers of nearly 30 kW.

3.2 High-Powered Components

3.2.1 Test Section and Power Supply

The test section was composed of a 1.19 m long piece of 6.4 mm OD by 0.9 mm wall thickness Inconel 600 tubing—as shown in Table 3.1—with a heated length of 93.2 cm and an unheated development length of 28.7 cm—more than 60 diameters—at the inlet. Inconel 600 was chosen for the low variance of its electricaly conductivity over a wide temperature range [36]. This ensures that the axial heat flux distribution is uniform.

A schematic diagram of the test section is shown in Figure 3.3. Thermocouples were used to measure wall temperature at each of the locations shown—their detailed specifications are outlined in a following section. Power was applied to the test section using large copper bus bars. Three 373.7 MCM—very low resistance—electrical cables were used to transmit power from the power supply to each of the bus bars to minimize heat generation and voltage losses.

Power was supplied to the test section by a Magnavolt Technologies, Inc., model number TCP32.100.400.SHMI, DC power supply. It was composed of one master and two slave 32 kW Regatron TC.P.32 units capable of providing 32 kW of DC power each for a total of up to 96 kW.

The unit was tested and calibrated by test engineer Bruno Ammann at Magnavolt's facility in Plattsburg, NY on November 18, 2008 in conformity with ISO 9001 quality control standards and 'CE' electrical regulations. Calibration results are shown in Table 3.6.

Electrical isolation of the test section was provided by Conax Technologies EG-

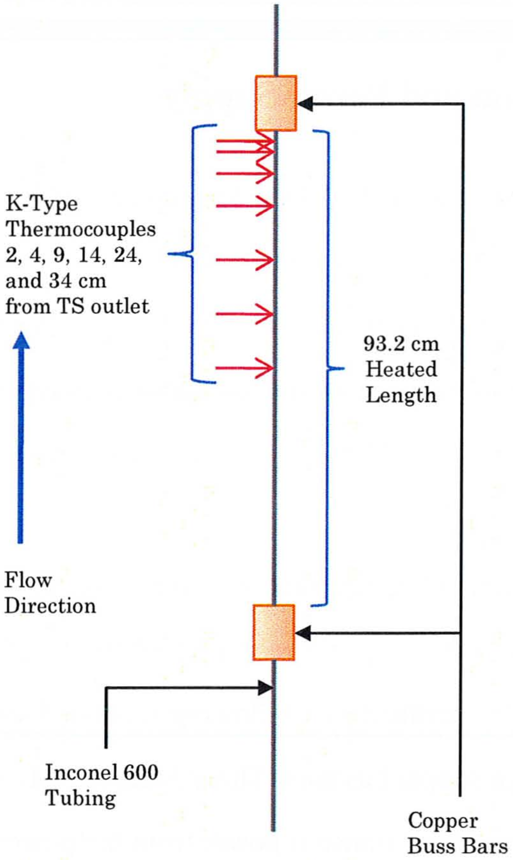

Figure 3.3: Schematic diagram of the test section

250-A-XX-L electrode sealing glands. A diagram of the sealing gland assembly is shown in Figure 3.4.

3.2.2 Preheater and Power Supply

A preheater was used to maintain a constant test section inlet temperature. The preheater was a resistance-heated coiled length of 9.5 mm OD by 0.9 mm wall SS 316 tubing. Power was supplied by a Miller SR-B7-1000 power supply capable of

Specification	***Value***
Maximum Power	96 kW
Maximum Current	1200 A (0-80 V)
Maximum Voltage	100 V (0-960 A)
Current De-Rating (80 V)	$T_{ambient} \leq 30°C$ 1080 A $T_{ambient} \leq 35°C$ 960 A $T_{ambient} \leq 40°C$ 900 A
Static Accuracy (Line Regulation)	$< \pm 0.1\%$
Stability at Constant Conditions (8 hours, following 0.5 hour warmup)	$< \pm 0.05\%$
Ambient Temperature Coefficient	Voltage $< \pm 0.02\%/°C$ Current $< \pm 0.03\%/°C$
Output Ripple	300 Hz $< \pm 1.1\%$FS V_{p-p} 300 Hz $< \pm 0.4\%$FS V_{RMS}
Output Noise	40-1000 kHz $< 1.5V_{p-p}$ 40-1000 kHz $< 0.1V_{RMS}$

Table 3.6: Test section calibration data

providing 40 kW RMS of continuous AC power with a maximum current of 1000 A at 50 V. Electrical isolation was achieved using a Conax Technologies EG-375-A-XX-L electrode sealing gland similar to the one shown in Figure 3.4.

The preheater length was optimized to maximize the output of the power supply according to a V-I curve provided by the power supply manufacturer and also limit the wall temperature to less than 350°C at a variety of inlet temperatures and flow rates based on the estimated range of experimental conditions. Wall temperature was estimated using the Dittus-Boelter correlation. The power optimization assumed a constant value of 90Ω·cm for the electrical conductivity of SS 316. It was assumed that, in order to minimize size, the preheater would be coiled to a diameter of 0.20, 0.25, or 0.30 m and that only integer numbers of coils would be used. The resulting design used 4.47 m of tubing in seven 0.19 m diameter coils with an estimated total resistance of 0.167 Ω and maximum power of 28.5 kW.

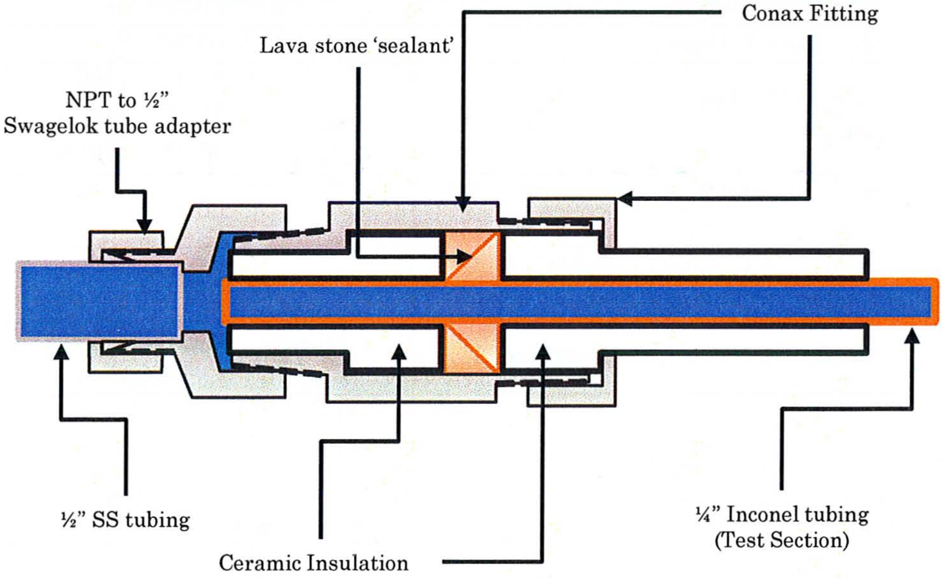

Figure 3.4: Electrical insulation schematic

The maximum observed power output was limited to approximately 12 kW at 90% full power. This may be due to the failure of the design calculations to take lead cable and contact resistances into consideration. The power supply itself is also well used and may no longer meet its maximum design specifications.

3.3 Measurements and Instrumentation

3.3.1 Data Transmission and Acquisition

All experimental measurements excluding wall temperature were recorded using a Keithley 3700 data acquisition system. Measurements were made using Keithley

3721 digital multimeter modules. The Keithley modules were capable of measuring voltage, current and resistance as well as temperature using a K-type thermocouple and an internal reference junction. Relevant measurement accuracies are shown in Table 3.7.

Range	*Measurement Accuracies*
0.1–10 V:	Resolution: 1 μV Accuracy: ±0.0025% + 20 μV Temperature Coefficient*(/°c): ±0.0001%+ 1μV
1–10 mA:	Resolution: 0.1 nA Accuracy: ±0.05% + 0.9μA Temperature Coefficient*(/°c): ±0.005%+0.5μA
10–100 mA:	Resolution: 1 nA Accuracy: ±0.05% + 9μA Temperature Coefficient*(/°c): ±0.005%+5μA
100–1000 Ω:	Resolution: 100 $\mu\Omega$ Accuracy: ±0.0065% + 0.004 Ω Temperature Coefficient*(/°c): ±0.0008%+0.001Ω
-150–1372°C:	Resolution: 0.001 °C Accuracy: ±1°C Temperature Coefficient*(/°c): ±0.03°C
*Operating Temperature	23±5°C Coefficient Applies: 0–18°C/28–50°C

Table 3.7: Keithley multimeter module specifications

3.3.2 Load Resistance and Test Section Power

Some current measurements were converted to voltages using load resistors. The voltage across the load resistor was then measured by the Keithley 3721 unit. This was done because only two current measurement 'slots' for each of the two Keithley 3721 boards used were available.

The resistance values of the load resistors was measured using a Fluke 77 Series III handheld multimeter. This is more accurate than using the resistor colour code

Resistor	*Value*
Flow Meter	267±1.5Ω
Wall Temperature	266±1.5Ω
Differential Pressure	267±1.5Ω
Test Section Inlet Temperature	267±1.5Ω
Test Section Outlet Temperature	267±1.5Ω

Table 3.8: Load resistor values

values since poor ±5% specification resistors were used. For resistive loads of 100–320 Ω it has an accuracy of ±0.5% + 0.2Ω. The resistance values for all load resistors used this way are given in Table 3.8.

The same handheld multimeter was used to measure the voltage applied to the test section at the buss bars. For DC Voltages of 1–100 V it has an accuracy of ±0.3% + 0.01 V. Test section current readings were taken from the front panel display of the power supply. Test section power was calculated as $Q = V_{meas} \times I_{meas}$.

3.3.3 Fluid Temperature

Fluid temperature measurements were made by Resistive Temperature Devices—RTDs—at the test section inlet and outlet, and at the preheater inlet. A K-type thermocouple was used to measure the fluid temperature at the pump inlet. Their specifications are given in Table 3.9.

The test section inlet and outlet temperature measurements were measured using Omega TX-69 4–20 mA transmitters configured with a temperature range of 20–220°C. Their current outputs were measured as load resistor voltages by the Keithley 3721. The TX-69 transmitters have a real-time digital temperature display. This allowed the experiment operator to more effectively control test section

Type and Model	*Position*	*Specifications*
RTD PR-17-2-100-1/16-6-E	TS Inlet TS Outlet	•3-wire RTD • $-200 < T < 850$°C •Accuracy: ±0.15°C+0.2% •Measured by Omega TX-69
RTD PR-17-2-100-1/16-6-E	Preheater Inlet	•3-wire RTD • $-200 < T < 850$°C •Accuracy: ±0.15°C+0.2% •Measured by Keithley 3721
Thermocouple HKMQIN-062-U	Pump Inlet	•K-type Thermocouple •Range: $0 < T < 1250$°C •Accuracy: Greater of ±1.1°C or 0.4% •Measured by Keithley 3721

Table 3.9: Fluid temperature measurement devices

inlet temperature and observe when the fluid reached saturation at the outlet. The TX-69 specifications are shown in Table 3.10. The RTD and lead line resistances at the flow meter inlet were measured directly by the Keithley 3721 digital multimeter. The K-type thermocouple at the pump inlet was measured and converted to a temperature value by the Keithley 3721 using its internal reference junction.

Measurement	*Uncertainties*
RTD	Digital Accuracy: ±0.1°C Drift: ± 0.1% span/year Temperature Stability: ±0.004%/°c Calibration Accuracy: ±0.05% DAC Accuracy: ±0.02%
Thermocouple (K-type)	Digital Accuracy: ±0.1°C Drift: ± 0.1% span/year Temperature Stability: ±0.004%/°c Calibration Accuracy: ±0.05% DAC Accuracy: ±0.02% Cold Junction Accuracy: ± 0.5°C

Table 3.10: TX-69 4-20 mA transmitter specifications

3.3.4 Wall Temperature

Wall temperature measurements were made using Omega HKMQIN-010-U K-type thermocouples. Their specifications are identical to those of the HKMQIN-062-U thermocouple as shown in Table 3.9. The probe diameter is 0.010 in (0.0254 mm) instead of 0.062 in. Very fine-gauge thermocouples were chosen for their low thermal resistance and physical flexibility. The thermocouples were cemented to the outer wall of the test section using high temperature chemical-set cement with a thermal conductivity of 7.4×10^{-4}W m^{-1} $^{o}C^{-1}$ [37]. A very thin layer—on the order of 0.1 mm thick—of the same cement was applied for electrical isolation before affixing the thermocouples.

Temperature measurements were made by nine thermocouples at seven locations along the test section as shown in Figure 3.3. At the locations 2 and 4 cm from the outlet two thermocouples were fixed at radially opposite locations for more robust CHF detection.

Due to difficulties with the Keithley unit, wall temperatures were measured using one TX-69 transmitter for one of the thermocouples 2 cm from the TS outlet. Other thermocouple measurements were made by visually reading an Omega HH-502 handheld temperature calibration device. For K-type thermocouples above 0°C it has an accuracy of ±0.3% + 0.3°C.

Wall Temperature Correction

The outside wall temperature was was used to infer the test section inner wall surface temperature so that the heat transfer coefficient could be evaluated at the inside wall of the test section. This method is outlined in [38]. Novog, Yin, and Chang provided an expression for the thermal conductivity of Inconel 600 as a function of temperature that was accurate to within ± 0.1% for temperatures from 50 to 500^{o}C. They then solved the steady-state conduction equation in radial co-ordinates using insulated outside boundary conditions and a transformation of variables. All future indications of 'inside wall temperature' or 'inside wall temperature measurement' refer to the value calculated using this method.

$$\bar{K}=\frac{K_T}{K_{T,ref}} \qquad \bar{q}=\frac{\dddot{q}R^2}{K_{T,ref}T_{ref}} \qquad K_r=K_0\exp\left(\omega T\right) \qquad \bar{r}=\frac{r}{R} \qquad \bar{T}=\frac{T}{T_{ref}}$$

$$\bar{T}=1+\frac{1}{\omega T_R}\ln\left(1-\frac{\omega T_R\bar{q}}{4}\left(\bar{r}^2-2\ln\left(\bar{r}\right)-1\right)\right) \tag{3.1}$$

The solution is shown above in Equation 3.1 where all temperatures are in Kelvin, K is thermal conductivity in $\frac{W}{mK}$, and $\dddot{q}$ is the volumetric heat generation rate in $\frac{W}{m^3}$. The fit parameters for the thermal conductivity of Inconel 600, ω and K_0, have the values $1.64\times10^{-3}K^{-1}$ and 11.83 $\frac{W}{mK}$ respectively. Experimental uncertainties for inside wall temperature measurement were propagated using the error propagation equation as shown in Equation 3.2 [39].

3.3.5 Pressure

Absolute pressure was measured at the test section outlet by a Rosemount 3051C-A4A-22A1A-C6TR 0–13.790 MPa absolute pressure transmitter calibrated to a linear output of 4-20 mA. At the pump inlet pressure was measured by a Rosemount 3051CG5 pressure transmitter calibrated to 0–13.000 MPa absolute by Stern

Laboratories in March 2009. Differential pressure was measured by a Rosemount 1151DP5 pressure transmitter calibrated to 0–180 kPa absolute; it was also calibrated in March 2009 by Stern laboratories. Their specifications are given in Table 3.11. The calibration data from Stern laboratories is presented Appendix A.

The absolute pressure transmitter outputs were measured as current outputs on the Keithley 3721 multimeter. The differential pressure unit gave unstable readings in this configuration. The differential pressure transmitter's current output was measured indirectly as a voltage across a 270 Ω resistor by the Keithley unit.

Model	***Range***	***Specifications***
3051CG5	0–13.000 MPa(a)	2σ:±0.1414% RMS error:±2.535 kPa
1151DP5	0–180 kPa(d)	2σ:±0.1680% RMS error:±0.0539 kPa
3051CA4	0–13.790 MPa(a)	Reference Accuracy (3 σ):±(0.065 %FS) Five-year Stability (3 σ):±0.125 %URL

Table 3.11: Pressure transmitter specifications

3.3.6 Flow Rate

Flow rate was measured by a Krohne Optimass 7000 S15 Compact coriolis flow meter. Its specifications are given in Table 3.12.

Specification	*Value*
Maximum Flow Rate	3125 $^{g}/_{s}$
Reference Accuracy	±0.1% + Zero Stability
Repeatability	±0.05% + Zero Stability (includes linearity and hysteresis)
Zero Stability	±0.015%(Maximum Flow Rate)

Table 3.12: Krohne Optimass 7000 S15 Compact mass flow meter specifications

3.3.7 Total Measurement Errors

Standard deviations for measured values are calculated by computing the square root of the sum of the variances, (σ_i^2), of each component of uncertainty. Sources of error for each type of measurement are compiled in Table 3.13.

Measurement uncertainties were propagated using the error propagation equation when the data was reduced [39]. The equation is shown in Equation 3.2 for a hypothetical function of N variables, $c = f(a_1, ..., a_N)$.

$$\sigma_c^2 \approx \sum_{i=1}^{N} \sigma_i^2 \left(\frac{\partial f}{\partial a_i}\right)^2 \tag{3.2}$$

This form of the error propagation equation is approximate because it does not include covariance terms. This approximation is adequate since, overall, the covariance terms including the partial derivatives are relatively small. For example: the uncertainty in a heat transfer coefficient calculated using Equation 1.1 includes the uncertainty in wall temperature, fluid temperature, and test section power. Both wall and fluid temperature have covariances with respect to test section power. The uncertainty in test section power, and the influence of test section power uncertainty on the overall uncertainty, are very small with respect to the uncertainty in temperature measuremen by at least an order of magnitude. As a result the contribution of the covariance terms of the error propagation equation to the overall uncertainty in heat transfer coefficient is negligible.

In addition to instrumentation uncertainties, experimental results may be biased due to the violation of some assumptions that were used when the data was reduced. The most significant sources of experimental bias in this thesis were the assumptions that the test section was perfectly insulated and that heat was conducted in the radial direction only when Equation 3.1 was used to calculate the inside wall temperature of the test section.

This assumption induced a systematic error into the results because heat losses resulted in the actual inside wall temperature being greater than that calculated based on the assumption that the outer wall was insulated. For example, if the measured outside wall temperature was 220^oC at a test section power of 8 kW the calculated inside wall temperature was 210.6^oC which changed to 211.5°C with a 10% heat loss. This was on the order of magnitude of the uncertainty in the outside wall temperature measurement to one standard deviation; the effect increased at higher powers. Heat losses through the outside wall also resulted in the effective 'wall thickness' being thinned over which there is a net heat flux towards the fluid. A 10% reduction in wall thickness resulted in the same change of calculated inside wall temperature as a 10% reduction in heat flux. Since these effects occur in tandem they compounded one another.

Measurement	*Uncertainty*
Flow Rate	•Keithley 3700 •Fluke 77 Series III •Krohne Optimass 7000 S15 •±0.8 g/s at 33 g/s
Wall Temperature (1)	•Keithley 3700 •Fluke 77 Series III •Omega TX-69 •K-Type thermocouple •±3.5°C at 220°C
Wall Temperature (2)	•Omega HH-502 •K-Type thermocouple •±3°C at 220°C
Fluid Temperature	•Keithley 3700 •Fluke 77 Series III •Omega TX-69 •RTD •±3°C at 212°C
TS Outlet Pressure	•Keithley 3700 •Rosemount 3051CA •±12 kPa at 2000 kPa
Differential Pressure	•Keithley 3700 •Fluke 77 Series III •Stern Laboratories Calibration •Rosemount 1151 (drift) •±1.2 kPa(d) at 100 kPa(d)
Pump Inlet Pressure	•Keithley 3700 •Stern Laboratories Calibration •Rosemount 3051CG (drift) •±6 kPa at 2000 kPa

Table 3.13: Sources and typical values of uncertainty with 95% confidence and one year drift for each measurement

Chapter 4

Experimental Results

4.1 Introduction

The experiments were performed at a pressure of 2.0 MPa while inlet temperature and mass flux were varied. Mass fluxes of 1500 and 2000 kg $m^{-2}s^{-1}$ were used while inlet temperature was varied to 126, 148, 170, and 180°C. These inlet temperatures correspond to subcooled thermodynamic mass qualities of -0.200, -0.150, -0.100, and -0.077.

The effect of heated length on boiling heat transfer can be examined by comparing the heat transfer results at different test section positions. As indicated in Chapter 3 there is an unheated development length at the test section inlet of more than 60 *D*. No heat transfer measurements are made less than 100 diameters from the beginning of the heated length. For these experiments, *Re* varied from approximately 36 000—69 000 at the test section inlet based on the inlet mass flux, inlet temperature, and test section exit pressure. Turbulent flow in pipes typically becomes fully developed after 10–60 diameters [2]. Based on this analysis entrance effects were not considered in the following analysis.

4.1.1 A Note on the Figures

Experimental boiling curves are presented in four ways in this chapter and Appendix B. The legends in the figures indicate information for each of the curves displayed in each plot. For thermocouple linearity, the total test section power is displayed. For heated length effect the thermocouple positions are indicated. For constant inlet temperature the day and month the experiment was performed and the mass flux—in exponential notation—are shown. Similarly the lengend for constant mass flux shows the day and month of the experiment and the corresponding inlet temperature.

4.2 Thermocouple Linearity

Temperature measurements were made at seven positions along the test section using nine thermocouples. Good thermal contact at each thermocouple location is needed for reliable wall temperature measurements. If the heat flux is uniform and the heat transfer coefficient is nominally constant then the relative 'goodness' of thermal coupling to the outer test section wall can be checked by plotting the inside wall temperature against position along the test section. At 2000 kPa, linearly interpolating the enthalpy at 165°C between the enthalpy at 120 and 210°C differs from the actual value by less than 0.5%. Therefore for the pressure and range of temperatures of this experiment it can be assumed that the enthalpy varies linearly with temperature along the test section. The fluid enthalpy rise in the test section varies

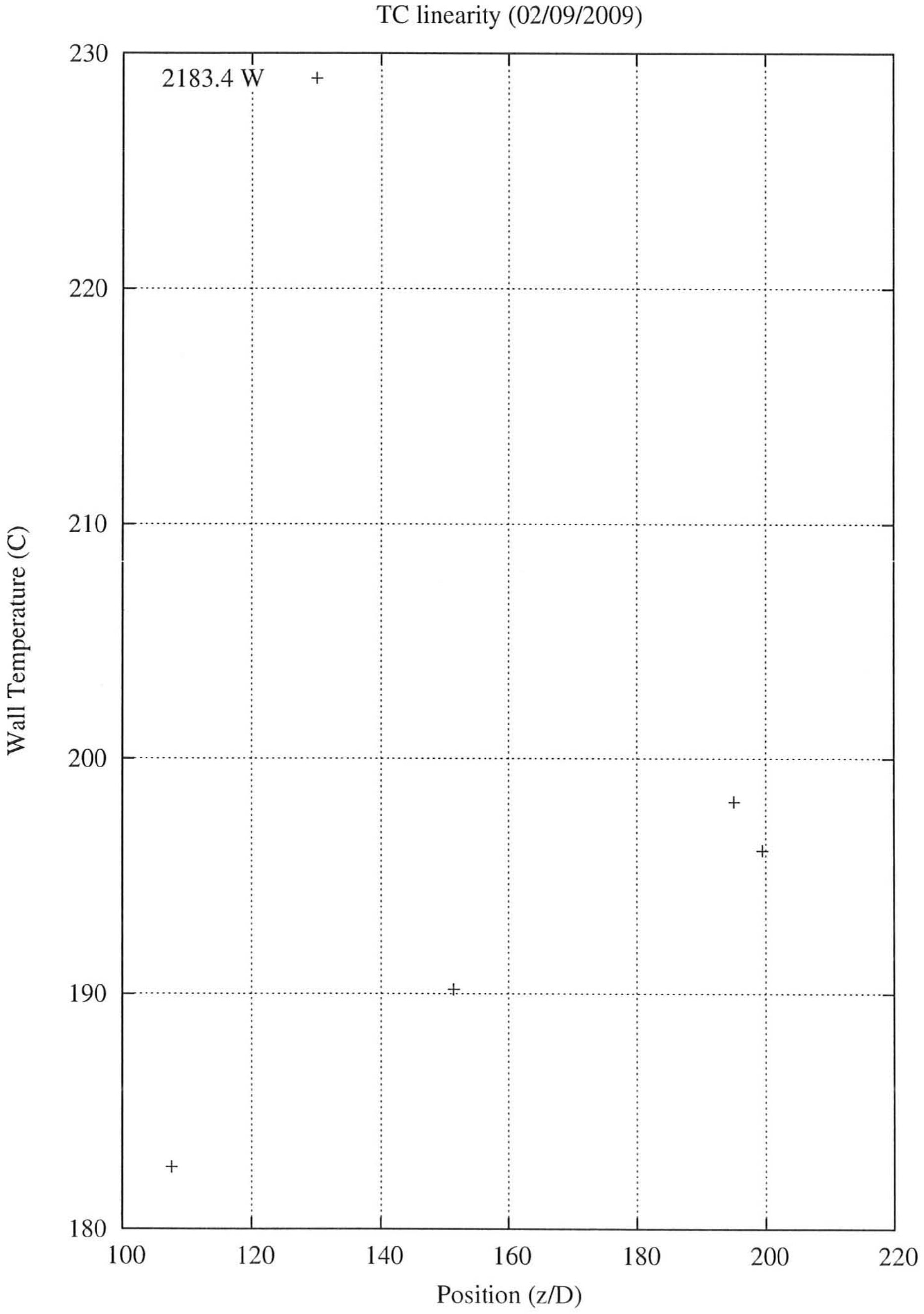

Figure 4.1: Thermocouple linearity for thermocouples 2, 4, 24, and 44 cm from the test section outlet

with the local heat flux. Therefore if the heat flux is constant the axial fluid temperature variation will be very nearly linear. If the thermocouple attachments are equally good then the measured wall temperature should also demonstrate linearity with axial distance.

Out of nine thermocouples, four of them exhibited consistently good linearity. Figure 4.1 demonstrates the good linearity of the thermocouples located 4, 24, and 44 cm from the test section outlet. The measurements made by these thermocouples are analyzed in detail in the next chapter. The thermocouples located 9 , 14, and 34 cm from the test section exit generally exhibited lower than expected temperature readings. The low readings can be attributed to poor thermal contact with the test section since this would 'insulate' the thermocouples from the wall.

It is evident that the thermocouples located 2 cm from the test section exit also exhibit poor linearity. Near the test section outlet some of the low measured temperature values may also be attributed to axial conduction due to the large thermal capacitance of the bus bars. As indicated in Chapter 3 the bus bars used to electrically couple the power supply to the test section were large copper blocks. Spade connectors were crimped to all three of the power supply cables to join them with the bus bars. The crimped connections to the spade connectors were roughly 2 cm in diameter by 10 cm long of bare metal. Axial heat conduction to the bus bars occurred near the test section outlet due to heat losses through the large surface area of the spade connectors and the large thermal capacitance of the bus bars. This resulted in a reduced heat flux to the coolant and a smaller radial temperature gradient in the test section wall. This phenomenon accounts for the majority of the non-linearity exhibited by this thermocouple. A relatively small portion of the non-linearity may be due to poor thermal coupling with the test section wall. The measurements 2 cm from the test section outlet are important because this location observed the most saturated boiling heat transfer. It is evident that the behaviour of the thermocouples at this location was relatively good as can be seen by comparing Figure 4.1 with Figures B.1 and B.2. Since no method was devised to explicitly correct for the effect of axial conduction, however, the data from this thermocouple location was also excluded from the analysis in the next chapter.

Plots that demonstrate poor thermocouple linearity for positions 9, 14, and 34 cm from the test section outlet can be found in Appendix B.

4.3 Heat Balance

A plot of heat losses against heat flux is shown in Figure 4.2. The figure shows that the measured power to fluid is higher than the measured electrical power to the test section at high powers. The source of this problem was likely due to either a bias in the inlet temperature measurement, the calibration of the mass flow meter, or the zero of the mass flow meter. Further investigation will eliminate these sources of error from future experiments.

These measurement errors induced a bias in the estimation of local fluid temperature and local mass quality. It is evident from the discussion in Chapter 5 that this has a significant effect on the prediction of single phase heat transfer. Subcooled boiling and low mass quality saturated boiling are not strongly dependent on mass flux or local subcooling. This is because the wall to fluid temperature difference is much larger for boiling heat transfer than for single phase heat transfer, and the wall temperature is more strongly influenced by the wall superheat rather than the

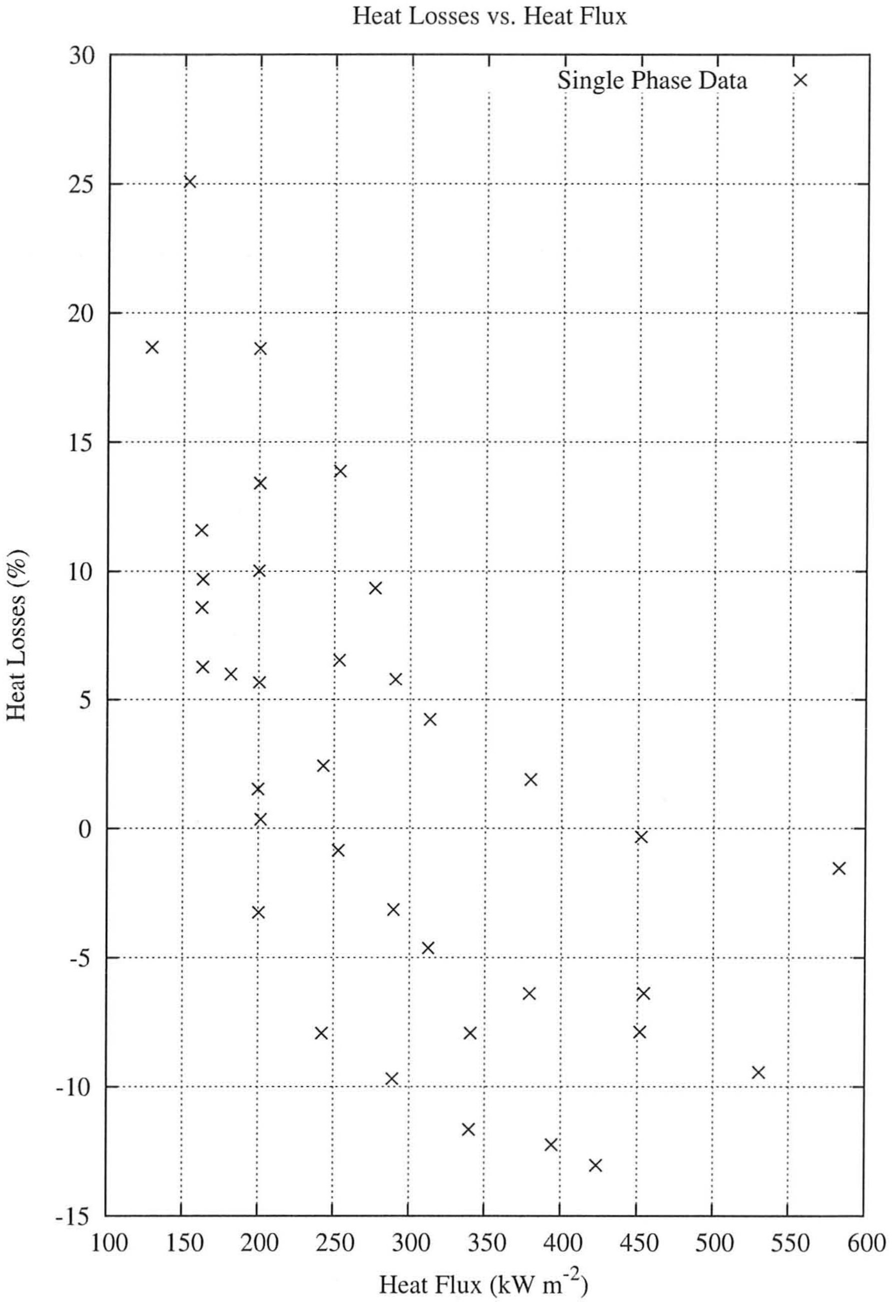

Figure 4.2: Heat losses plotted against heat flux for data points that had no boiling at any point in the test section

bulk temperature difference. Therefore nucleate boiling heat transfer data were not as strongly influenced by biases and uncertainties in bulk temperature and flow rate as were single phase heat transfer data.

4.4 Pressure Drop

Figure 4.3 shows the measured pressure drop across the test section for several experiments with two mass fluxes and two inlet temperatures. These measurements include the pressure drop through 15 cm sections of 10.9 mm ID tubing upstream and downstream of the Conax fittings used to electrically isolate the test section.

For single phase flow, pressure drop increases with mass flux and decreases with fluid temperature. Pressure drop increases significantly as boiling begins and occurs further upstream in the test section as the power is increased.

4.5 Heat Transfer Coefficients

Figure 4.4 shows calculated heat transfer coefficients for several experiments with two mass fluxes and two inlet temperatures. These plots indicate the range of heat transfer coefficients measured during single phase convection, subcooled boiling, and saturated boiling.

It is evident from the figure that single phase heat transfer increases with mass flux for constant heat flux. This figure also indicates that heat transfer coefficients measured at very low heat fluxes may be artificially high. This is likely due to heat losses from the test section being on the same order of magnitude as the power to the test section. The boiling regions of these curves would collapse onto one

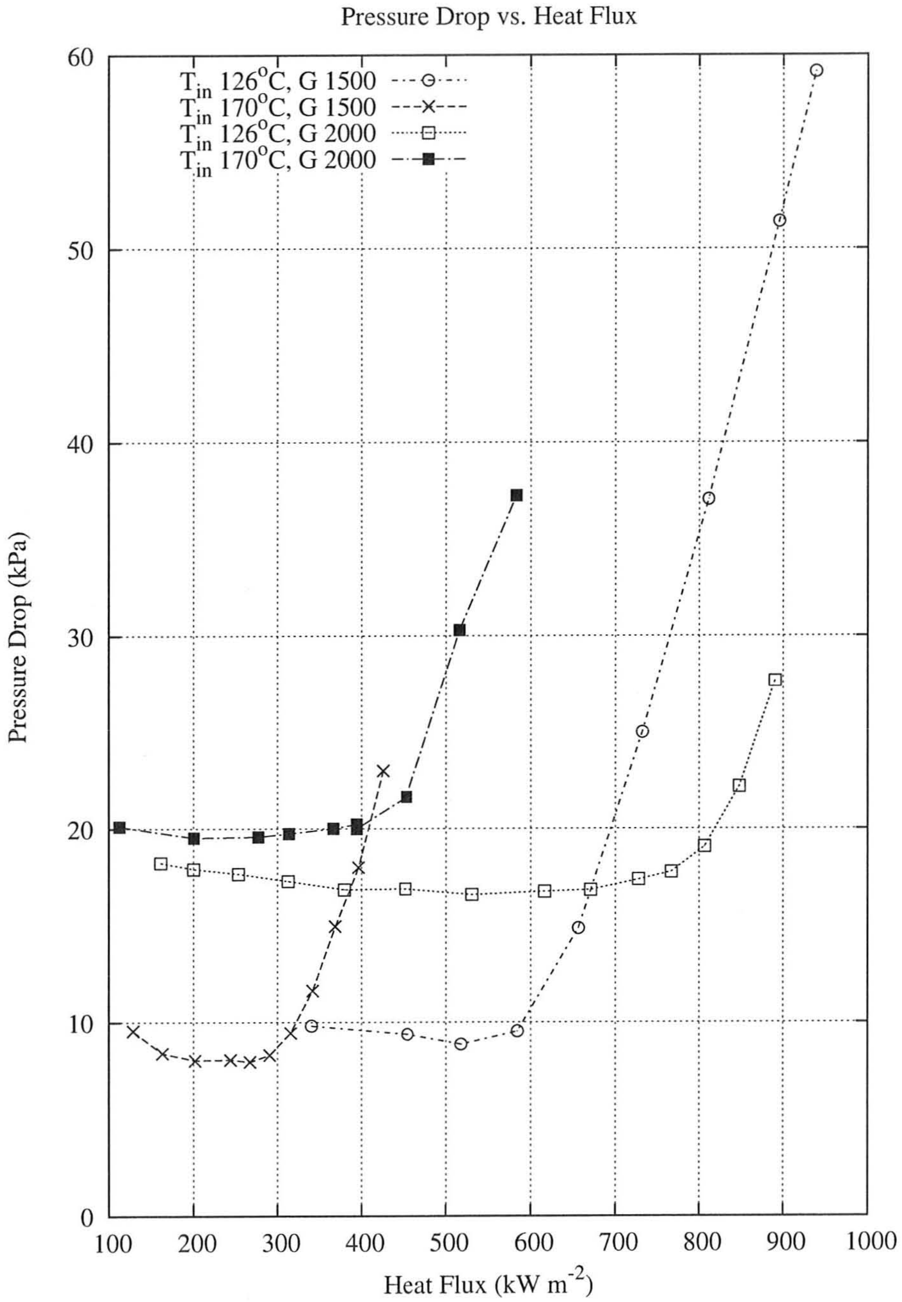

Figure 4.3: Heat flux vs. pressure drop for four experiments with two inlet temperatures and two mass fluxes

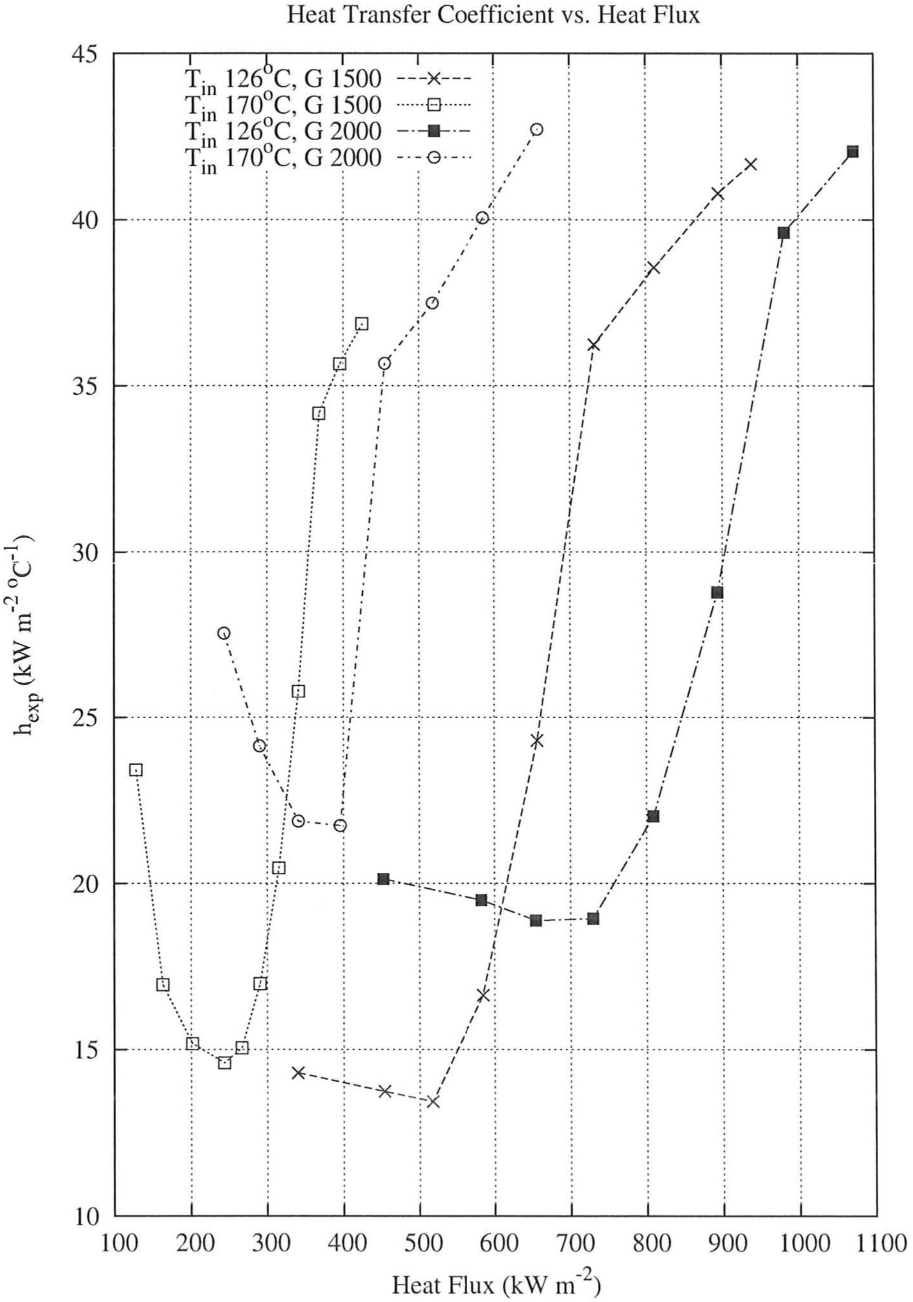

Figure 4.4: Heat transfer coefficient vs. heat flux for two inlet temperatures and two mass fluxes, measured 4 cm from the test section exit

another if the heat transfer coefficient were redefined in terms of wall superheat instead of the overall difference between the wall and the bulk fluid temperature. This is because the wall temperature in nucleate boiling is largely independent of local subcooling—see Table 2.2.

4.6 Effect of Heated Length

The test section length was not varied but heat transfer measurements were taken at several positions along the heated length. Figure 4.5 shows heat flux plotted against the temperature difference between the wall and the bulk fluid for single phase flow. The slope of the curve for each heated length was nearly identical. This indicates that the heat transfer coefficients did not vary significantly with heated length for single phase flow.

Figure 4.6 shows boiling curves, with error bars of one standard deviation to illustrate typical values of uncertainty for heat flux and wall temperature, for four test section positions with constant mass flux and inlet temperature. As indicated in the preceding section the 2 cm thermocouple demonstrated relatively poor linearity. Figure 4.6 shows that for all values of heat flux the 2 cm thermocouple measurement gave a lower temperature reading than the 4 cm thermocouple largely due to heat losses through the bus bars. The 2 cm data is included here for completeness so that this boiling curve need not be reproduced in the Appendix.

The 44, 24, and 4 cm curves appear to asymptoptically approach each other at high values of wall superheat. Therefore the wall temperature was ‘constant’ at different positions along the heated length that reached fully developed boiling. This supports the subcooled boiling correlations that are independent of bulk fluid

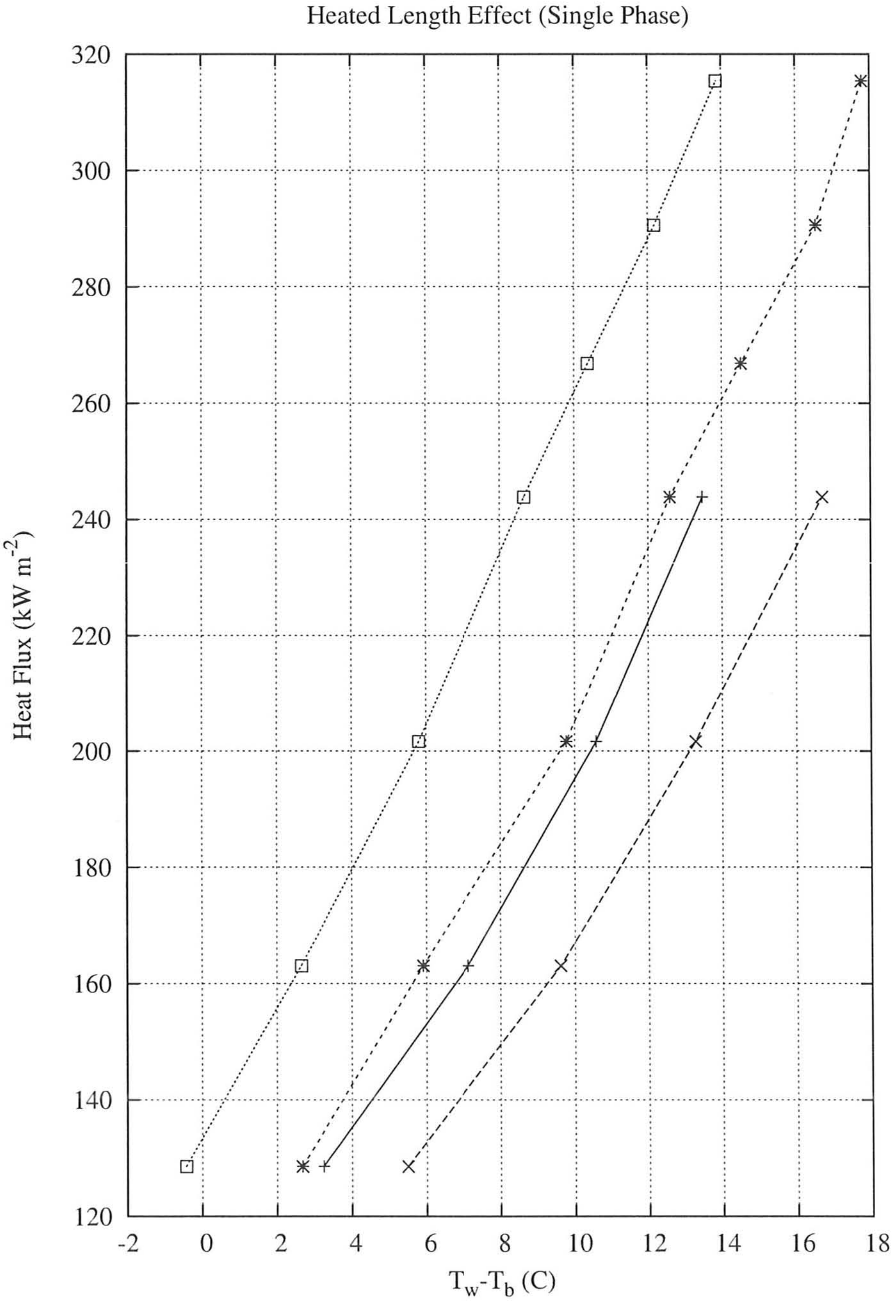

Figure 4.5: Single phase heat transfer for four test section positions with T_{in}=170.0^{o}C and mass flux of 1500 kg m^{-2} s^{-1}

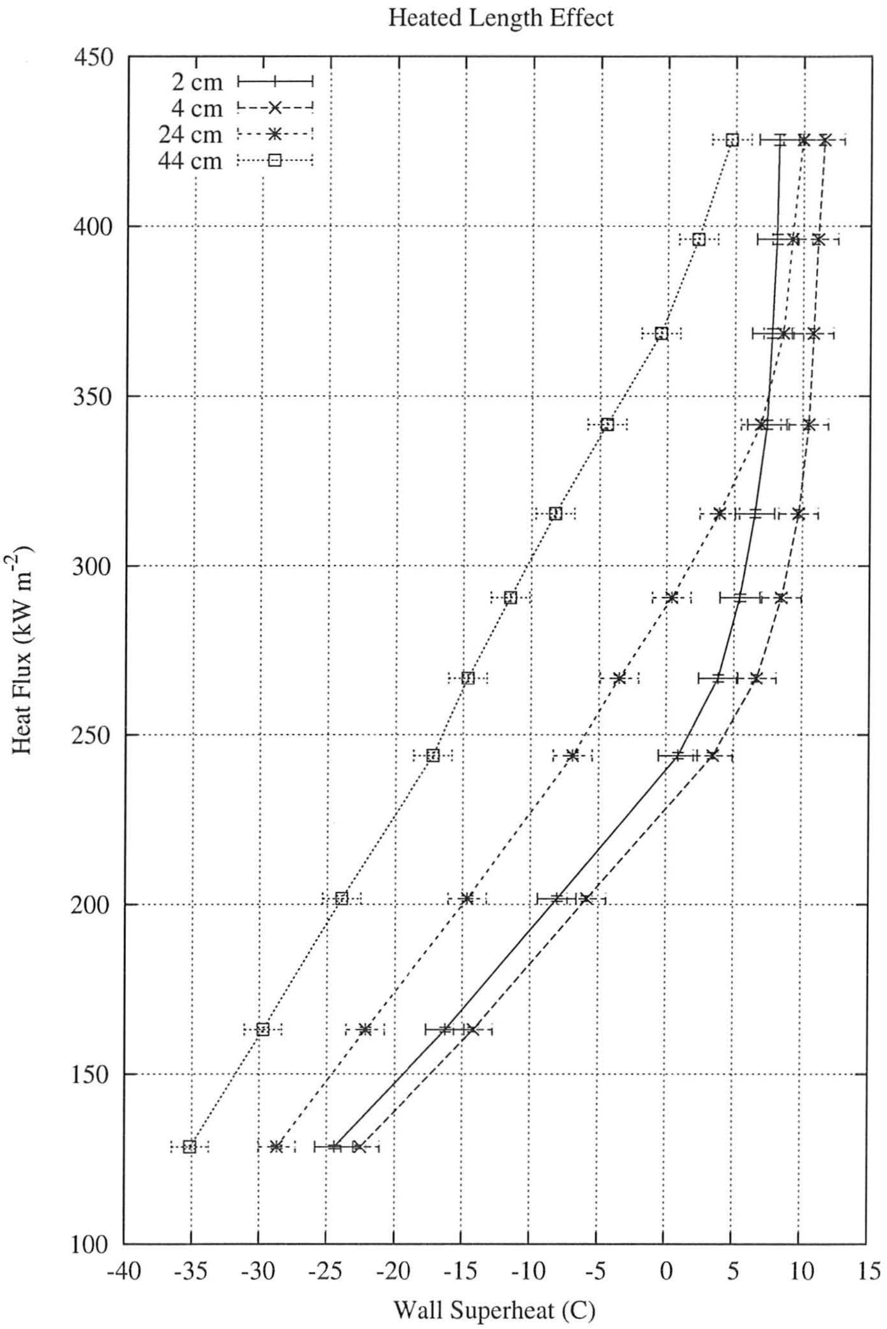

Figure 4.6: Boiling curves for four test section positions with T_{in}=170.0^{o}C and mass flux of 1500 kg m^{-2} s^{-1}

temperature since subcooling is higher for shorter heated lengths with constant heat flux, mass flux, and inlet temperature.

More boiling curves that demonstrate the effect of heated length can be found in Appendix B.

4.7 Effect of Mass Flux

Figure 4.7 displays typical results for the effect of mass flux on heat transfer. There is a clear separation between the results for single phase heat transfer at different mass fluxes. Wall temperature at constant heat flux decreases with increasing mass flux.

The onset of nucleate boiling occurs when the slope of the boiling curve begins to increase. At lower mass fluxes the onset of boiling occurs at slightly lower heat fluxes. Wall temperature during fully developed boiling was observed to be slightly higher for higher mass fluxes. Figure 4.7 shows fully developed boiling above approximately 600 kW m^{-2} for a mass flux of 1500 kg m^{-2} s^{-1} and above 850 kW m^{-2} for 2000 kg m^{-2} s^{-1}.

The slope of the boiling curve for the lower of the two mass fluxes decreases above 800 kW m^{-2}; this likely coincides with OSV and/or saturated boiling. This makes it difficult to directly observe the effect of mass flux on subcooled boiling since lower mass flux flows reach saturation at lower heat fluxes. This problem is even more evident for higher inlet temperature boundary conditions as can be seen in Figure 4.8. The low mass flux curve can be seen to deviate from the steep-sloped nucleate boiling region before the heat flux is high enough to directly compare the fully developed boiling regions of each curve.

The uncertainty in the inside wall temperature measurements is larger than the difference between the fully developed boiling wall temperatures for the high and low mass flux boiling curves in Figure 4.7. It is possible that the apparent reduction in heat transfer with increased mass flux is simply a random error. This is unlikely because these boiling curves are consistent with results for a variety of other bound-

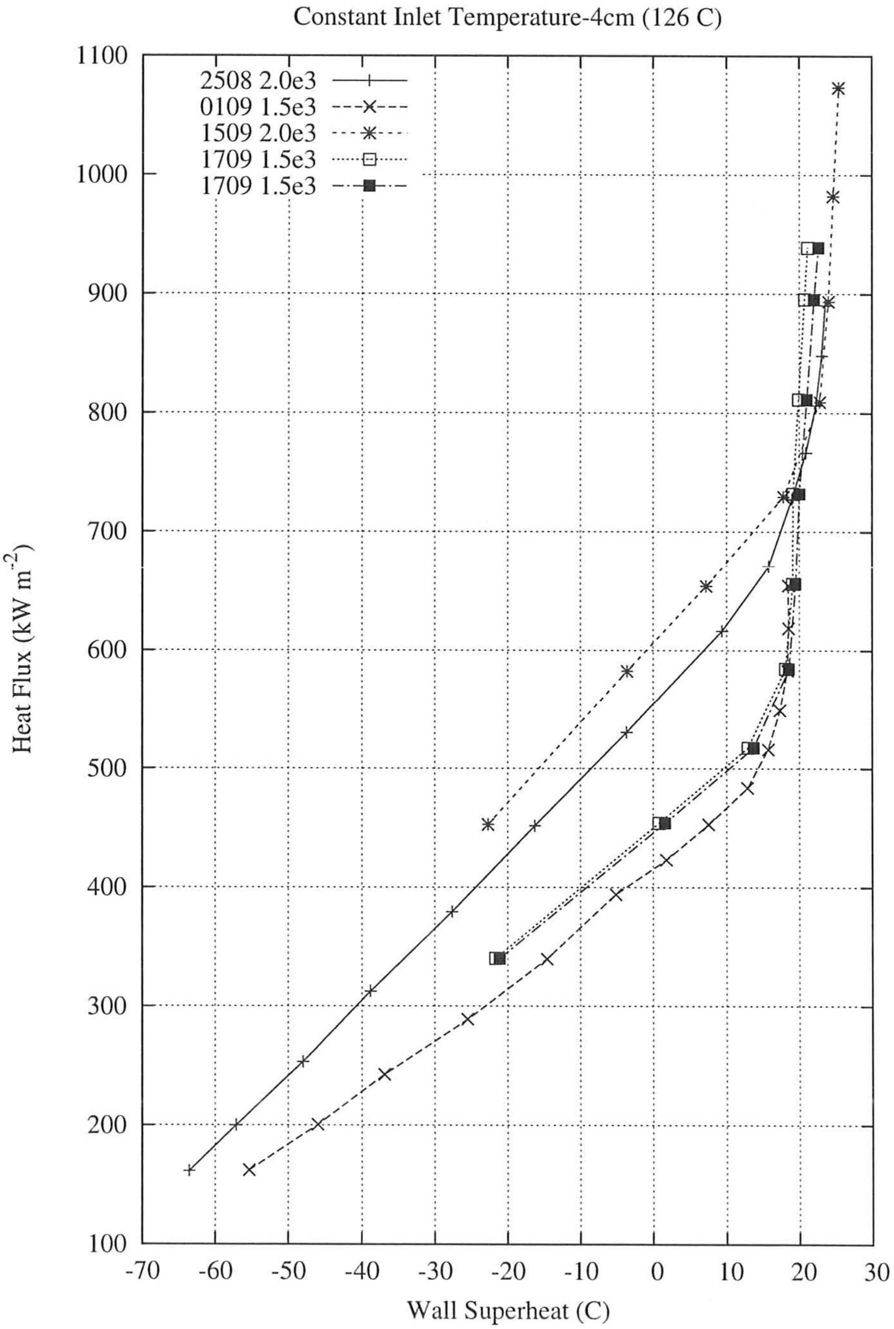

Figure 4.7: Boiling curves for constant inlet temperature of 126.0°C, 4 cm from the TS outlet

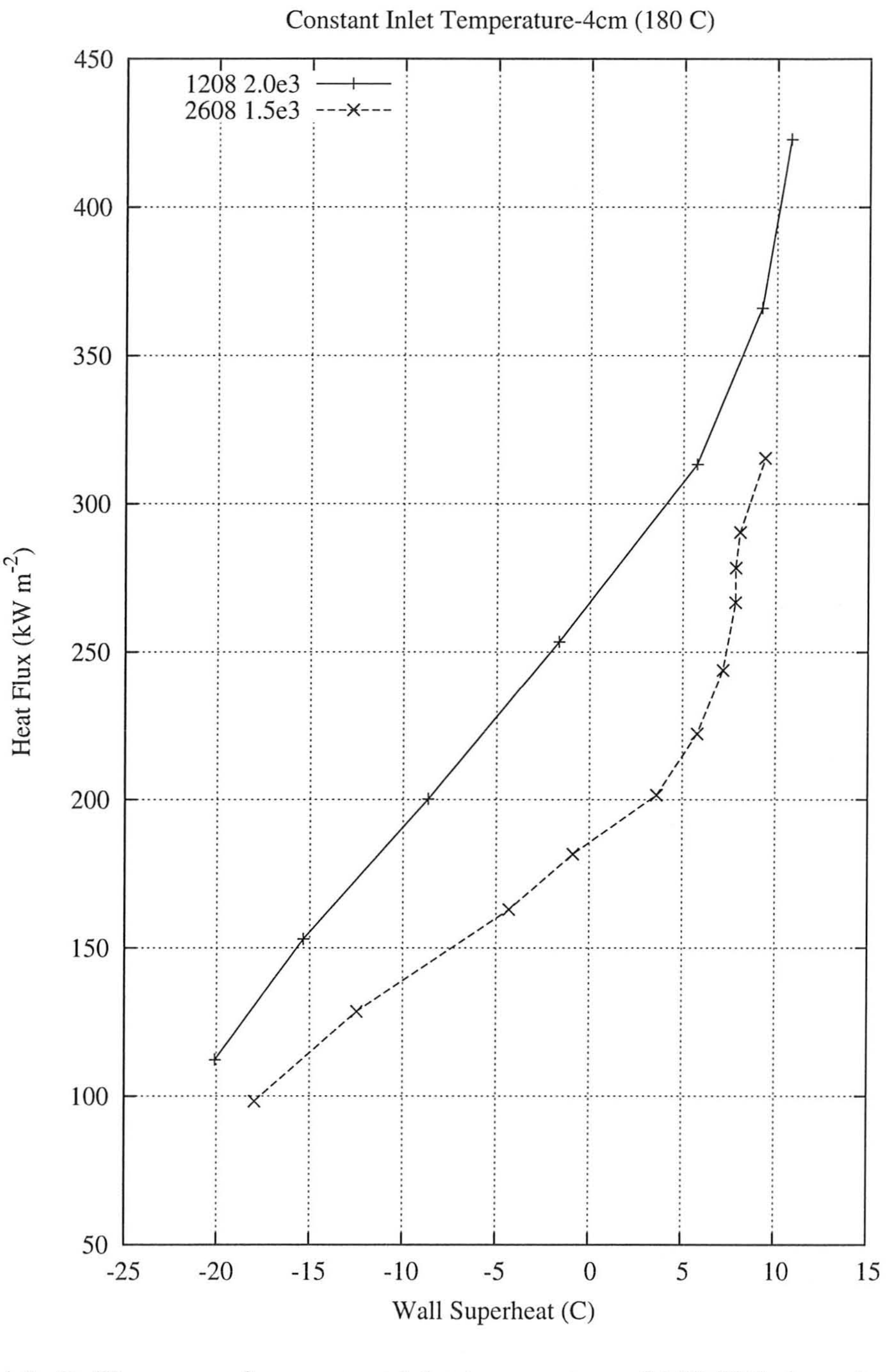

Figure 4.8: Boiling curve for constant inlet temperature of 180.0°C, 4 cm from the TS outlet

ary conditions. More boiling curves that support this observation may be found in Appendix B.

4.8 Effect of Inlet Temperature

The effect of inlet temperature can be seen in Figure 4.9 that displays boiling curves for constant mass flux. In the region of single phase heat transfer the curves are well-separated.

As inlet temperature increases the onset of nucleate boiling occurs at lower heat fluxes. It is evident that there is a systematic trend of decreasing wall temperature with increasing inlet temperature as fully developed boiling is approached. The boiling curves can be seen to 'cross' one another. This may be due to 'boiling suppression' because of higher radial temperature gradients in the fluid for lower inlet temperatures. It may also be attributable to the limits of experimental repeatability but this is unlikely since the trend is systematic for four different inlet temperatures.

In Figure 4.9 the slope of the boiling curves for T_{in} equal to 180.0^{o}C and 126.0^{o}C can be seen to first increase and then decrease in slope. As in Figure 4.7 this decrease in slope likely corresponds to OSV and/or saturated boiling.

More data for constant mass flux that demonstrates the effect of inlet temperature on the boiling curve can be found in Appendix B.

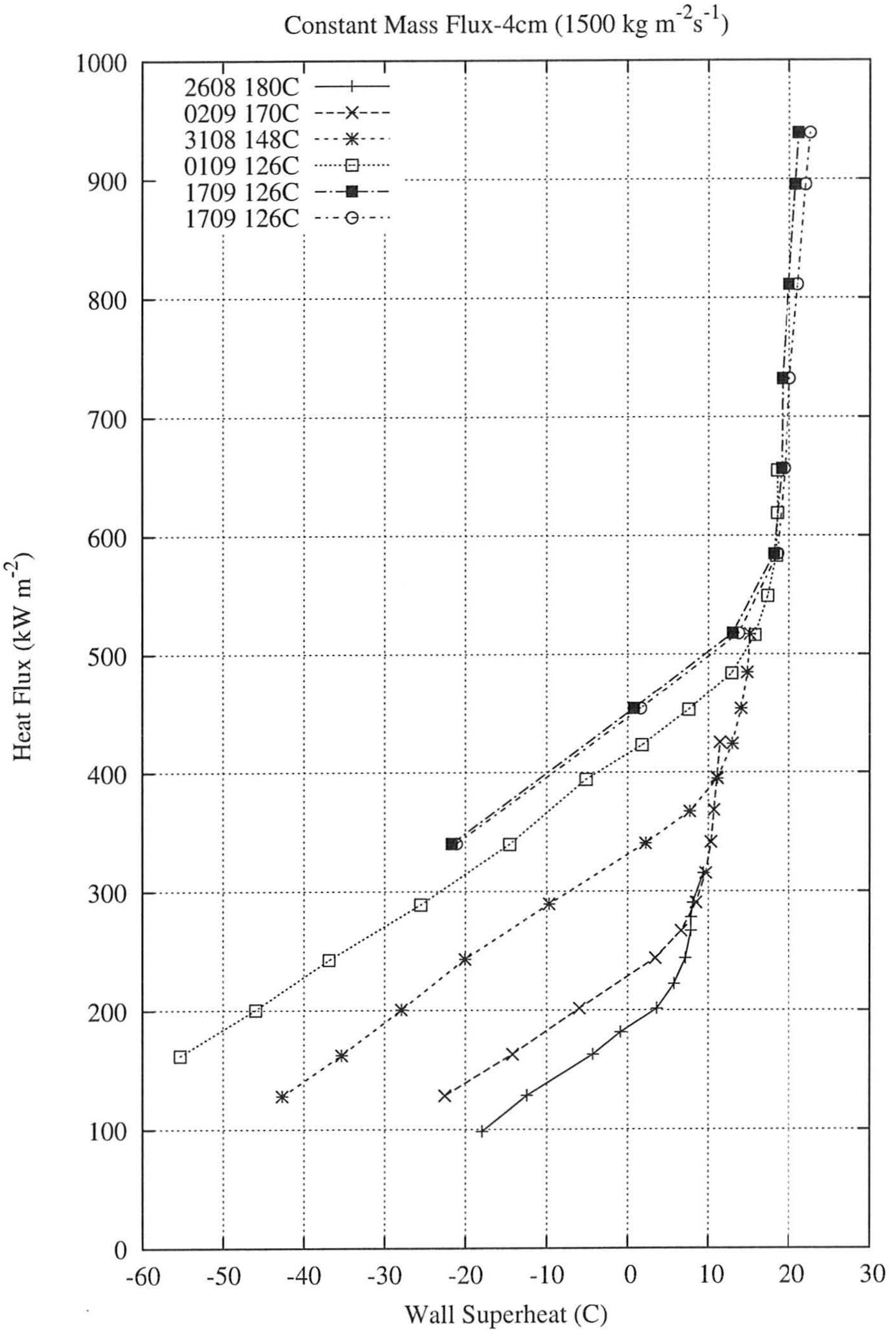

Figure 4.9: Boiling curves for constant mass flux of 1500 kg m^{-2} s^{-1}, 4 cm from the TS outlet

Chapter 5

Analysis and Discussion

5.1 Data Analysis Methodology

A MATLAB script was used to convert measured values into proper units, transform outside wall temperatures to inside wall temperatures, determine local Nusselt numbers, and calculate predicted Nusselt numbers based on the relevant measured parameters.

A RELAP5(MOD3.3) model of the *test section and inlet development length* was used to qualtitatively estimate flow regime. The development length was modelled as a 20 cm long, 4.6 mm ID PIPE component with 20 volumes and the test section was modelled as a 93.2 cm long, 4.6 mm ID PIPE component with 40 volumes. A heat structure with uniform internal heating was coupled to the test section PIPE component using Inconel 600 properties from the expression by Novog *et al* to model the electrically heated test section walls [38]. Inlet mass flux, inlet fluid temperature and outlet pressure boundary conditions were taken directly from experimental measurements. This was an effective way to use the flow regime map that is used in RELAP5, based on the work of Taitel, Bornea, and Dukler [40, 41].

All fluid properties were based on the channel exit pressure and the local fluid temperature. Local fluid temperature was calculated by linearly interpolating the total energy added to the fluid by the test section at each measurement point and adding it to the enthalpy of the fluid at the inlet. The local enthalpy was then used to calculate the local temperature based on the outlet pressure. This approximation is valid because fluid properties vary strongly with temperature but weakly with pressure near 2.0 MPa. For example, varying the pressure $\pm 5\%$ near 2.0 MPa results in a negligible change in enthalpy whereas a $\pm 5\%$ change in temperature at 200°C produces an enthalpy change of the same relative magnitude.

Often the extrapolated fluid temperature near the end of the test section's heated length exceeded the measured outlet temperature of the fluid. This is consistent with the possibility that the copper bus bars may act as significant heat sinks, especially at the test section outlet where the fluid is hottest.

As discussed in Section 4.3, a heat balance was calculated as a per cent difference of the measured fluid power from the electrical power. Fluid power was determined by finding the enthalpy of the fluid at the inlet and outlet based on the local fluid temperature and pressure measurements. The enthalpy difference divided by the mass flow rate gave the fluid power in kW.

5.2 Single Phase Convection

Single phase data points that had $T_w - T_b$ less than 15°C were excluded from the analysis. Since the fluid temperature and wall temperature uncertainties are on the order of 3°C for 95% confidence levels, heat transfer coefficients evaluated from data with temperature differences less than 15°C would have an uncertainty, to the same level of confidence, on the order of 40% or more due to temperature measurements alone.

Figures 5.1–5.3 show the results of comparisons of the single phase convection data against the Dittus-Boelter, Gnielinski and Petukhov-Popov correlations respectively. The two distinct groupings evident in these plots represent the blocks of experiments with the same mass flux. The variation of predicted values in each group represent deviations in inlet mass flux and differing fluid properties that vary with the local fluid temperature.

Table 5.1 shows a quantitative comparison of the experimental results to the Petukhov-Popov, Gnielinski, and Dittus-Boelter correlations. The data used for the comparison had heat balance errors of less than ±2%. It is evident that all three correlations underpredict heat transfer for shorter heated lengths and overpredict it for longer heated lengths. The 'all' column represents data collected at axial locations 4, 24, and 44 cm from the test section outlet.

L-z (cm) *(# of data)*	**44** (6)	**24** (6)	**4** (6)	**all** (18)
Petukhov	-14.7% ±6.1%	-3.2% ±8.5%	10.2% ±5.8%	-2.6% ±12.3%
Gnielinski	-6.5% ±6.7%	5.2% ±9.3%	19.1% ±6.2%	6.0% ±12.8%
Dittus–Boelter	-7.4% ±6.7%	5.0% ±8.4%	18.5% ±5.4%	5.3% ±12.7%

Table 5.1: Quantitative comparison of single phase heat transfer correlations for the experimental data gathered with absolute heat balance errors of less than 2%

The data in Figure 5.4 is grouped by axial location on lines of nearly constant slope. This can be verified quantitatively by examining Table 5.1. As heated length

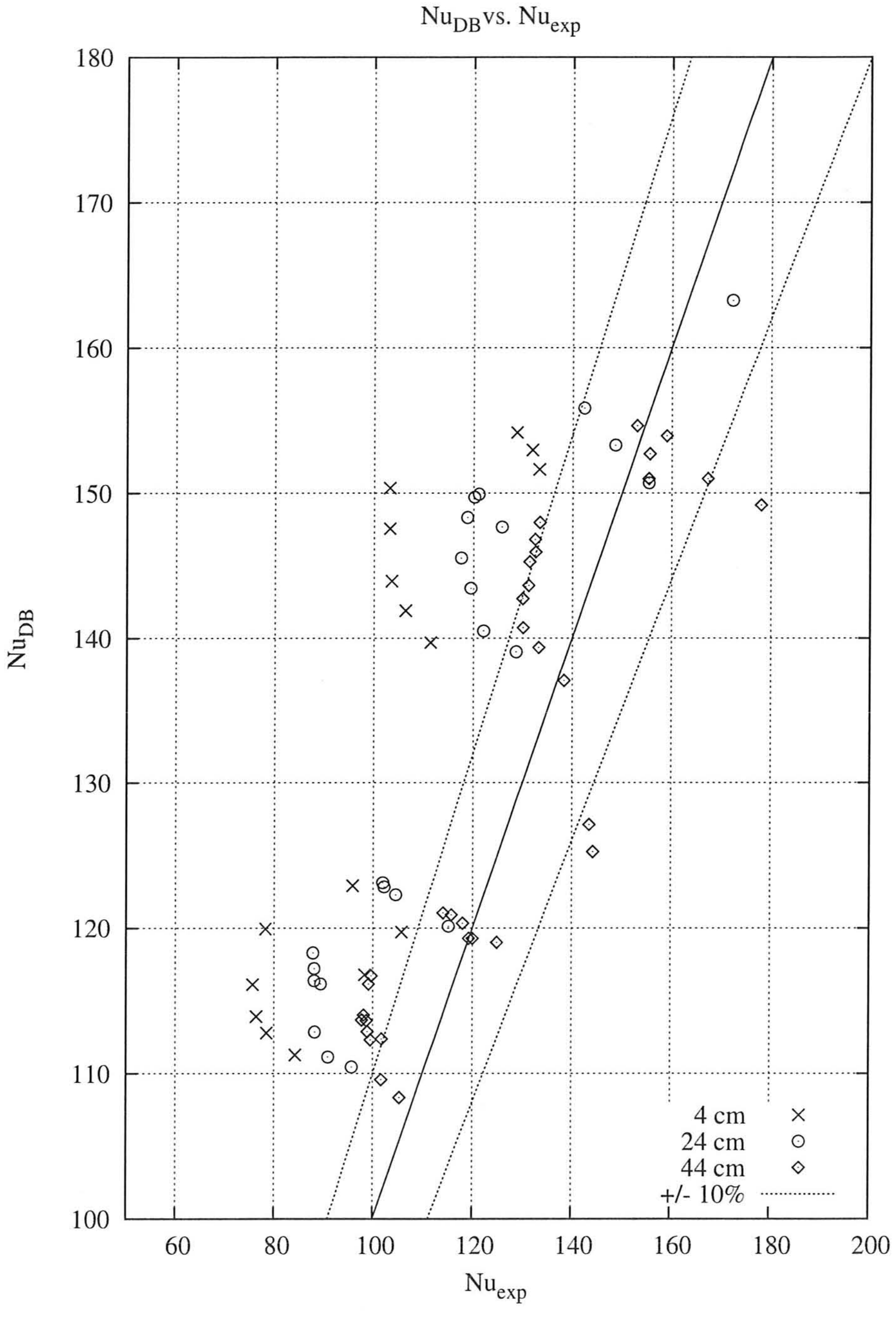

Figure 5.1: Comparison of experimental results to the Dittus-Boelter correlation for single phase convective heat transfer

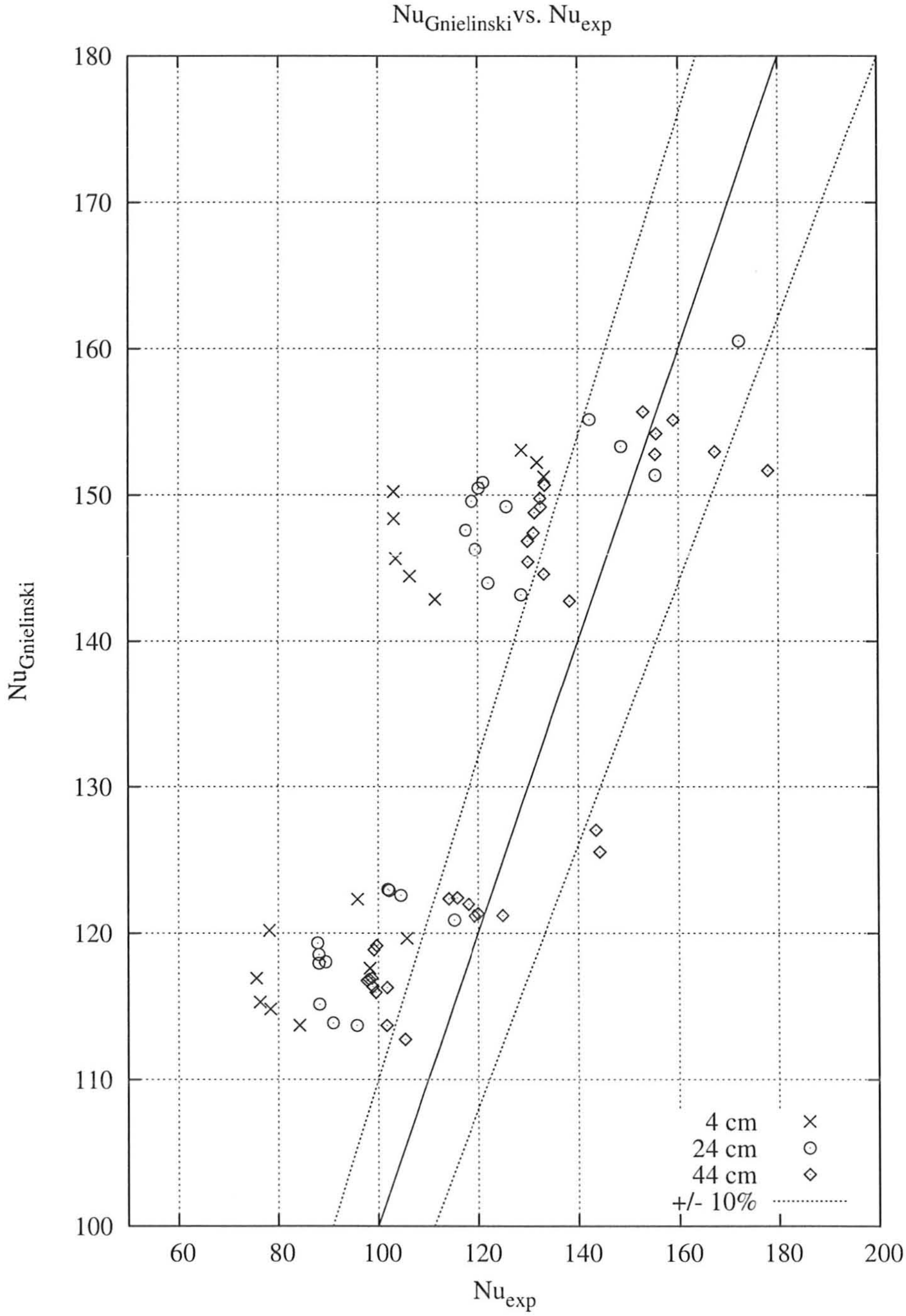

Figure 5.2: Comparison of experimental results to the Gnielinski correlation for single phase convective heat transfer

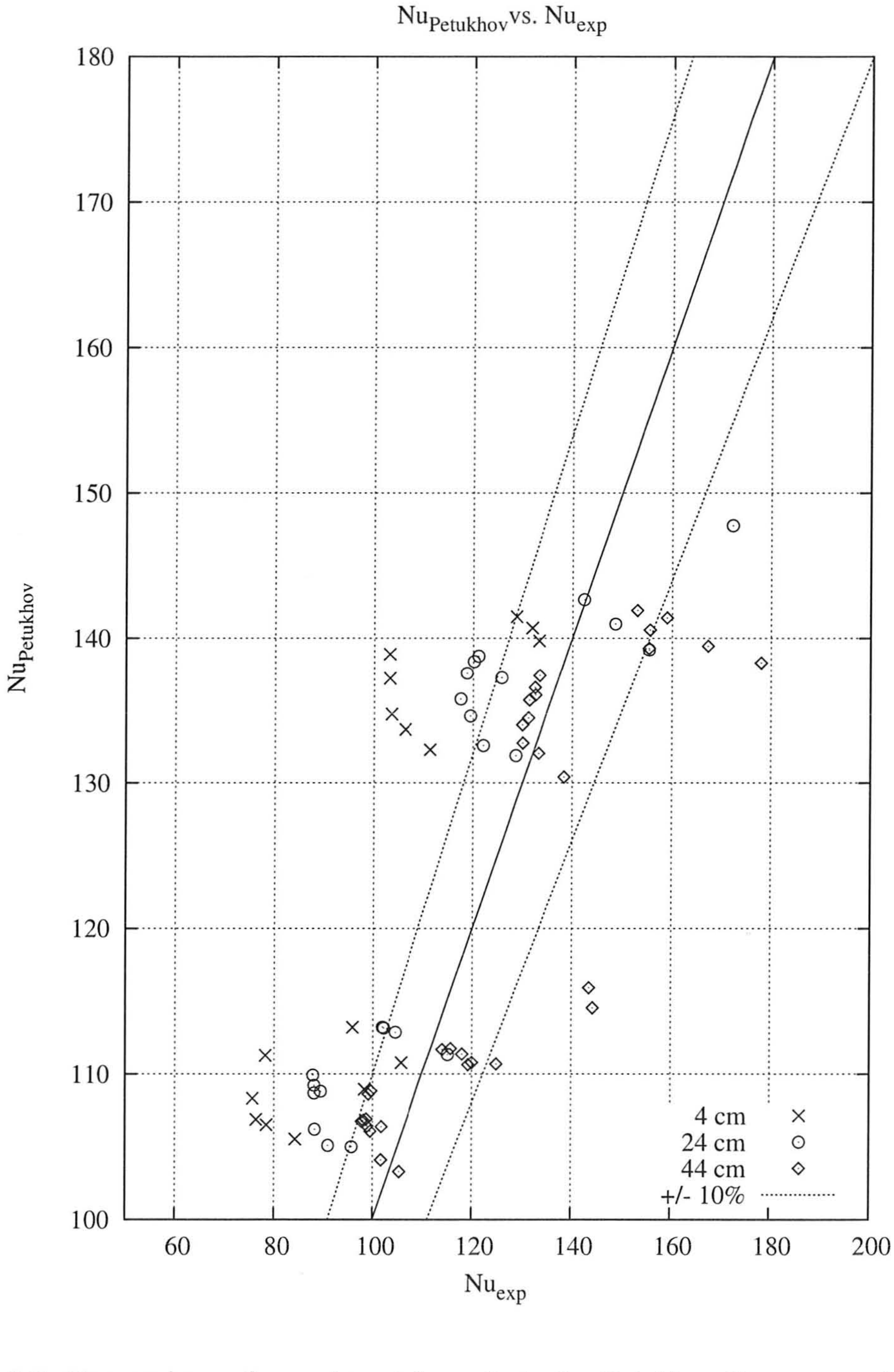

Figure 5.3: Comparison of experimental results to the Petukhov-Popov correlation for single phase convective heat transfer

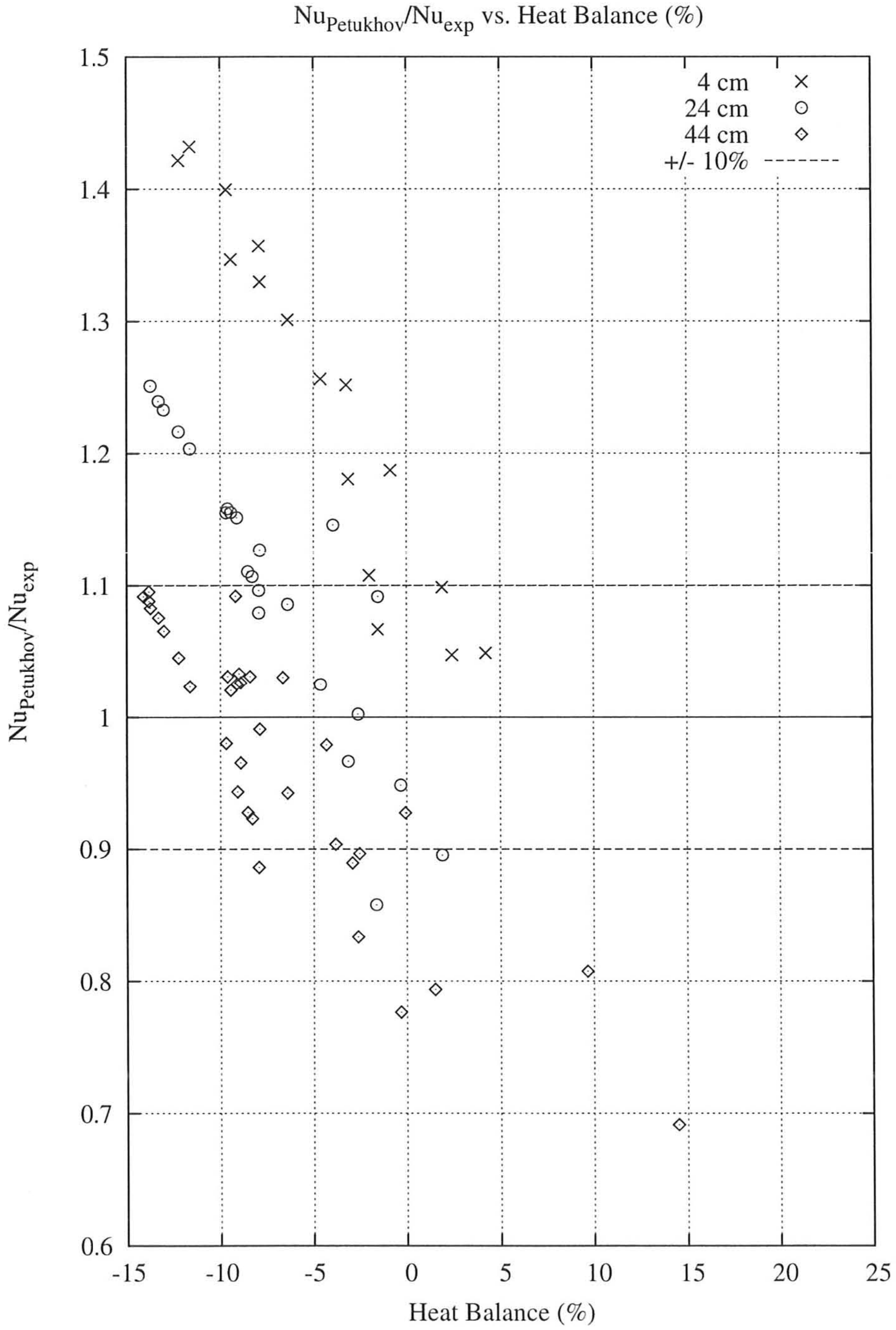

Figure 5.4: Comparison of experimental results to the Petukhov-Popov correlation as a function of the heat balance (%)

increases, the experimental values shown in Figures 5.3 and 5.2 may misrepresent the 'actual' experimental values of Nu. This is because as heat losses increase with power the assumption that the outside wall of the test section was perfectly insulated became less true. The Petukhov-Popov and Gnielinski correlations may overpredict local Nusselt numbers for the longest heated lengths by a greater margin than what is indicated in Table 5.1.

The test section was well insulated from the inlet to the first upstream thermocouple location 44 cm from the test section outlet. After this point the insulation is less robust. It was difficult to apply thermal insulation in between closely-spaced thermocouples without damaging their mechanical contact with the test section. In the poorly insulated region of the test section the wall heat flux and fluid temperature may be overestimated using the assumption that the outer wall heat flux is zero. Underprediction of the local fluid temperature could result in poor estimation of strongly temperature dependent fluid properties leading to poor correlation predictions. Heat losses also contribute to biases in the inside wall temperature as outlined in Section 3.3.7.

Another factor that may influence the predictive accuracy of correlations is the difficulty in quantifying the effect of axial and radial temperature gradients within the fluid at different positions along the heated length. Since the fluid is heated as it flows along the test section axis the bulk temperature continuously increases until saturation is reached. The temperature gradient within the boundary layer constantly changes along the heated length. This observation of the effect of fluid property gradients in single phase convection is consistent with the observations of Novog [42].

The Gnielinski correlation contains a wall temperature correction factor based on the ratio of Pr at the bulk fluid temperature compared to the wall temperature. This term considerably complicates the calculation procedure because it requires iteration and does not yield better predictions of Nu. It also contains a heated length correction factor which also does not appear to improve its prediction capability.

5.3 Subcooled Boiling

Data points that had a wall superheat of at least 5°C and that had an equilibrium quality of less than 0.0 were selected as 'subcooled boiling' data points. The 5°C threshold was chosen by visually inspecting the individual boiling curves. Using this threshold eliminated most single phase data points with small wall superheats from the subcooled boiling data without excluding any partial nucleate boiling points. Data was largely in the bubbly flow regime except for data with very low local subcooling where it was estimated the slug flow regime occurred.

5.3.1 Comparison with Existing Correlations

Figures 5.5–5.10 show comparisons of the experimental data to several subcooled boiling correlations: those of Jens-Lottes, Thom *et al*, Thom *et al* as modified by Novog [42], Rassokhin *et al*, Labuntsov, and Yin *et al*. Table 5.2 shows the statistical analysis of each correlation in comparison with the experimental data for each heated length; the 'all' column represents the data collected 4, 24, and 44 cm from the end of the heat length only.

Based on the results shown in Table 5.2 it is evident that most of the correlations

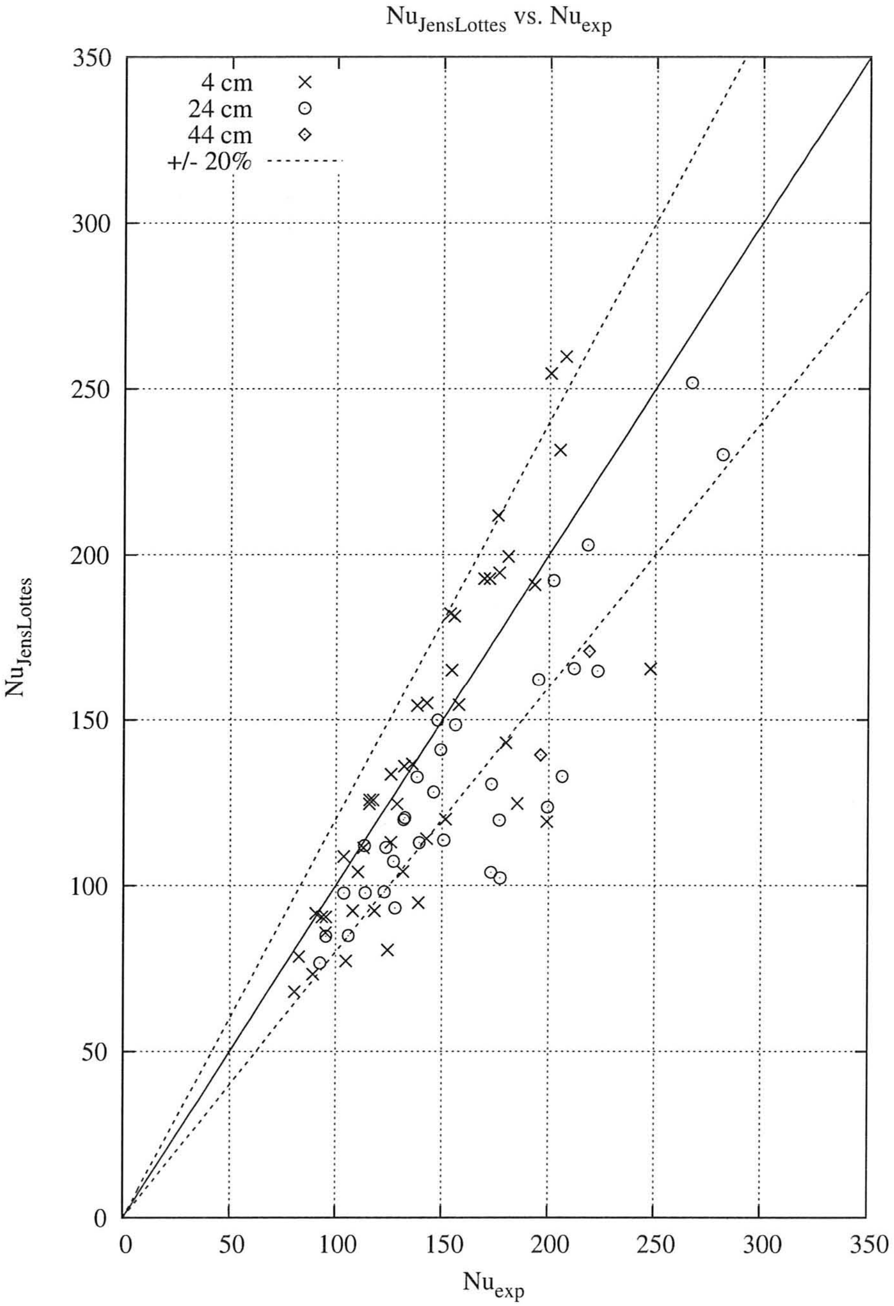

Figure 5.5: Comparison of experimental results to the Jens-Lottes subcooled boiling correlation

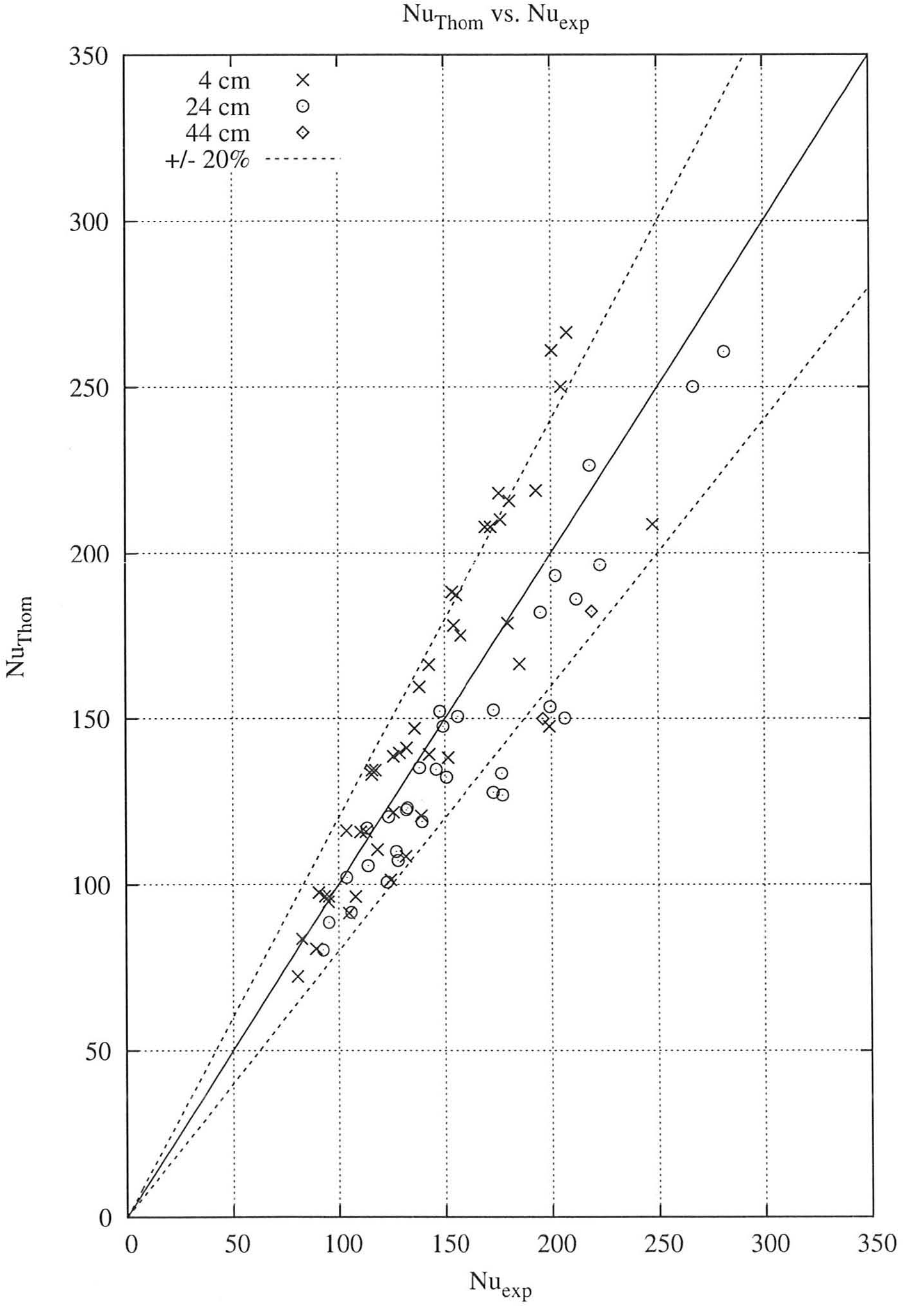

Figure 5.6: Comparison of experimental results to the Thom *et al* subcooled boiling correlation

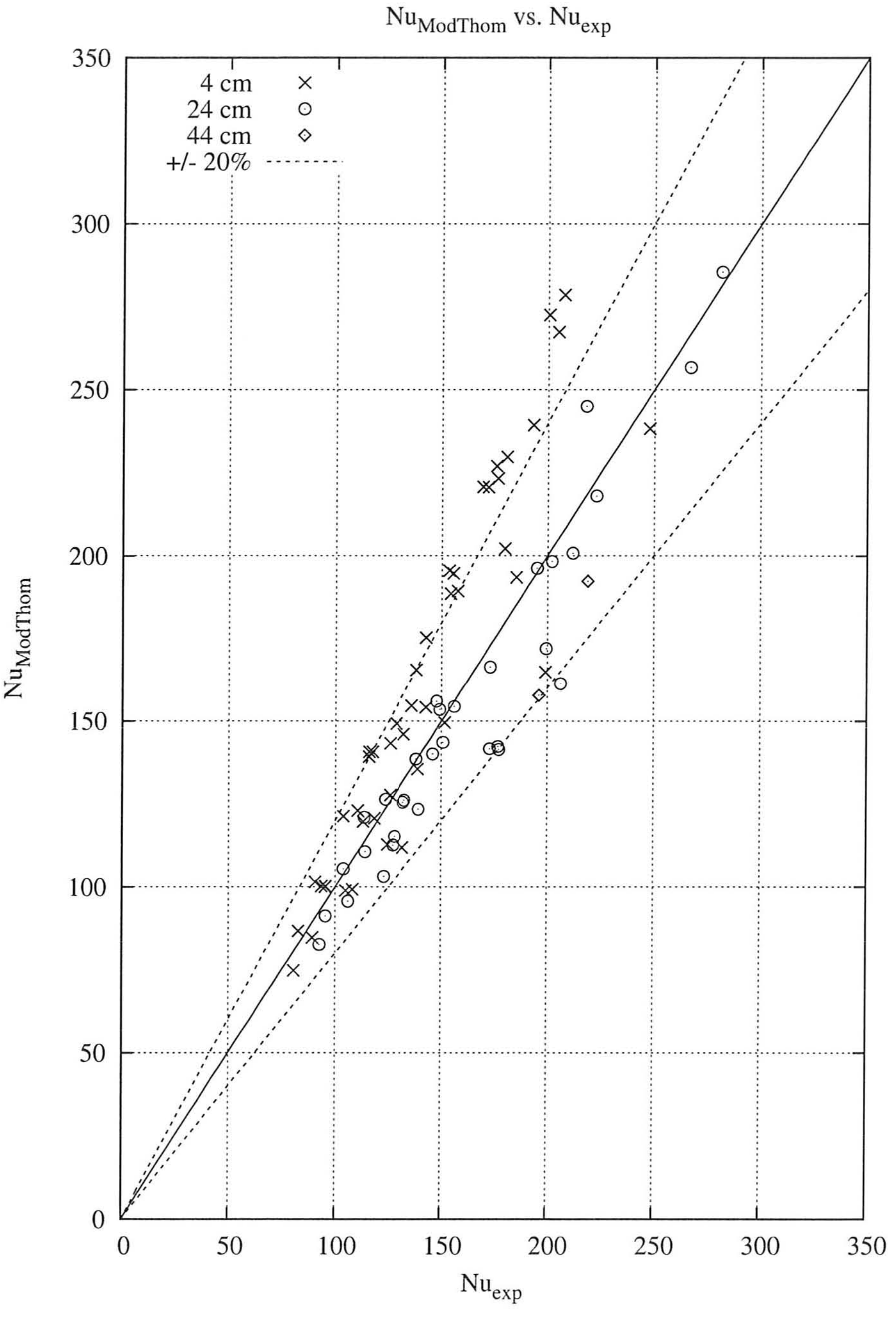

Figure 5.7: Comparison of experimental results to the Thom *et al* subcooled boiling correlation as modified by Novog

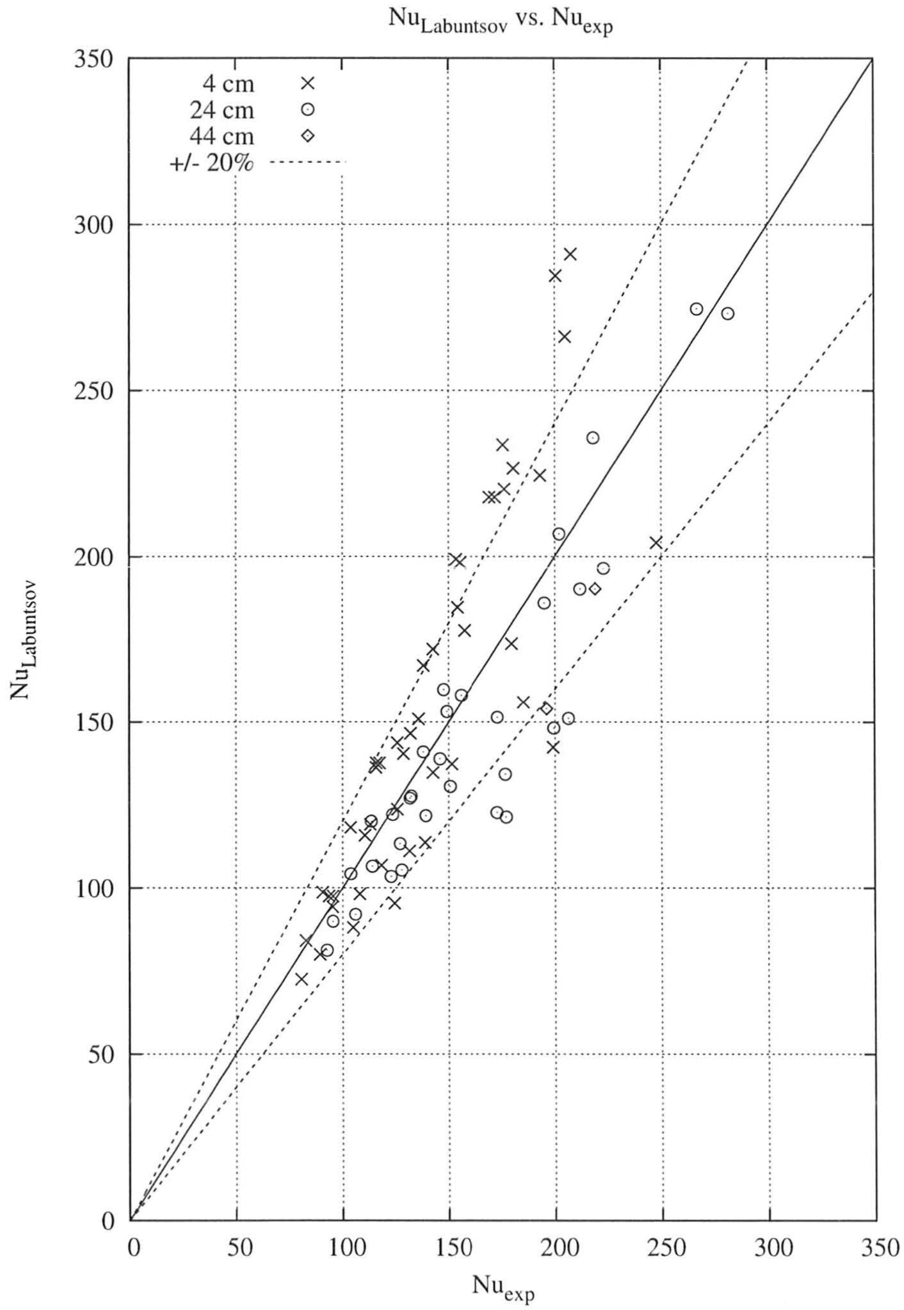

Figure 5.8: Comparison of experimental results to the Labuntsov subcooled boiling correlation

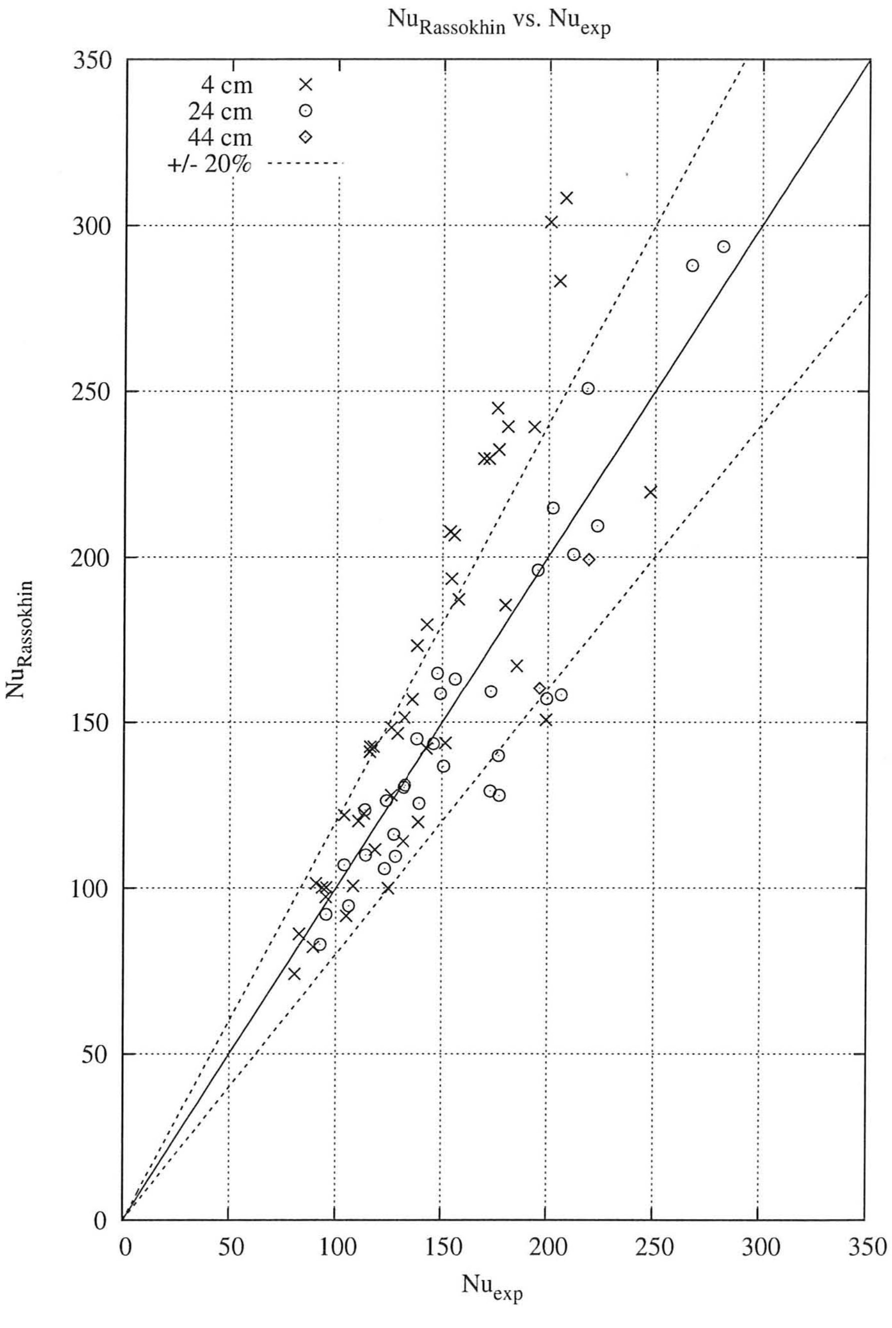

Figure 5.9: Comparison of experimental results to the Rassokhin *et al* subcooled boiling correlation

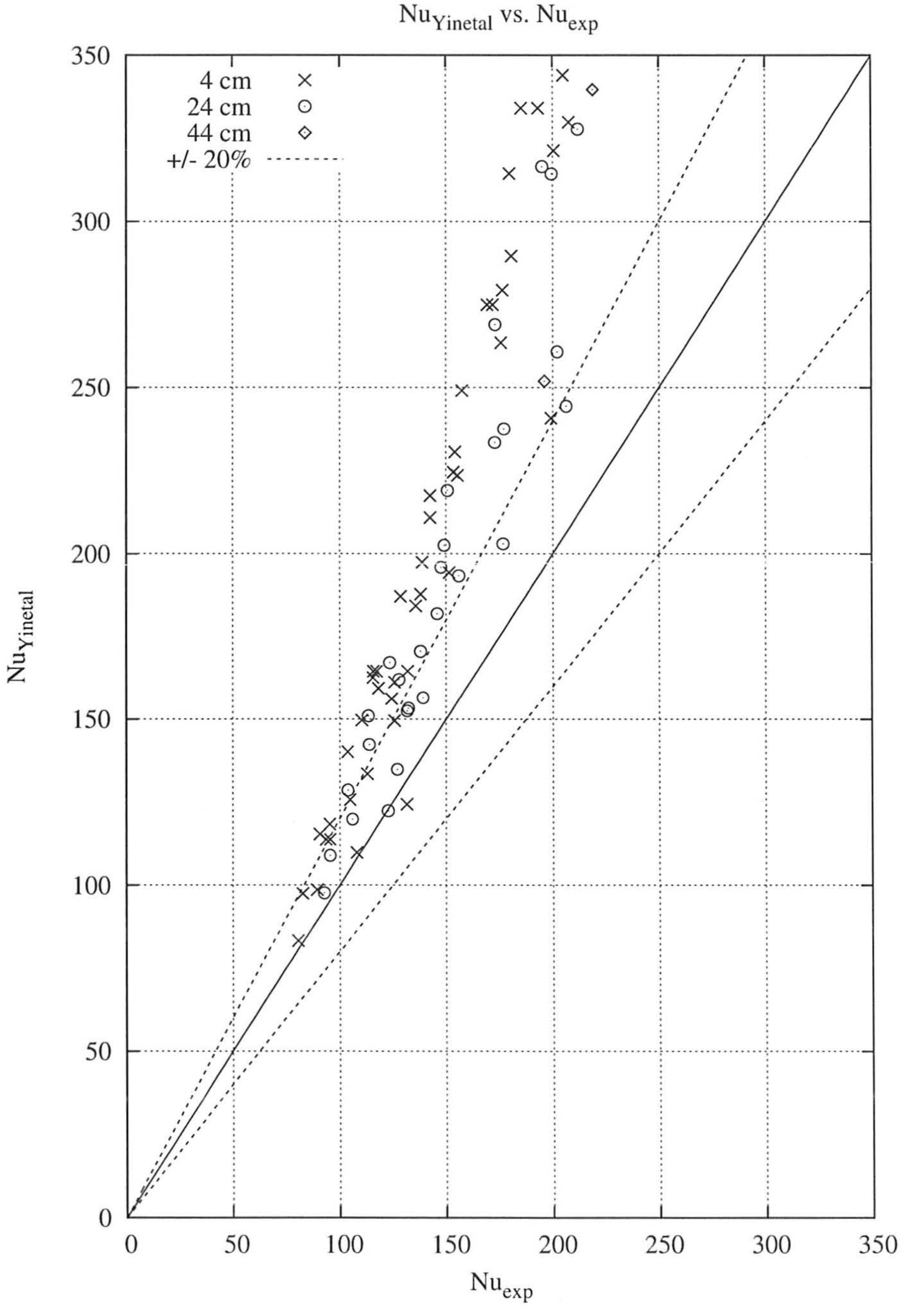

Figure 5.10: Comparison of experimental results to the subcooled boiling correlation of Yin *et al*

underpredict the majority of the experimental Nusselt numbers except that of Yin *et al.* The level of underprediction decreases with heated length. The standard deviation of the data increases with heated length for the thermocouples located 44, 24, and 4 cm from the test section outlet but this may be related to the number of data points at each position rather than the heated length.

In Figures 5.5–5.10 many of the values are grouped in the region of relatively 'lower' Nusselt numbers. Both partial and fully developed boiling are included in the data sets shown here. The data for heated lengths 24 cm or more from the test section outlet are dominated by partial nucleate boiling. For the limited range of parameters over which it occurs partial nucleate boiling corresponds to slightly higher Nusselt numbers than fully developed boiling. Therefore data for longer heated lengths may be skewed towards partial nucleate boiling. This is likely the main reason why most of the correlations underpredict the data, especially for shorter heated lengths.

L-z (cm) *(# of data)*	**44** (2)	**24** (33)	**4** (45)	**all** (80)
Jens-Lottes	-25.5% ±4.9%	-17.9% ±12.8%	-3.6% ±17.2%	-10.1% ±6.9%
Thom	-20.1% ±4.8%	-11.2% ±10.1%	0.5% ±14.1%	-2.0% ±15.1%
Thom [42]	-15.9% ±5.2%	-6.3% ±9.5%	12.0% ±13.9%	-3.8% ±15.3%
Rassokhin	-13.7% ±6.5%	-5.6% ±12.2%	12.4% ±18.9%	-4.3% ±18.6%
Labuntsov	-17.3% ±5.9%	-9.3% ±12.0%	7.6% ±17.8%	-0.03% ±17.7%
Yin	41.7% ±18.7%	33.3% ±26.5%	39.0% ±20.3%	36.7% ±23.0%

Table 5.2: Mean error and standard deviation of experimental results compared with correlations

For higher values of Nu calcualted from data gathered 4 cm from the test section outlet, subcooled boiling correlations largely overpredict Nu. This can be seen in Figures 5.5–5.10. All but one of the subcooled boiling data points at this location with Nu greater than 157 correspond to conditions that had locally reached OSV. It is possible that once this condition is reached the intensity of nucleate boiling decreases and further increases in Nu are due to other phenomena.

The analysis regarding heat losses in Section 3.3.7 also pertains to the experimental values of Nu for subcooled boiling. The effect may be even more exaggerated for boiling since it corresponds to higher heat fluxes. Therefore the level of underprediction by some correlations shown in Table 5.2 may have been overestimated.

5.3.2 Parametric Trends

Figure 5.11 shows heat flux plotted against wall superheat. It is evident that these two parameters are positively correlated. Data from different heated lengths largely lie on separate lines of constant slope which suggest that there is a heated length or local subcooling effect on wall superheat. This also suggests that flow regime did not significantly affect heat transfer because there is no significant deviation of the data for high heat fluxes or wall superheats where the slug flow regime was predicted.

Figures 5.12–5.15 show the effect of mass flow rate, inlet subcooling, local subcooling, and heated length on subcooled boiling by plotting those values against heat flux divided by wall superheat. There is a significant amount of scatter in each of these graphs; several different values of exponents were applied to the heat flux term on the dependent axis but this did not significantly change the amount of scatter. This can be seen by comparing Figures 5.15 and 5.16.

Observing the data taken 4 cm from the test section outlet in Figure 5.12 there is no dependence on mass flux or inlet subcooling. Figure 5.14 suggests that large values of subcooling result in high heat fluxes and/or low wall superheats but more data is necessary to confirm this. There is also an apparent decreasing trend with respect to heated length. There are very few data points for the location 44 cm from the test section outlet so more subcooled boiling data at this location is necessary.

The wall heat flux divided by wall superheat is nearly constant with respect to inlet and local subcooling for all but very high local subcoolings. This agrees with the correlations in Table 2.2 that are dependent only on wall superheat, heat flux, and pressure. The apparent increase in heat flux over wall superheat for very high subcoolings supports Shah's hypothesis that there is a subcooling 'threshold' above which subcooling does increase heat transfer. Heat flux over wall superheat is independent of mass flow rate. Shah and Kandlikar's correlations do contain dependencies on mass flux but they are *very* weak, on the order of mass flux to the exponent 0.1–0.3.

Inlet subcooling, local subcooling and heated length are all related to the radial fluid temperature gradient near the test section wall. As indicated previously in Section 3.3.7 this temperature gradient may be at least partially responsible for some of the observed effect of heated length. This effect may be more pronounced for subcooled boiling than for single phase convection or saturated boiling. Once the wall becomes superheated the axial gradient of the fluid temperature at the wall becomes negative because of the negative axial pressure gradient. At the same time the axial

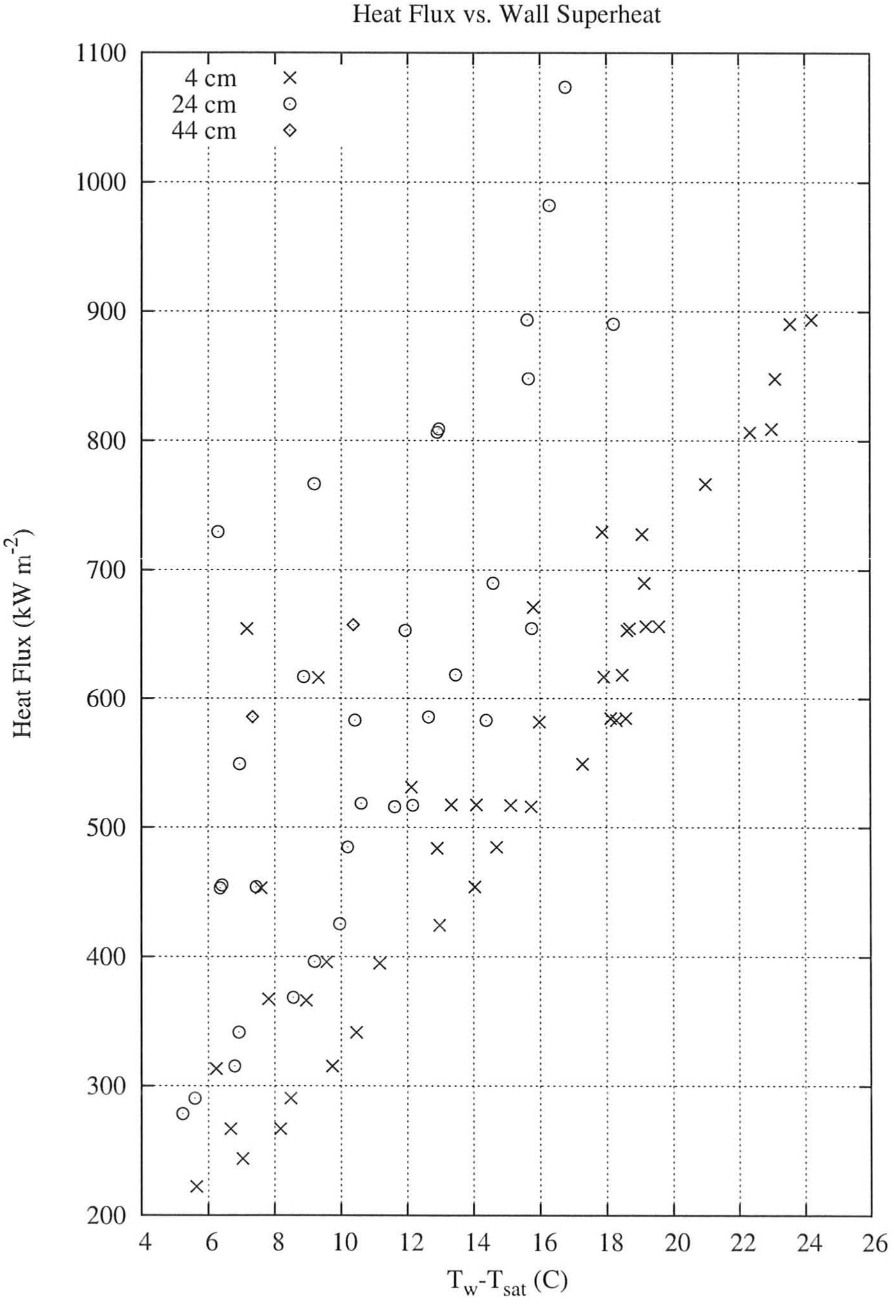

Figure 5.11: Heat flux plotted against wall superheat

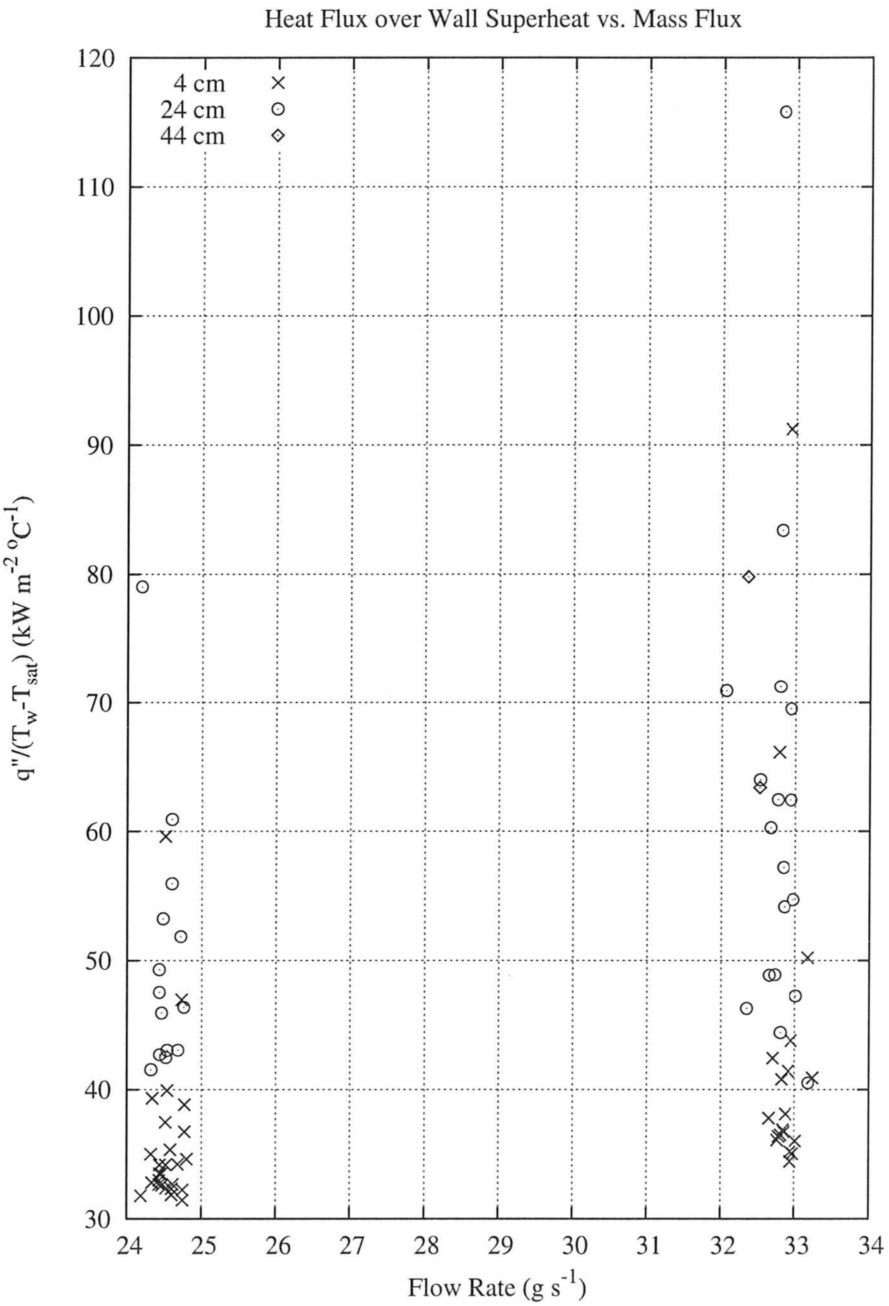

Figure 5.12: Heat flux divided by wall superheat plotted against mass flow rate (g/s)

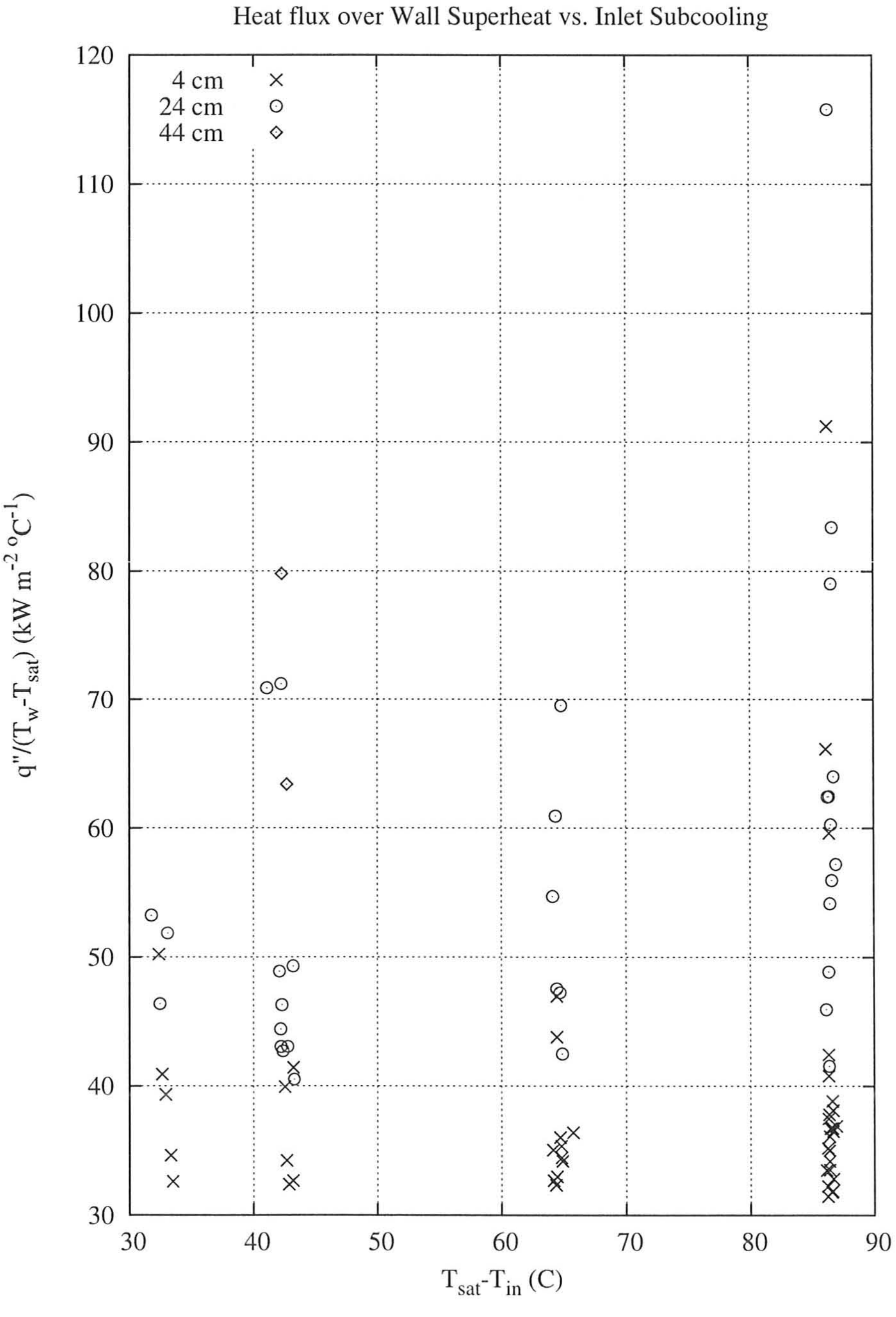

Figure 5.13: Heat flux divided by wall superheat plotted against inlet subcooling

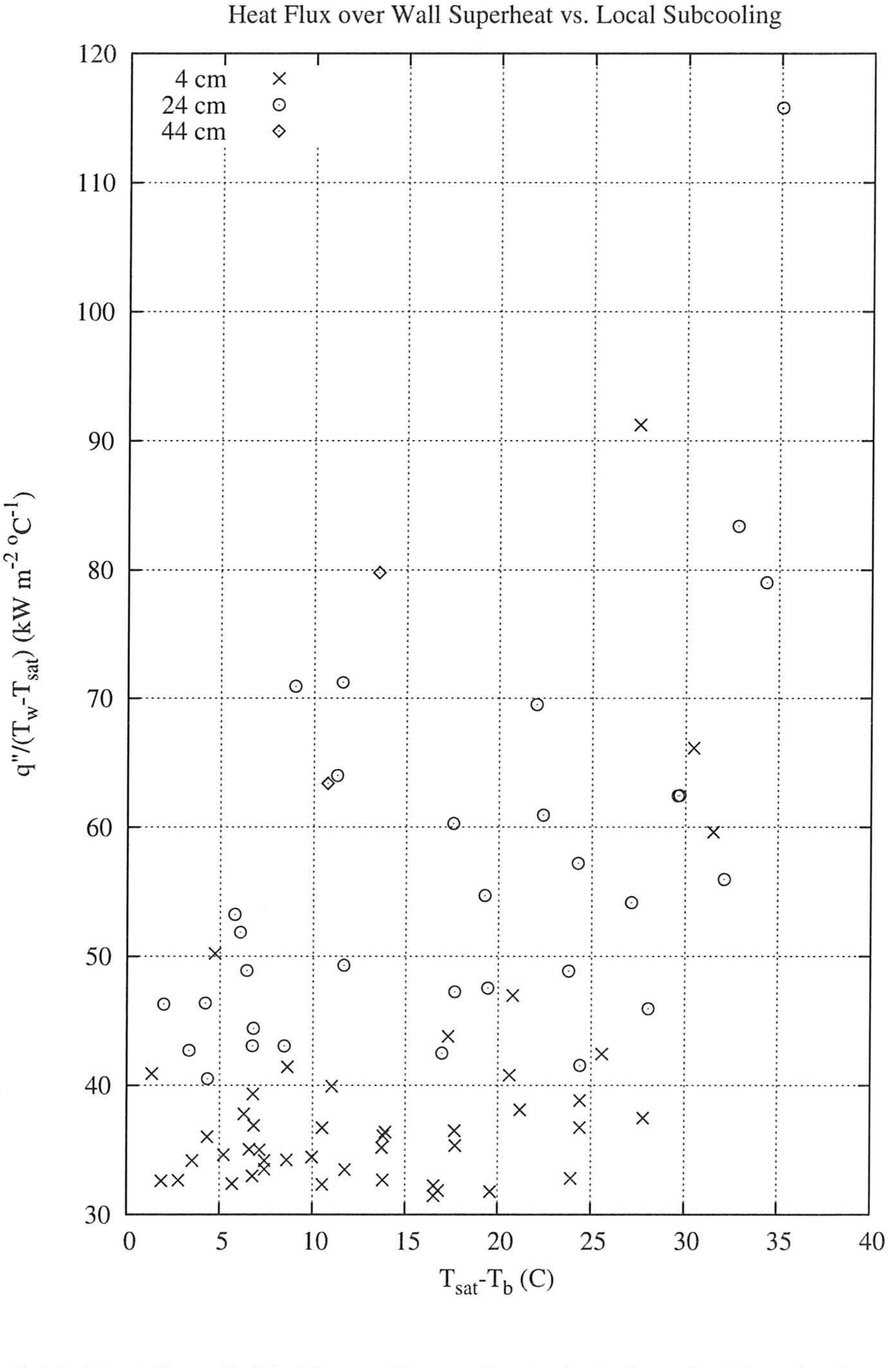

Figure 5.14: Heat flux divided by wall superheat plotted against local subcooling

gradient of the bulk fluid temperature is positive. The overall effect is that the radial temperature profile becomes increasingly flattened until the bulk fluid becomes saturated. For high values of inlet subcooling the axial fluid temperature gradient will be large because as inlet subcooling increases so does the wall heat flux necessary to reach superheated temperatures. Increased inlet subcooling increases the axial gradient of changes in the thermal boundary layer.

As indicated above, many subcooled boiling correlations express wall superheat independently of local subcooling. Therefore the present data, which shows that wall superheat is mostly independent of subcooling, is consistent with the data used to develop those correlations.

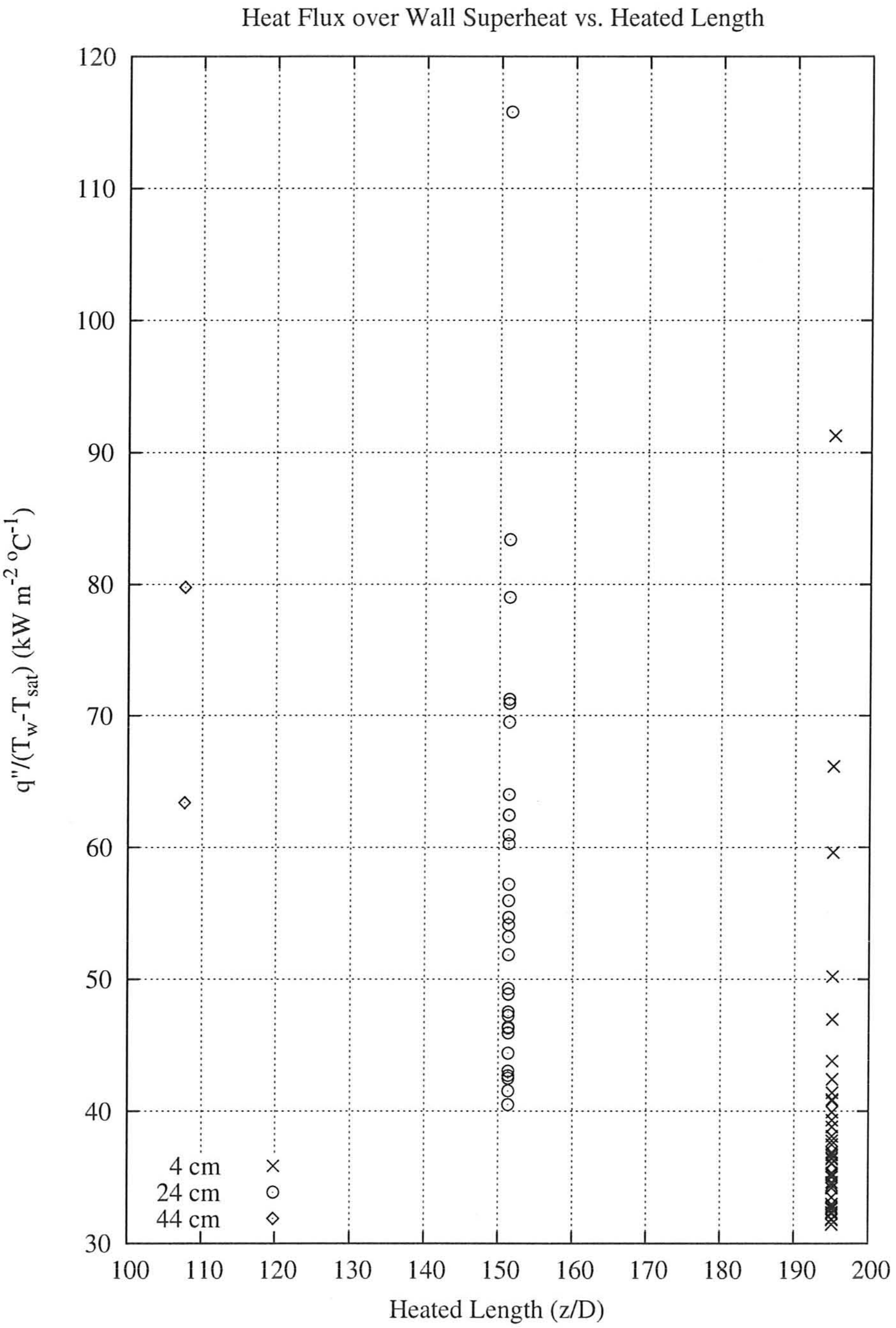

Figure 5.15: Heat flux divided by wall superheat plotted against heated length (1 diameter = 4.6 mm)

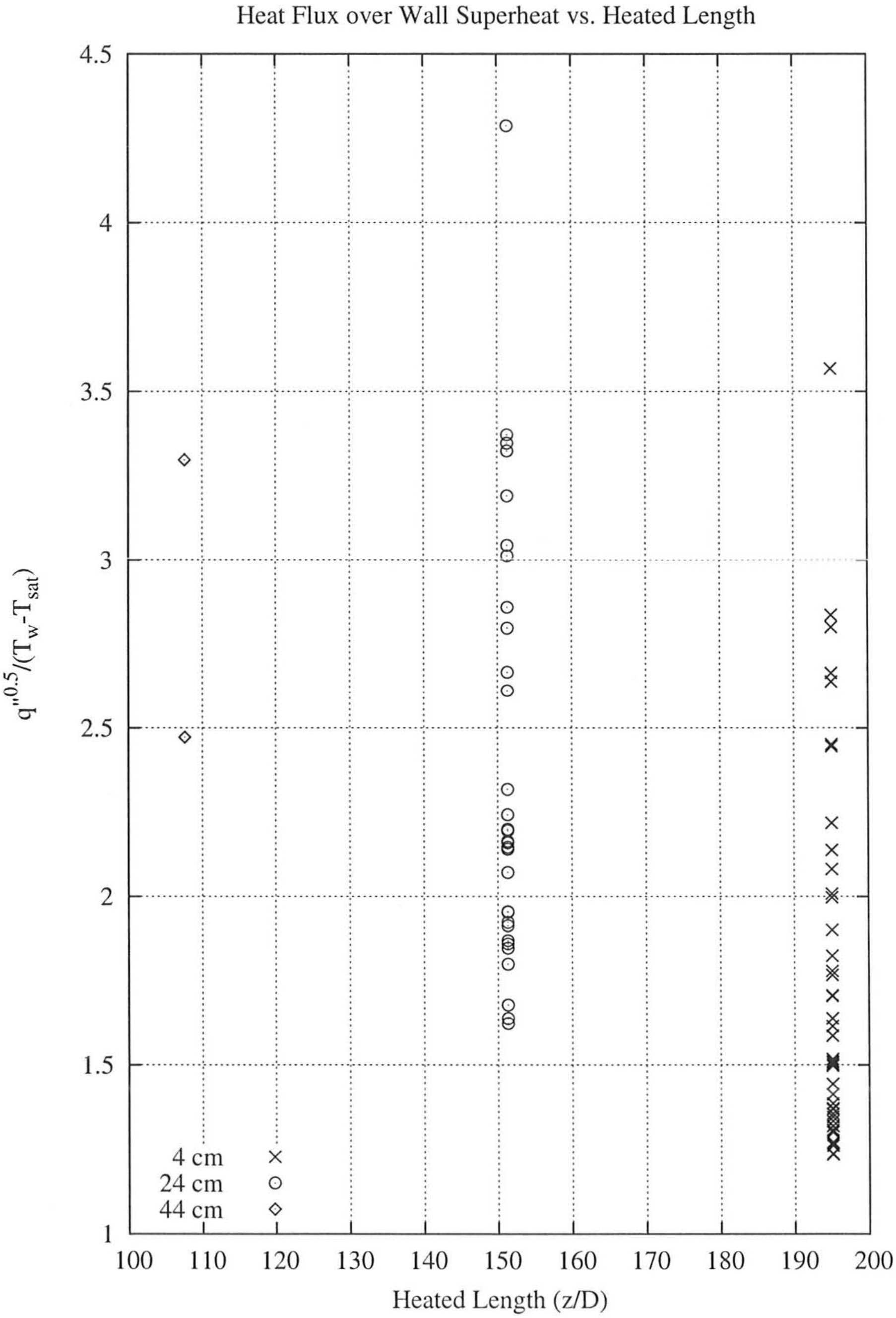

Figure 5.16: Heat flux to the one half power divided by wall superheat plotted against heated length (1 diameter = 4.6 mm)

5.4 Saturated Boiling

Saturated boiling data were selected based on the Saha-Zuber criteria for OSV as recommended by Kandlikar. Roughly half of the saturated data presented here correspond to what Kandlikar terms the 'Significant Void Flow' region where OSV has been reached but the bulk fluid has not yet reached saturation. All but one of the data points measured 24 cm from the test section outlet are in this region. For the thermocouples positioned 4 cm from the test section outlet the distribution of data is even between thermodynamically saturated data and 'Significant Void Flow'. Where required in the correlations flow quality as defined in Equation 2.2 has been used in place of equilibrium quality.

The flow regimes for the saturated boiling data were estimated to be bubbly for the most subcooled 'Significant Void Flow' data, slug flow for data near saturation, and annular flow for the highest local qualities.

5.4.1 Comparison with Existing Correlations

Figures 5.17 and 5.18 show a comparison of measured Nusselt numbers for saturated boiling compared with the modified Chen and Steiner-Taborek correlations, respectively. As in the previous sections the 'all' data column includes the data taken 4, 24, and 44 cm from the test section outlet.

The mean and standard deviations of the data in comparison to the modified Chen and the Steiner-Taborek correlations can be found in Table 5.3. As for the subcooled boiling data the prediction seems to be 'best'—with the lowest standard deviation—for the shortest heated length for which there is data available but this may also be due to the difference in the number of data points for the two posi-

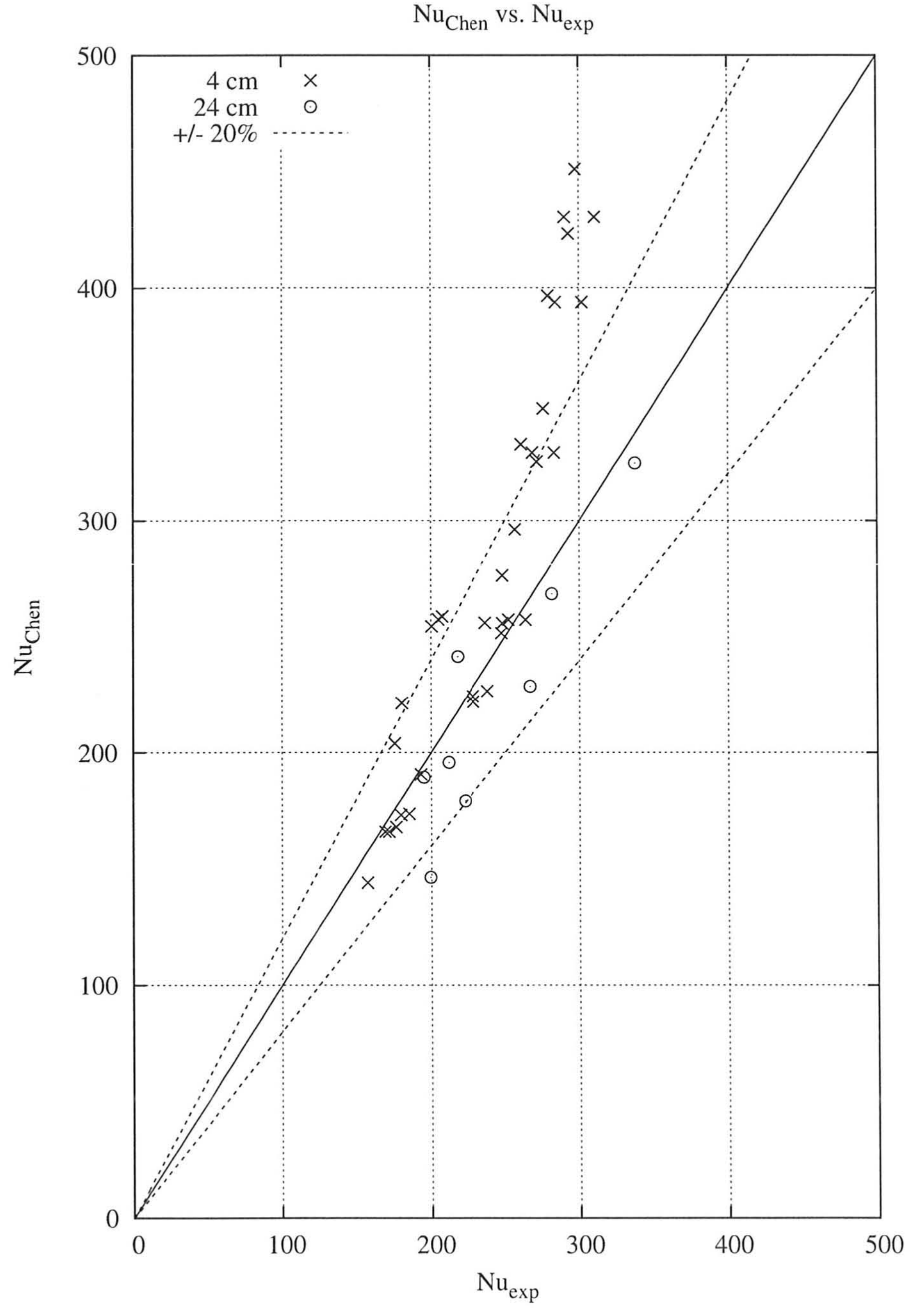

Figure 5.17: Comparison of experimental results to the modified Chen correlation for saturated flow boiling

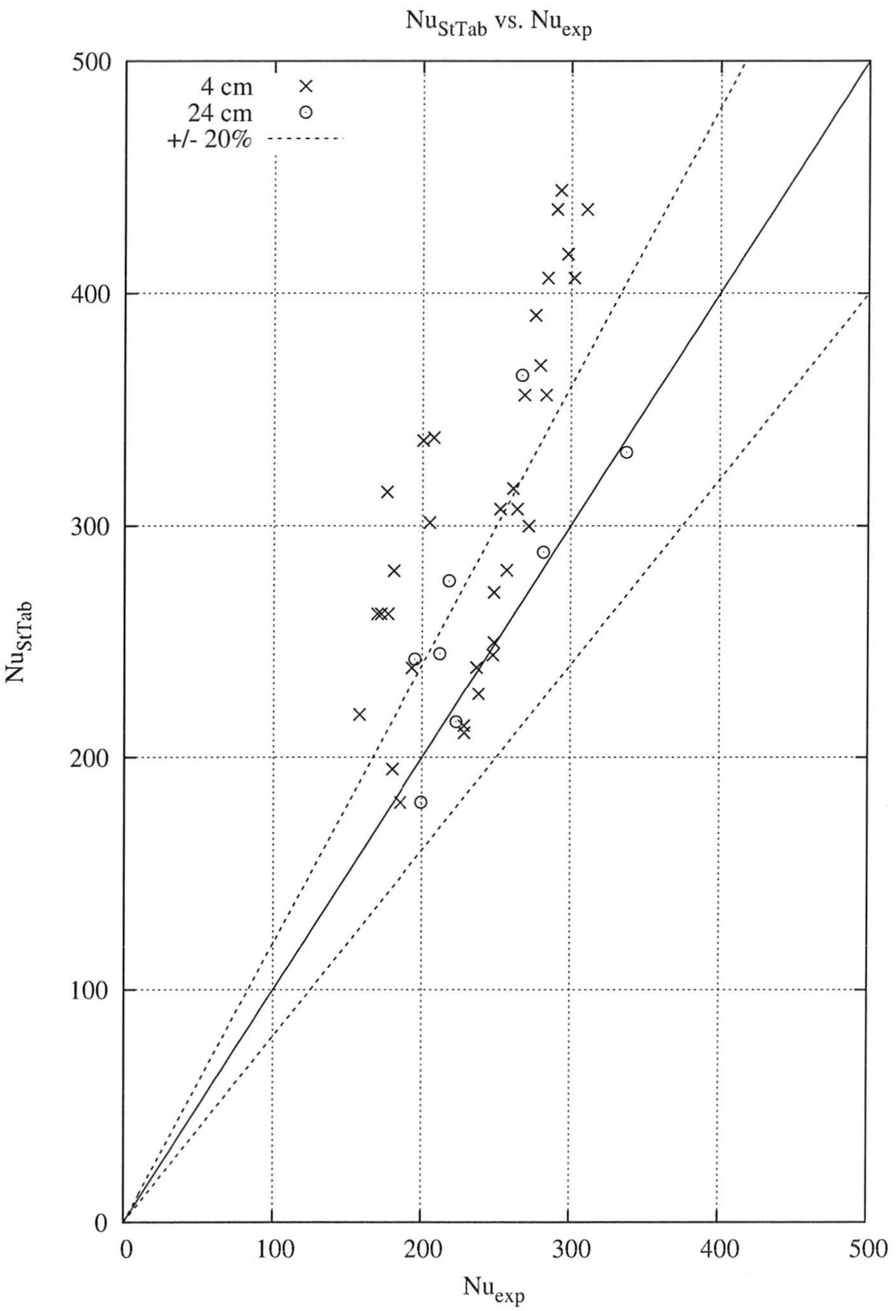

Figure 5.18: Comparison of experimental results to the correlation of Steiner and Taborek for saturated flow boiling

L-z (cm)	**44**	**24**	**4**	**all**
# of data	(0)	(9)	(34)	(43)
Chen	–	-12.05%	15.3%	9.6%
	–	±14.9%	±18.0%	±20.6%
Steiner-Taborek	–	12.0%	29.3%	25.7%
	–	±15.8%	±23.7%	±23.2%

Table 5.3: Mean and standard deviation for comparisons of saturated boiling data with the Chen and Steiner-Taborek correlations

tions. Nu values 4 cm from the test section outlet are overpredicted while Nu is underpredicted 24 cm from the test section outlet.

The modified Chen correlation tends to overpredict the convective enhancement factor F relative to Chen's original graphical correlation for small values of X_{tt}^{-1}. The value of F predicted by the 'analytic' expression lies at the 'upper limit' of the region of experimental data used to derive the graphical correlation [31]. This may account for some of the overprediction of the Chen correlation especially since the mass qualities for all the present data are very small.

In Figures 5.17 and 5.18 the values of the experimental Nusselt number approach an apparent 'limiting value'. The value of Nu predicted by both the modified Chen and Steiner-Taborek correlations increases while the 'measured' value increases much more slowly. This may be due to increasing heat losses as heat flux increases; this is unlikely because heat losses tend to result in *over*estimated experimental values of Nu as outlined in Section 3.3.7.

5.4.2 Parametric Trends

Figures 5.19–5.23 demonstrate the dependence of the saturated boiling data on heat flux, inlet temperature, mass flow rate, equilibrium quality, and heated length. Figure 5.19 shows that plotting heat flux against wall superheat collapses the data onto lines of constant slope for each heated length. It is evident from this figure that the 'saturated' boiling data presented here behaves similarly to the subcooled boiling data presented in the previous section. Although three different flow regimes were predicted for the saturated boiling there is no significant deviation or incontinuity in the data as heat flux and wall superheat increase. Therefore it is evident that flow regime did not have a strong effect on the experimental data if the flow regime transition predictions are correct. For these reasons the data in this section is presented in the same manner as for subcooled boiling: wall heat flux divided by wall superheat were plotted against each of the variables to determine if any dependence exists.

The equilibrium mass qualities of the saturated data are very near zero and range from slightly negative, for the data selected on the basis of having reached OSV, to 0.07. This can be seen in Figure 5.20. This figure also indicates that, for the data collected 4 cm from the test section exit, the wall superheat and heat flux increase monotonically once equilibrium quality reaches 0.

There is an apparent trend of heat flux over wall superheat decreasing with inlet subcooling in Figure 5.21. This may be attributed to larger temperature gradients in the thermal boundary layer for higher values of subcooling. Keeping mass flow rate constant, saturation is reached at higher heat fluxes for greater subcoolings resulting in larger wall superheat required for nucleate boiling to begin. In this case the bulk fluid temperature at an axial location along the test section may be saturated but the 'body' of the fluid outside the boundary layer is slightly subcooled which may suppress bubble growth and boiling heat transfer enhancement.

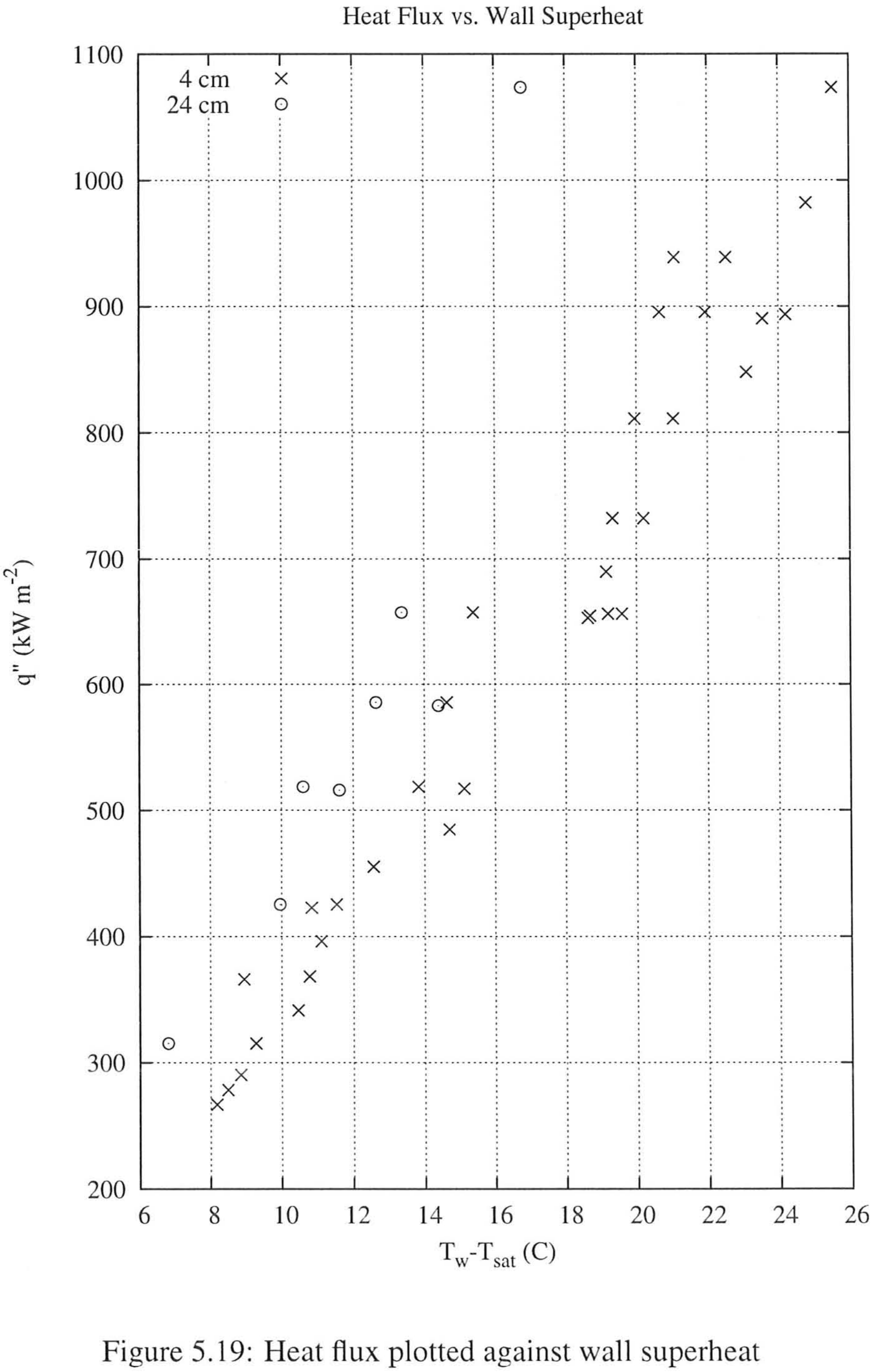

Figure 5.19: Heat flux plotted against wall superheat

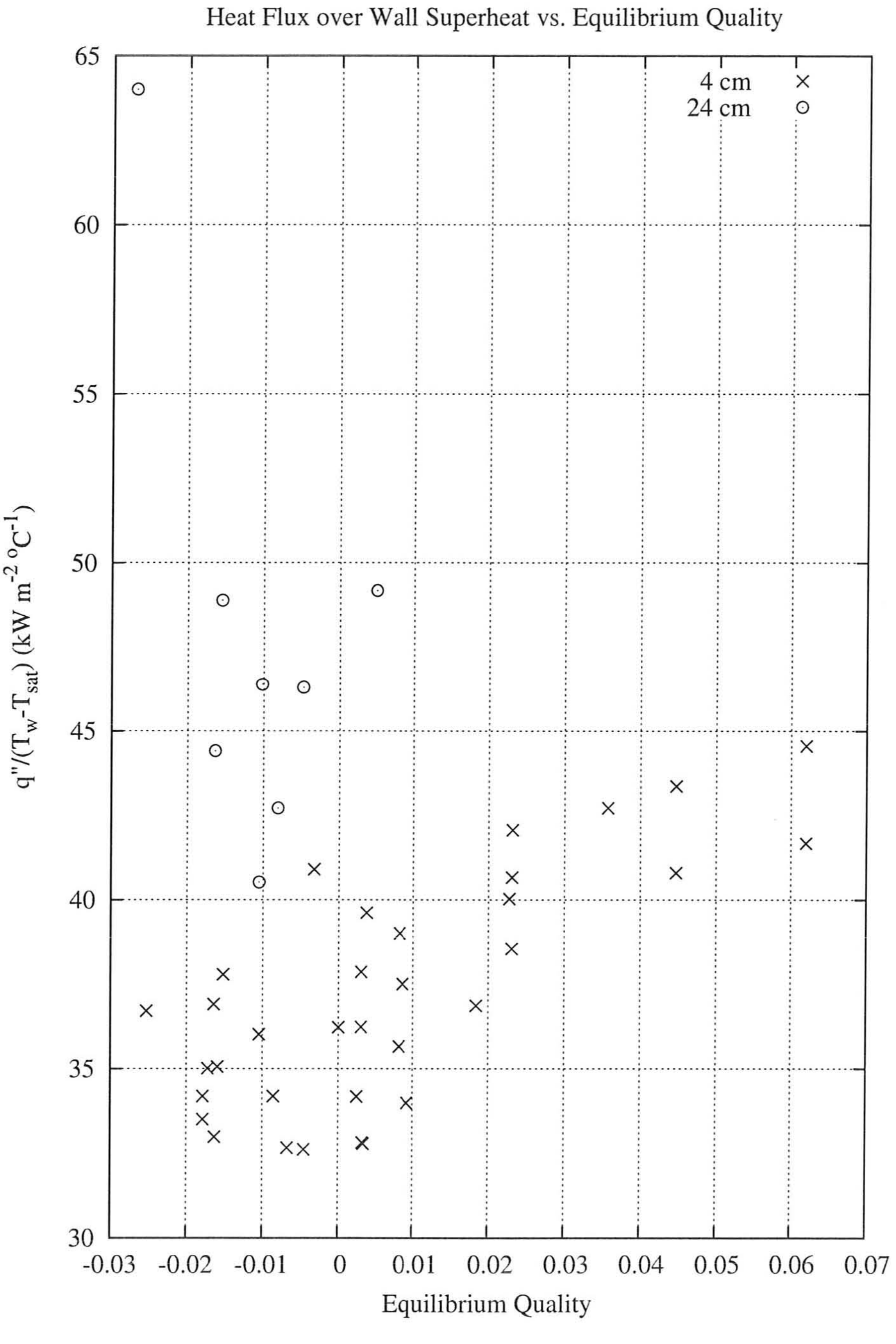

Figure 5.20: Heat flux over wall superheat plotted against equilibrium quality

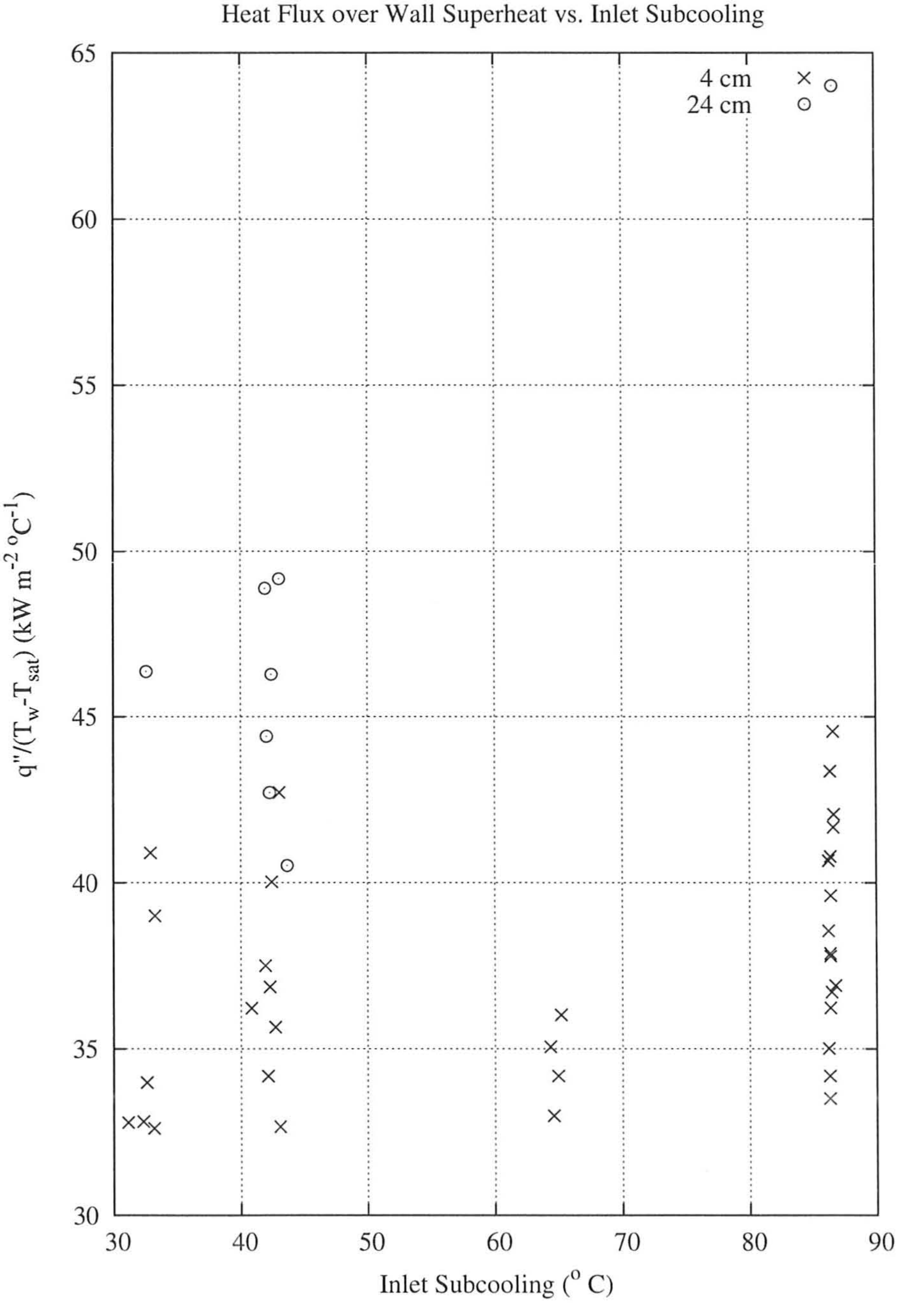

Figure 5.21: Heat flux over wall superheat plotted against inlet temperature (C)

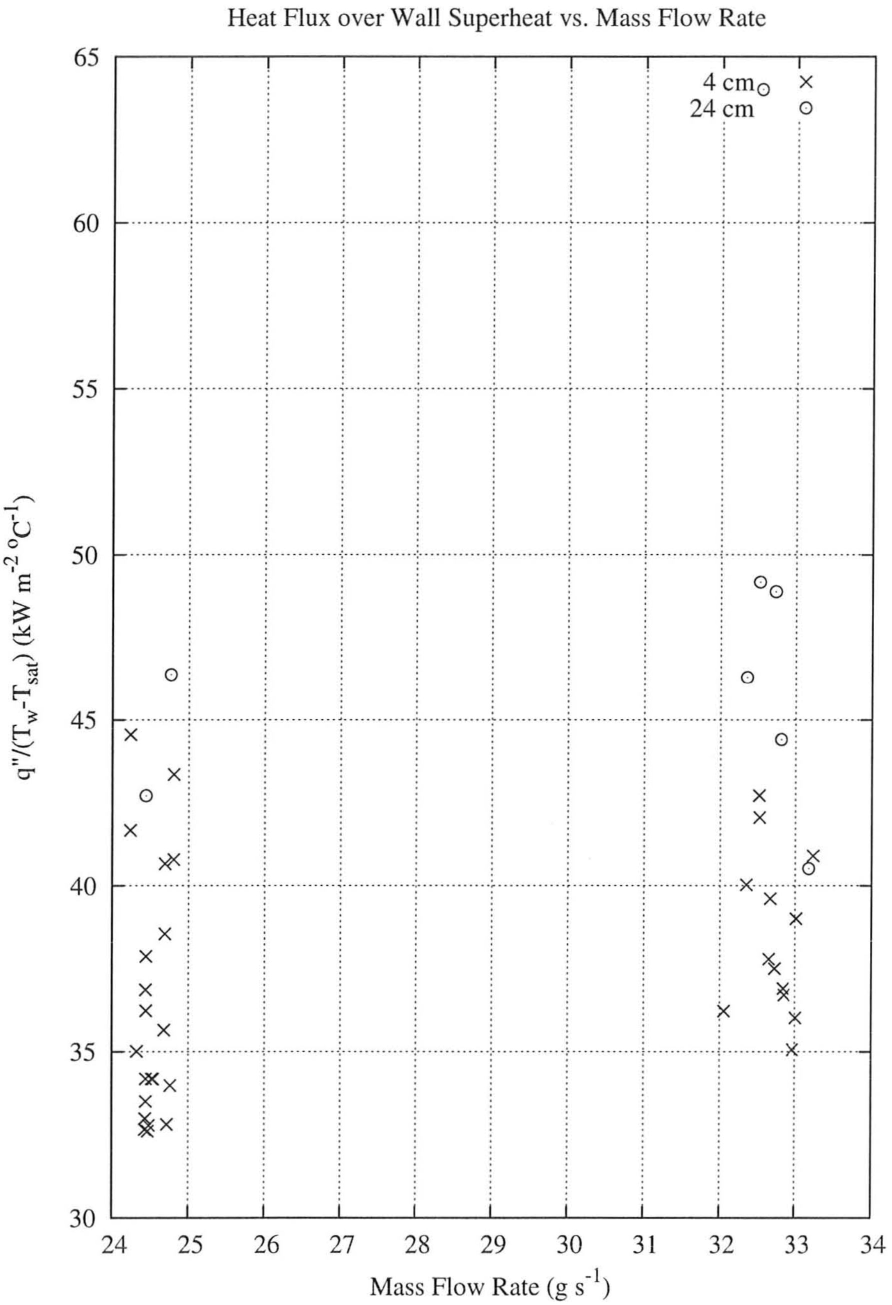

Figure 5.22: Heat flux over wall superheat plotted against mass flow rate (g/s)

Figure 5.22 shows that the dependence of heat flux over wall superheat on mass flux is negligible for the data presented here. This is more consistent with the subcooled boiling correlations from Table 2.2 than with the saturated boiling correlations in Table 2.3 that all contain terms which increase the heat transfer coefficient with respect to mass flux.

Figure 5.23 shows an apparent decreasing trend of heat flux over wall superheat with respect to heated length. Rather than being a 'heated length effect' this may be due to the data for shorter heated lengths being biased toward the slightly subcooled 'Significant Void Flow' region. If this is the case then the same argument made with respect to inlet subcooling may be made here—shorter heated lengths correspond to greater thermodynamic disequilibrium between the thermal boundary layer and the 'body' of the fluid.

Overall the parametric behaviour of the saturated boiling data presented here was similar to the subcooled boiling data. It is likely that nucleate boiling was the dominant mode of heat transfer in both cases since the mass quality of the saturated boiling data was limited to small values of less than 0.07. Although three different flow regimes—bubbly, slug, and annular—were predicted for the saturated boiling data they did not have a noticeable effect on heat transfer for these experiments. More saturated boiling data is needed to further evaluate the performance of this experiment.

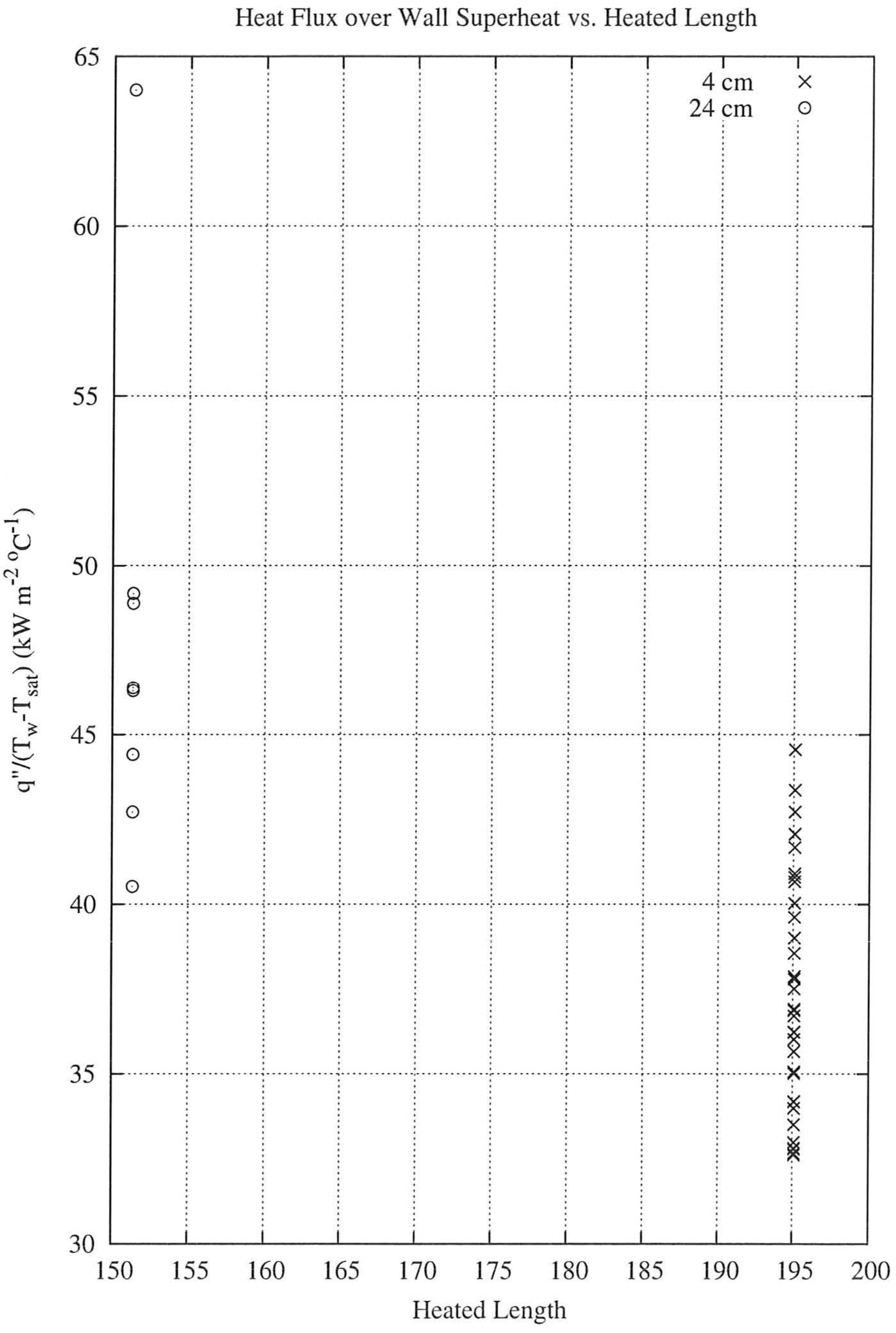

Figure 5.23: Heat flux over wall superheat plotted against heated length (1 diameter = 4.6 mm)

Chapter 6

Conclusion

A thermalhydraulics experiment has been constructed at McMaster University that was designed to gather heat transfer and critical heat flux data at pressures up to 10 MPa and test section powers up to 96 kW. Pump capacity is estimated to be up to 870 kPa(d) but is likely less due to wear and aging. Test section inlet temperature is limited by the available power of the preheater which is estimated to be 12 kW. The operating pressure for boiling heat transfer is limited by the heat removal capability of the condenser because the saturation temperature of water increases with pressure. The condenser is currently cooled by the municipal supply.

Quantity	**Parametric Range**
Mass Flux	1500, 2000 $\frac{kg}{m^2 s}$
Re	36–69$\times 10^5$
Pressure	2000 kPa
Inlet Temperature	126, 148, 170, 180 ^{o}C
Thermodynamic Quality	-0.20–0.07
Heat Flux	99–1074 $\frac{kW}{m^2}$
Heated Length	0.932 m
Diameter	0.0046 m

Table 6.1: Range of experimental conditions for the data presented in this thesis

Commissioning data have been presented in this thesis. Heat transfer data were gathered for a 4.6 mm inside diameter by 93.2 cm long test section with an outlet pressure of 2000 kPa, inlet temperatures of 126, 148, 170, and 180°C, mass fluxes of 1500 and 2000 $^{kg}/_{m^2s}$, and local qualities of -0.20 to 0.07. A summary of the parameter values examined for the commissioning data presented in this thesis is presented in Table 6.1.

Single phase heat transfer data with good heat balance results were slightly underpredicted by the Petukhov-Popov correlation and slightly overpredicted by the Gnielinski correlation for the most reliable thermocouple located 4 cm from the test section outlet. Subcooled boiling data were well-correlated by the Jens-Lottes, Thom *et al*, Rassokhin *et al*, and Labuntsov correlations with a typical mean error of -5.0% and standard deviation of 15% for all measurement positions considered together. Subcooled boiling data were poorly predicted by the correlation of Yin *et al* that was based on data with very high heat fluxes and subcooling. Saturated boiling data for the thermocouple located 4 cm from the test section outlet were overpredicted by 15.3% with a standard deviation of 18.0% by the modified Chen correlation. The Steiner-Taborek correlation performed relatively poorly and overpredicted the same data by 29.3% with a standard deviation of 23.7%. Saturated boiling data was limited to the nucleate boiling range with thermodynamic equilibrium mass qualities less than 0.07.

Future experiments with different boundary conditions are needed to fully demonstrate this facility's capabilities. For the limited range of parameters that were investigated, the commissioning data gathered so far show good agreement with existing correlations. Therefore it is expected that future results will be equally satisfactory.

6.1 Experiment Improvements

After analyzing the commissioning tests presented in this thesis several areas for improvement have been identified. These are listed in the following paragraphs.

There was a significant amount of data that had large heat balance errors. In particular the single phase data with high wall to bulk fluid temperature differences were predominated by data with negative heat balance errors. This meant that the measured power to fluid was higher than the measured test section electrical power. The source of heat balance errors must be found and corrected.

Wall temperature measurements using thermocouples could not be made by the Keithley data acquisition system directly. The interference from the high current flowing through the test section prevented the Keithley unit from making reliable measurements. Routing the thermocouple wire in twisted pairs and using an accurate external ice point will reduce the interference. Using the Keithley 3700 to measure wall temperature directly will reduce the uncertainty in wall temperature measurements.

Making small adjustments to flow rate using a single needle valve was difficult because the flow rate was very sensitive to small changes in valve position. Flow rate control was made more difficult once net vapour generation occurred in the test section because of increases in the pressure gradient. A better-designed mechanical flow control system would allow more precise flow control. In the future a variac will be used to control power to the pump motor which should improve flow control even further.

The experiment will be used in the future to gather heat transfer data during transients. The data acquisition currently being used takes approximately 20 seconds to make one cycle through all of the process measurements. The power and flow transients that will be examined occur on the order of 1–5 seconds. A much faster data acquisition system must be installed in order to make these measurements. The current system is sufficient for monitoring process variables and measuring steady-state data.

6.2 Direction of Future Research

Further experimental work will be possible once the improvements stated above have been made to the facility. The next stage in its development will be to gather commissioning data for critical heat flux and measure heat transfer data for a wider range of operating conditions. In particular it will be important to obtain some results for saturated boiling with higher local mass qualities to better validate its results against existing saturated boiling correlations.

Ultimately the experiment will be used to investigate the relationship between the onset of CHF during steady-state and transient conditions. Using this facility it will be possible to determine if it is sufficient to estimate CHF during transients using local conditions and steady-state CHF prediction methods. This will be accomplished by systematically performing experiments with a wide variety of boundary conditions. These experimental results will then be used to generate a transient CHF prediction method.

Contributions to Knowledge

The author has made the following contributions to knowledge during their Master's studies:

Statham, B.A. (2009). Using a thermalhydraulics system code to estimate heat transfer coefficients for a critical heat flux experiment. Canadian Nuclear Society/Canadian Nuclear Association National Student Conference. (Unrefereed conference paper and oral presentation)

Statham, B.A. (2008). Novel design of a CHF experimental facility. Canadian Nuclear Society/Canadian Nuclear Association National Student Conference. (Unrefereed conference paper and oral presentation)

Appendix A

Calibration Data

A.1 Pressure Transmitters

The following subsections show the Stern Laboratories calibration data for the pump inlet pressure and test section differential pressure transducers. The transmitters were ranged and zeroed then the transmitters' 4-20 mA output, measured as a voltage across a precision 500 Ω resistor, were fitted to a quadtratic function. The fitting function is in the form $P = A + B \cdot (V_m - V_o) + C \cdot (V_m - V_o)^2$ where V_m is the measured voltage and V_o is the voltage when the instrument is zeroed with a nominal output of 4 mA.

A.1.1 Rosemount 1151DP5

Reference (kPa)	Voltage	Calculated (kPa)	Difference (kPa)
0.000	-0.00005	-0.00121	0.00121
18.000	0.80163	17.97710	0.02290
36.000	1.60330	35.95994	0.04006
54.000	2.40506	53.94903	0.05097
72.000	3.20641	71.93350	0.06650
90.000	4.00811	89.93052	0.06948
108.000	4.80954	107.92577	0.07423
126.000	5.61089	125.92383	0.07617
144.000	6.41308	143.94534	0.05466
162.000	7.21774	161.97770	0.02230
180.000	8.01860	180.02779	-0.02779
162.000	7.21774	162.02701	-0.02701
144.000	6.41685	144.03018	-0.03018
126.000	5.61629	126.04533	-0.04533
108.000	4.81543	108.05812	-0.05812
90.000	4.01413	90.06570	-0.06570
72.000	3.21274	72.07552	-0.07552
54.000	2.41067	54.07499	-0.07499
36.000	1.60802	36.06583	-0.06583
18.000	0.80522	18.05778	-0.05778
0.000	0.00148	0.03311	-0.03311

Fitting function: $22.422979 \cdot (V_m - V_o) + 0.003528 \cdot (V_m - V_o)^2$

RMS error = 0.0539 kPa, 2σ=0.1680%

RMS/Span = 0.0299%

A.1.2 Rosemount 3051CG5

Reference (kPa)	Voltage	Calculated (kPa)	Difference (kPa)
0.000	0.00006	0.09050	-0.09050
1000.000	0.61531	1001.23688	-1.23688
2000.000	1.22972	2001.03068	-1.03068
3000.000	1.84383	3000.34370	-0.34370
4000.000	2.45755	3999.05136	0.94864
5000.000	3.07163	4998.35767	1.64233
6000.000	3.68533	5997.05860	2.94140
7000.000	4.29999	6997.35468	2.64532
8000.000	4.91412	7996.79625	3.20375
9000.000	5.52917	8997.75002	2.24998
10000.000	6.14407	9998.47212	1.52788
11000.000	6.75938	10999.87604	0.12396
12000.000	7.37376	11999.80258	0.19742
13000.000	7.98840	13000.16179	-0.16179
12000.000	7.37511	12002.00334	-2.00334
10000.000	6.14655	10002.49979	-2.49979
8000.000	4.91698	8001.44660	-1.44660
6000.000	3.68923	6003.41108	-3.41108
4000.000	2.46043	4003.74290	-3.74290
2000.000	1.23225	2005.14083	-5.14083
0.000	0.00097	1.58505	-1.58505

Fitting function: $1627.194892 \cdot (V_m - V_o) + 0.023081 \cdot (V_m - V_o)^2$

RMS error = 2.2535 kPa, 2σ=0.1414%

RMS/Span = 0.0173%

Appendix B

Experimental Data

B.1 Thermocouple linearity

B.1.1 Poor Linearity

Figure B.2 shows poor linearity for the thermocouple located 9 cm from the test section outlet. Observation of Figures B.1 and B.2 led to the measurements taken at 9 and 14 cm to be disregarded early on in the experiments.

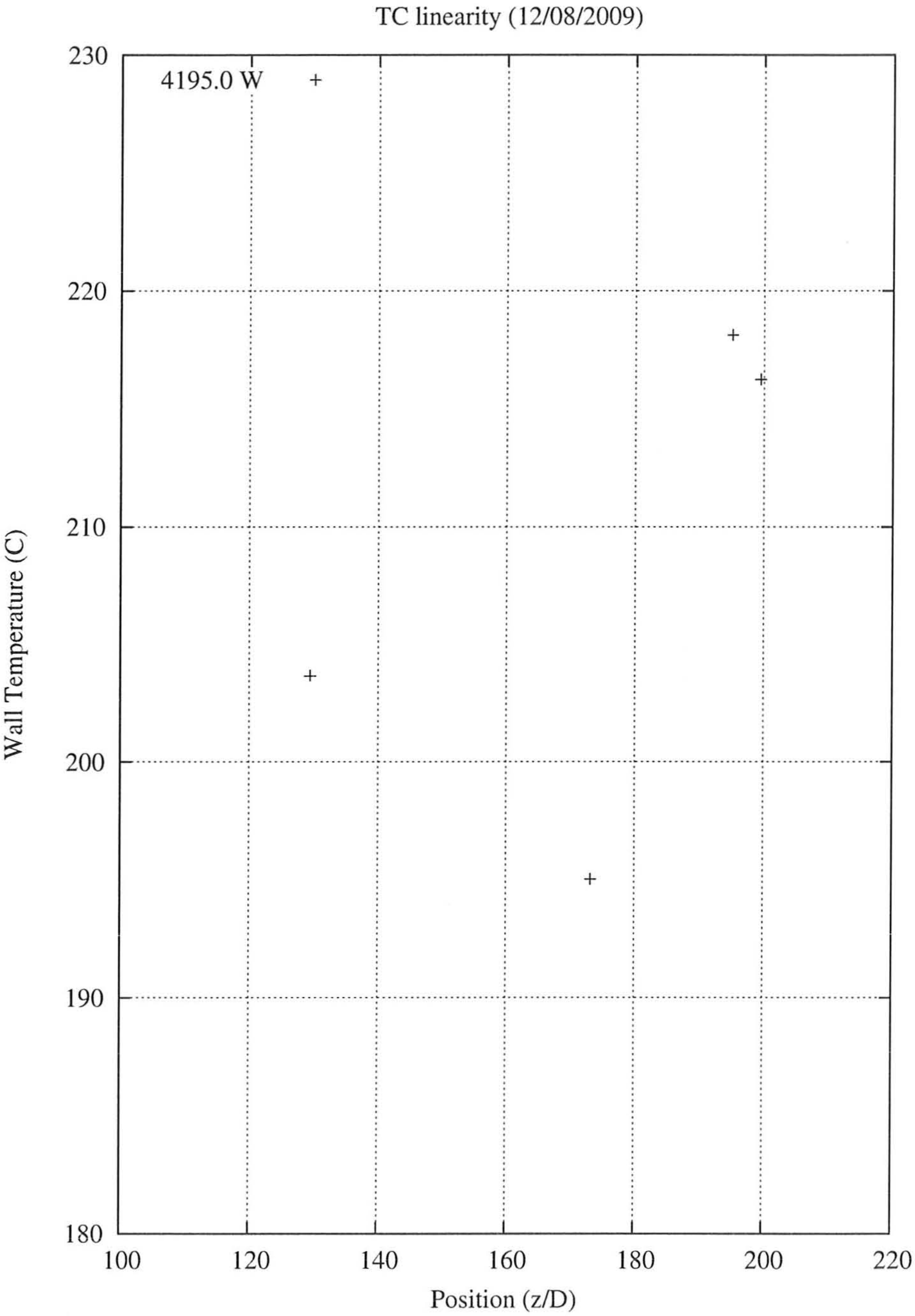

Figure B.1: Thermocouple linearity for thermocouples 2, 4, 14, and 34 cm from the test section outlet

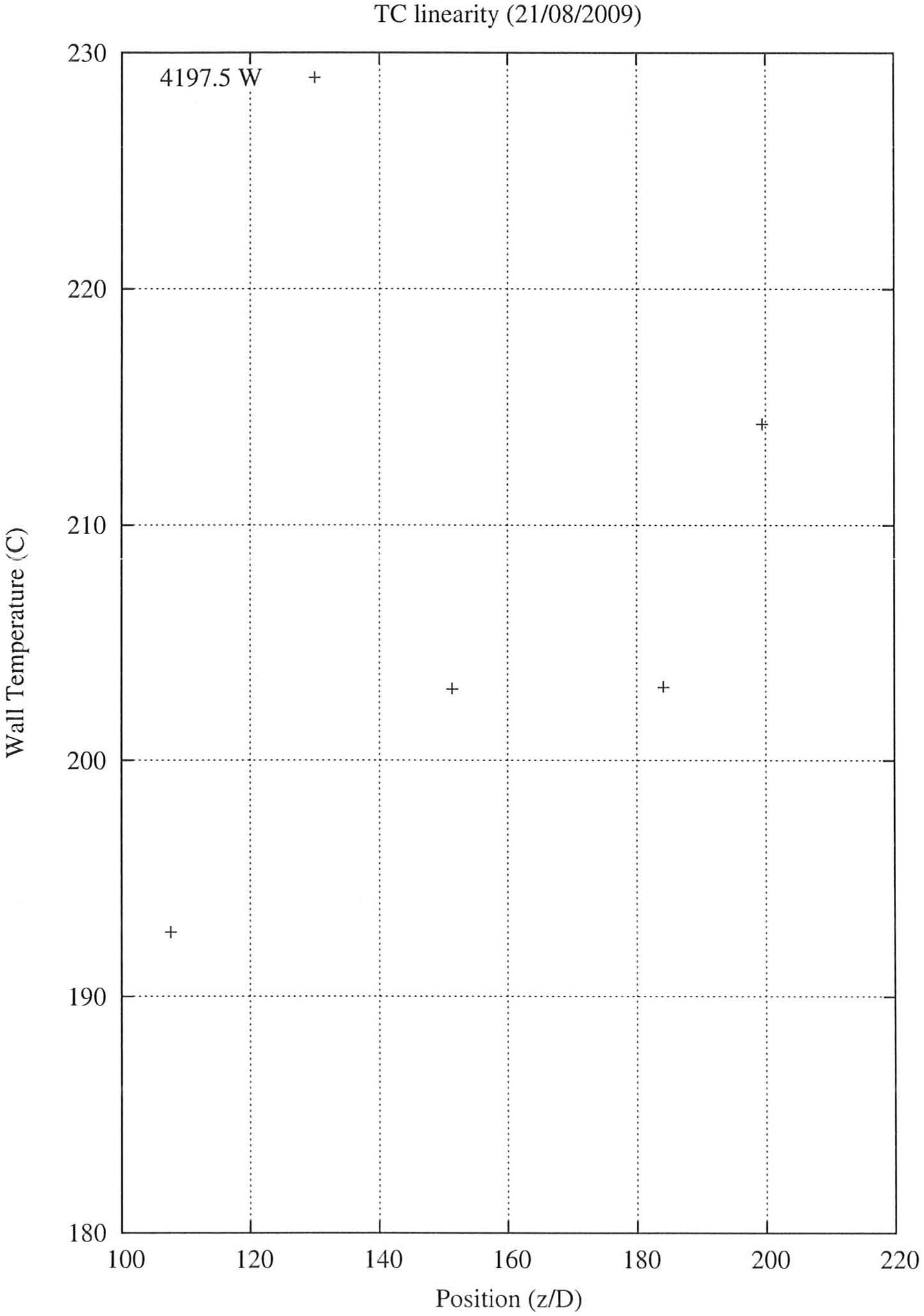

Figure B.2: Thermocouple linearity at 2, 9, 24, and 44 cm from the test section outlet for an experiment T_{in}=170^{o}C and a mass flux of 2000 kg m^{-2} s^{-1}

B.2 Heated Length Effect

This subsection shows all of the experimental boiling curves including those with poor thermocouple linearity. The results with poor linearity are included for the sake of completeness; only the data collected 4, 24, and 44 cm from the test section outlet should be considered when evaluating parametric effects on heat transfer, such as the effect of heated length.

The figures are shown in the order the experiments were conducted with the exception of those that have been included in the appendix and body text above.

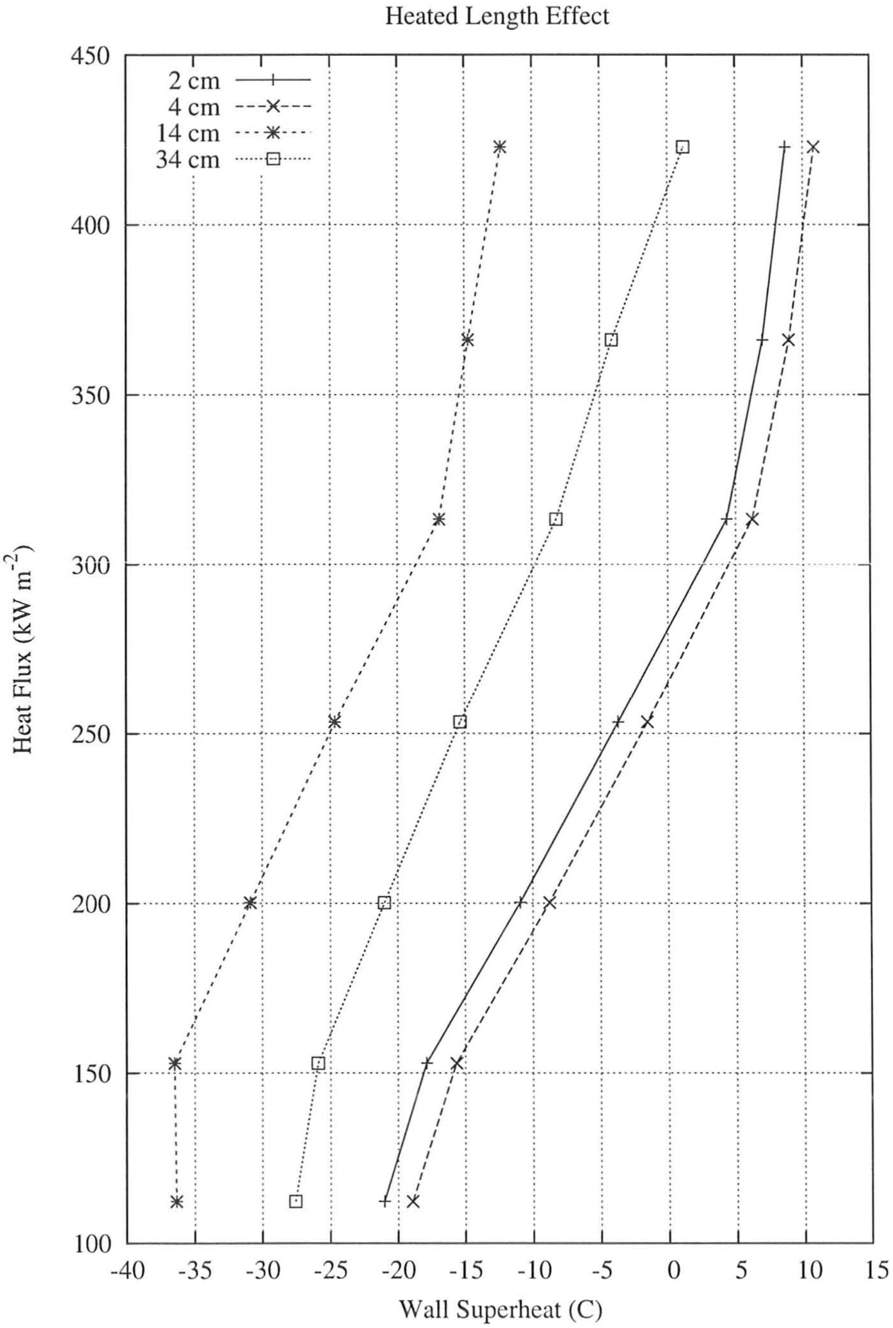

Figure B.3: Boiling curves for four test section positions with T_{in}=180^{o}C and mass flux of 2000 kg m^{-2} s^{-1}

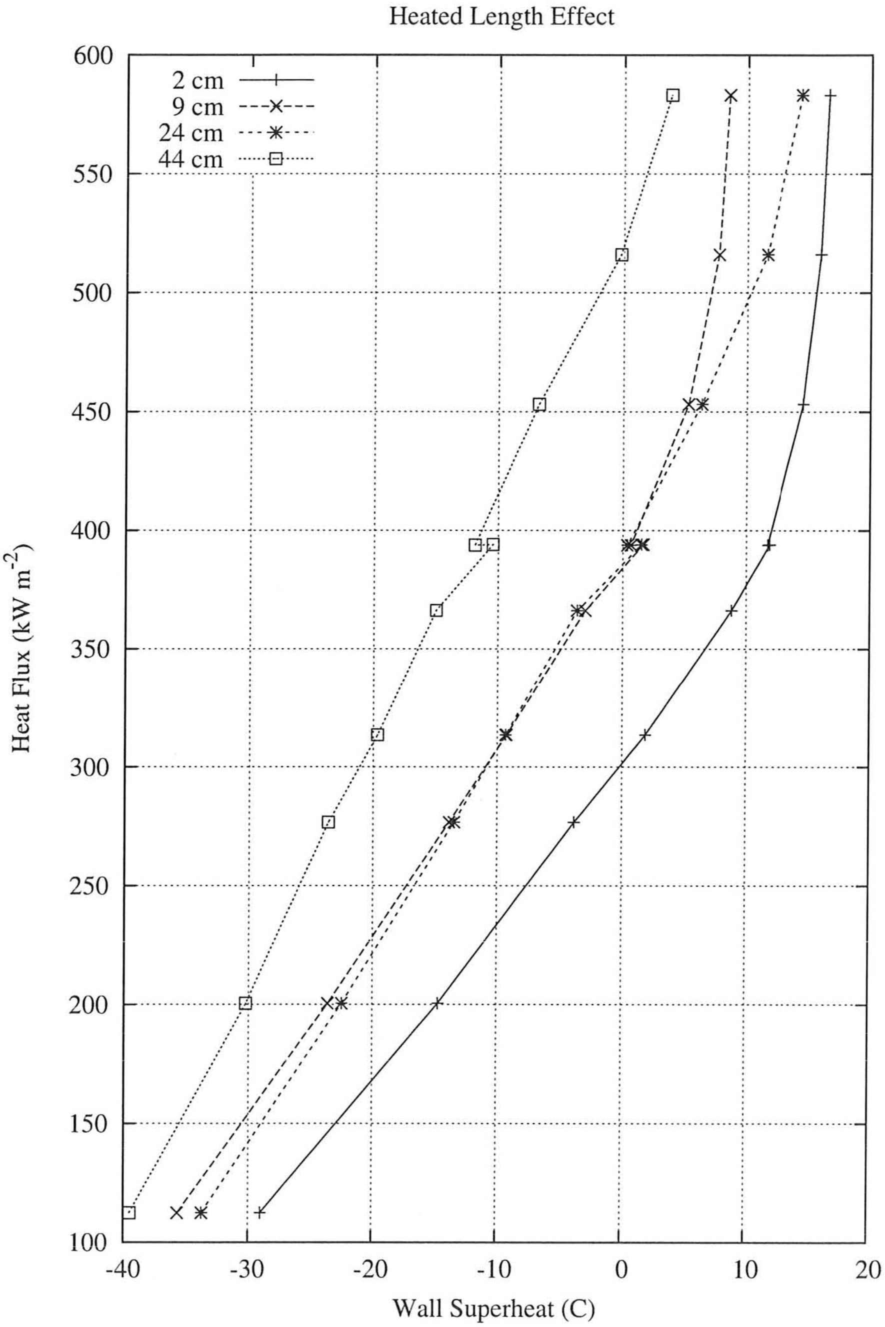

Figure B.4: Boiling curves for four test section positions with T_{in}=170^{o}C and mass flux of 2000 kg m^{-2} s^{-1}

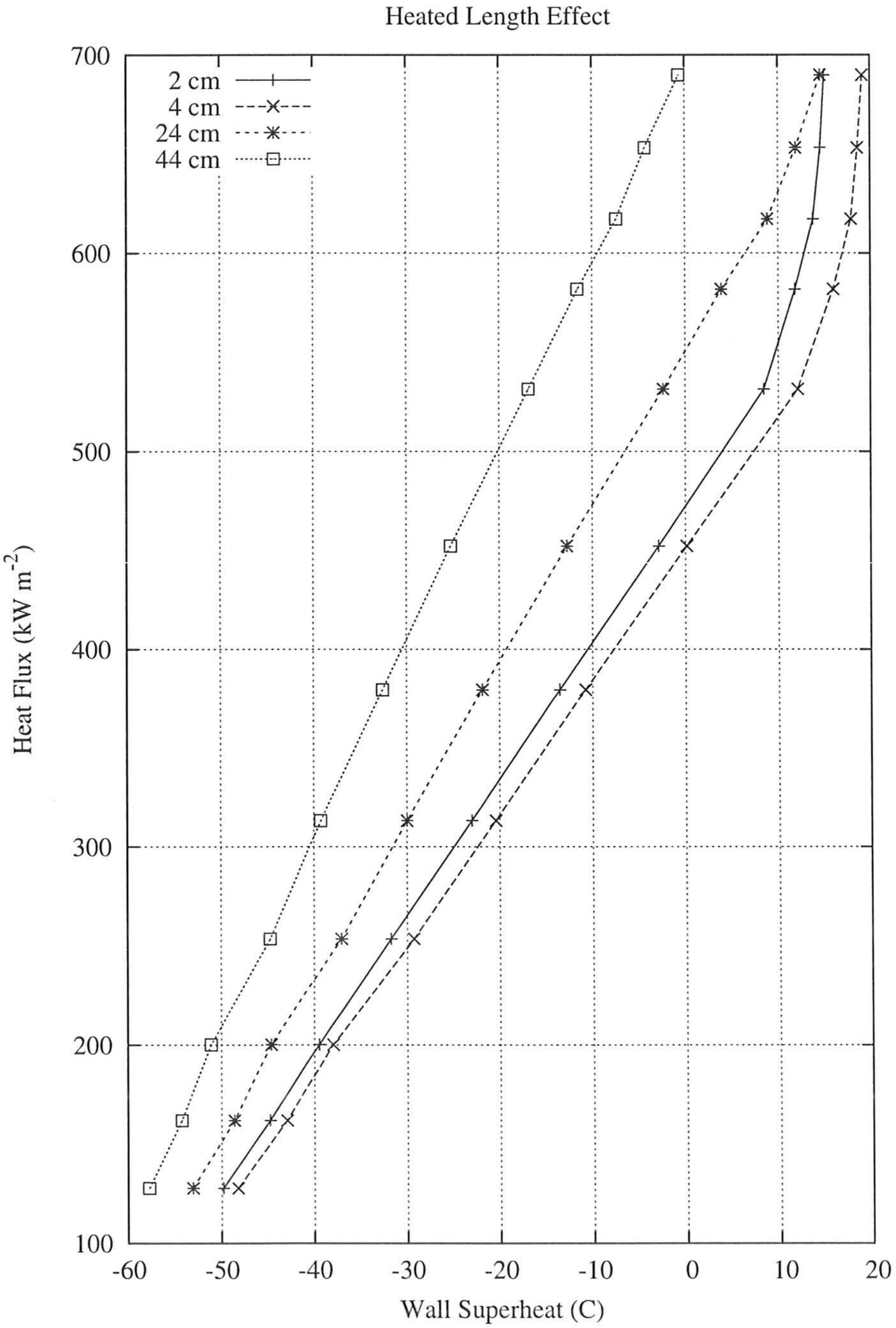

Figure B.5: Boiling curves for four test section positions with T_{in}=148°C and mass flux of 2000 kg m^{-2} s^{-1}

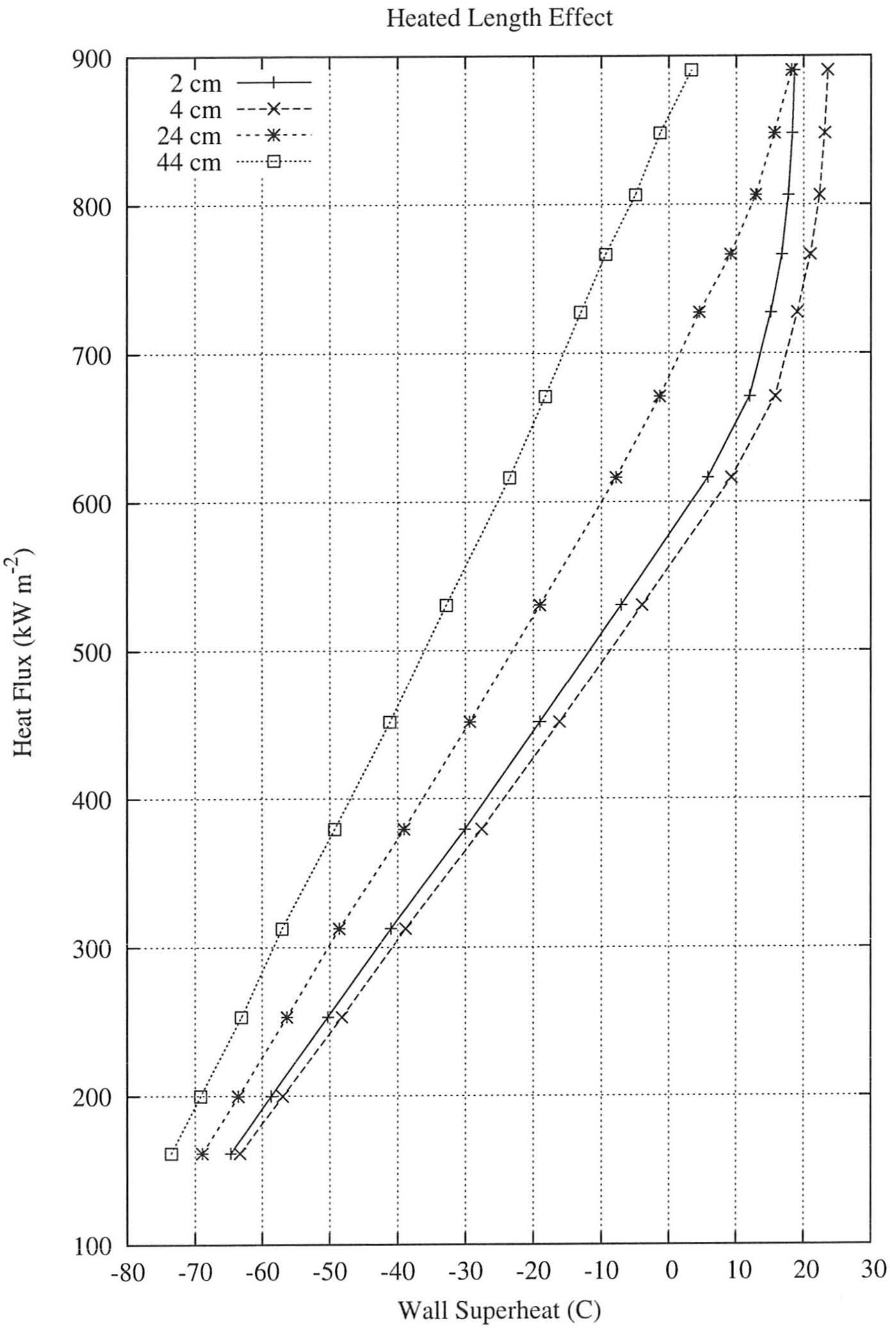

Figure B.6: Boiling curves for four test section positions with T_{in}=126^{o}C and mass flux of 2000 kg m^{-2} s^{-1}

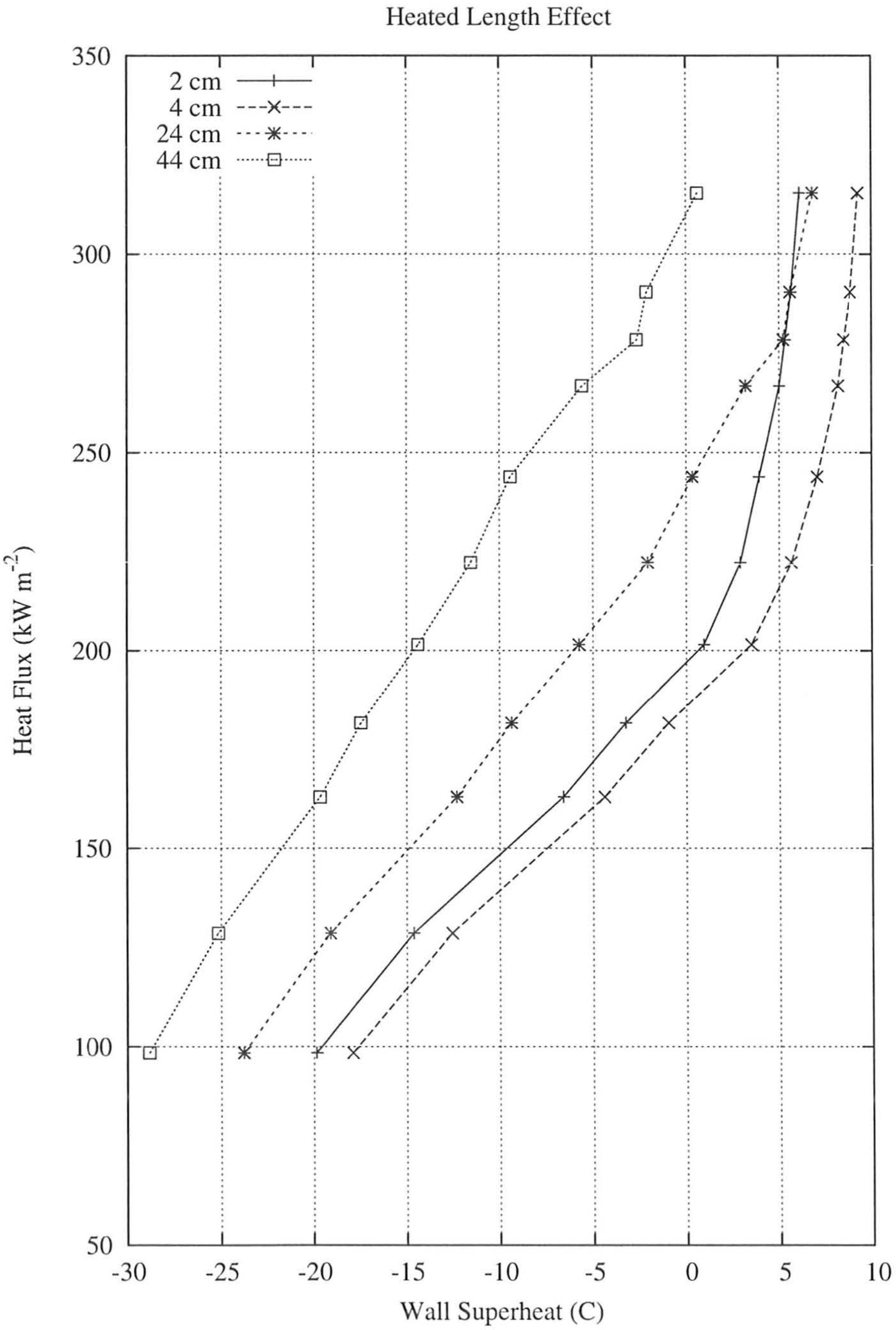

Figure B.7: Boiling curves for four test section positions with T_{in}=180^{o}C and mass flux of 1500 kg m^{-2} s^{-1}

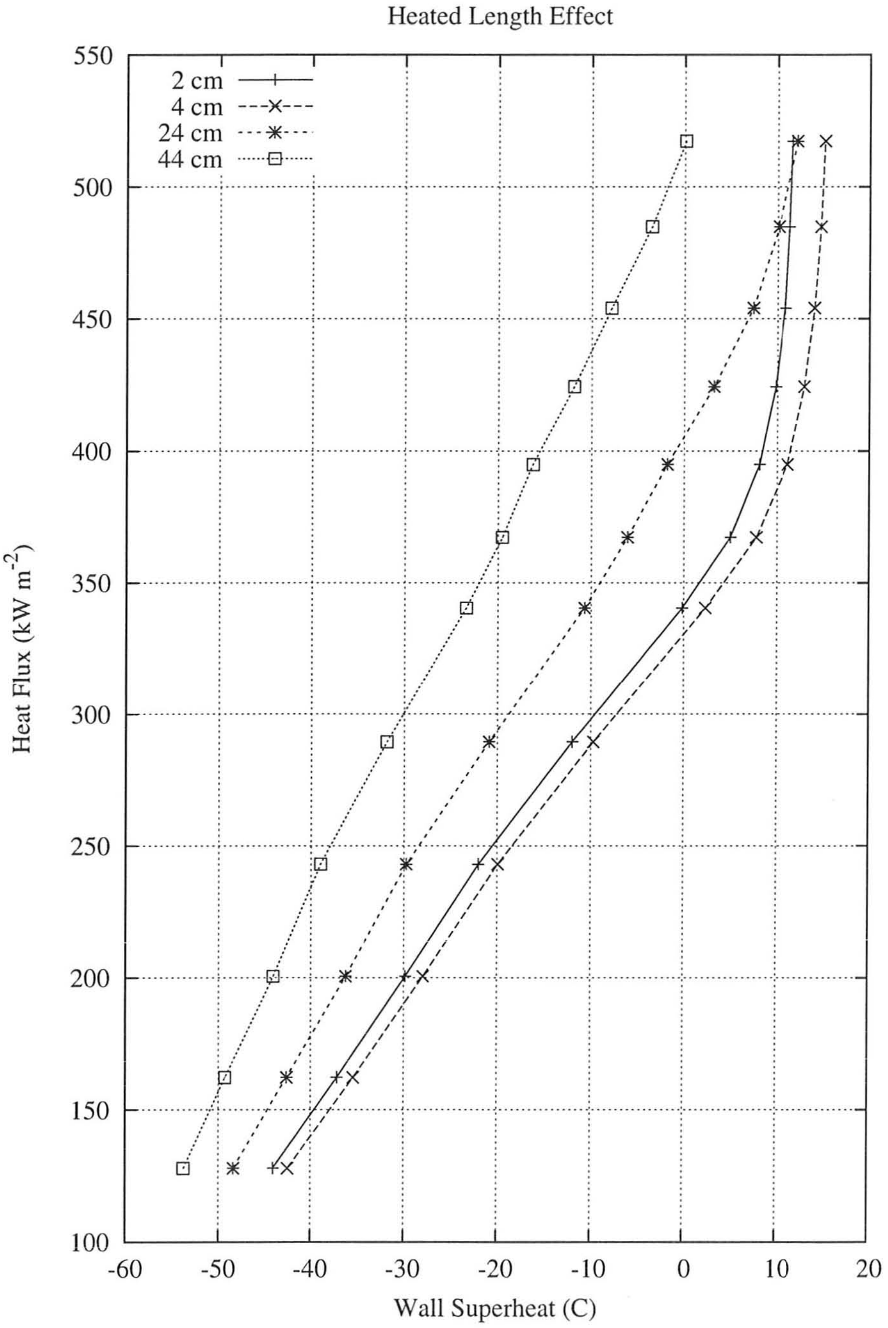

Figure B.8: Boiling curves for four test section positions with T_{in}=148^{o}C and mass flux of 1500 kg m^{-2} s^{-1}

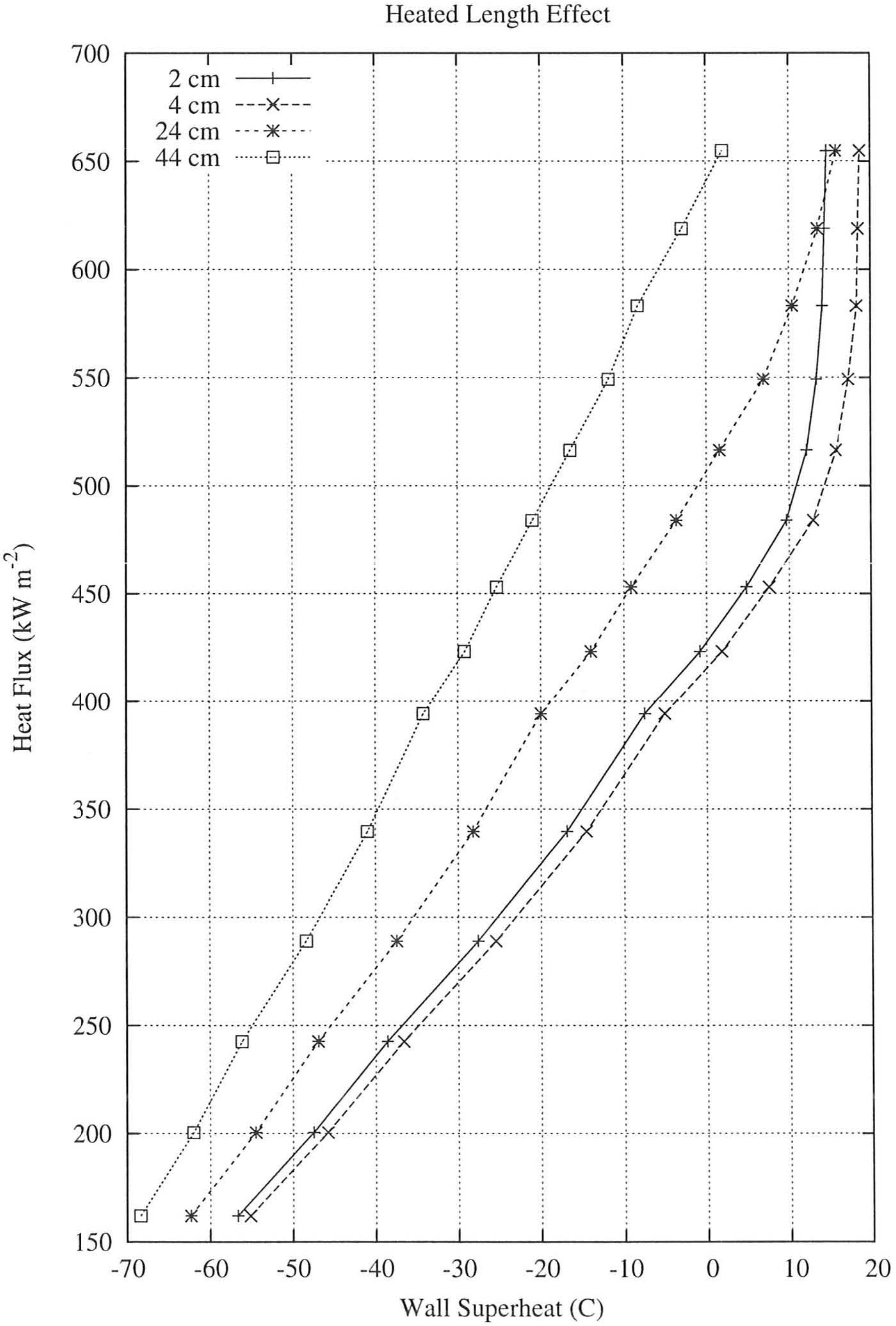

Figure B.9: Boiling curves for four test section positions with T_{in}=126^{o}C and mass flux of 1500 kg m^{-2} s^{-1}

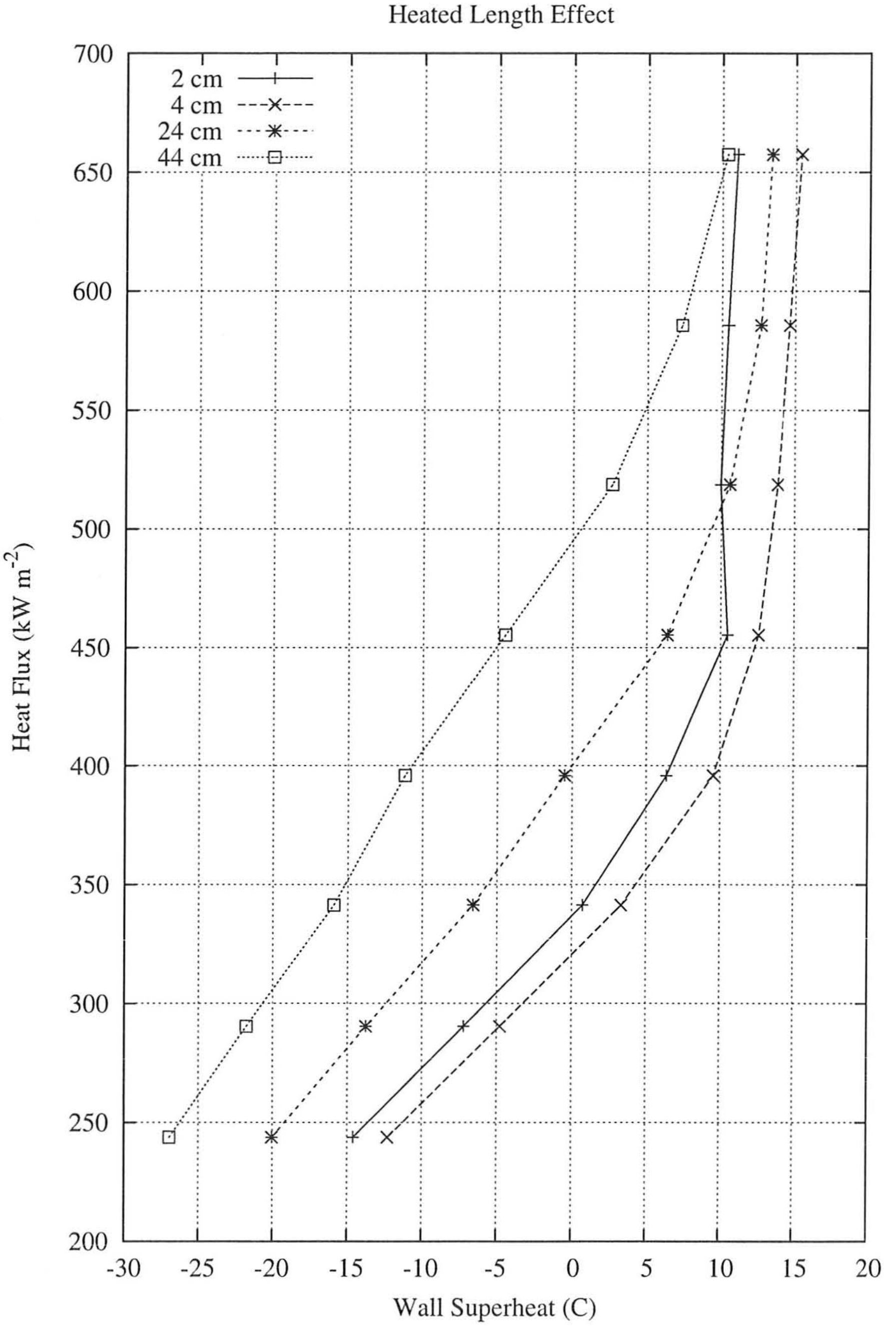

Figure B.10: Boiling curves for four test section positions with T_{in}=170^{o}C and mass flux of 2000 kg m^{-2} s^{-1}

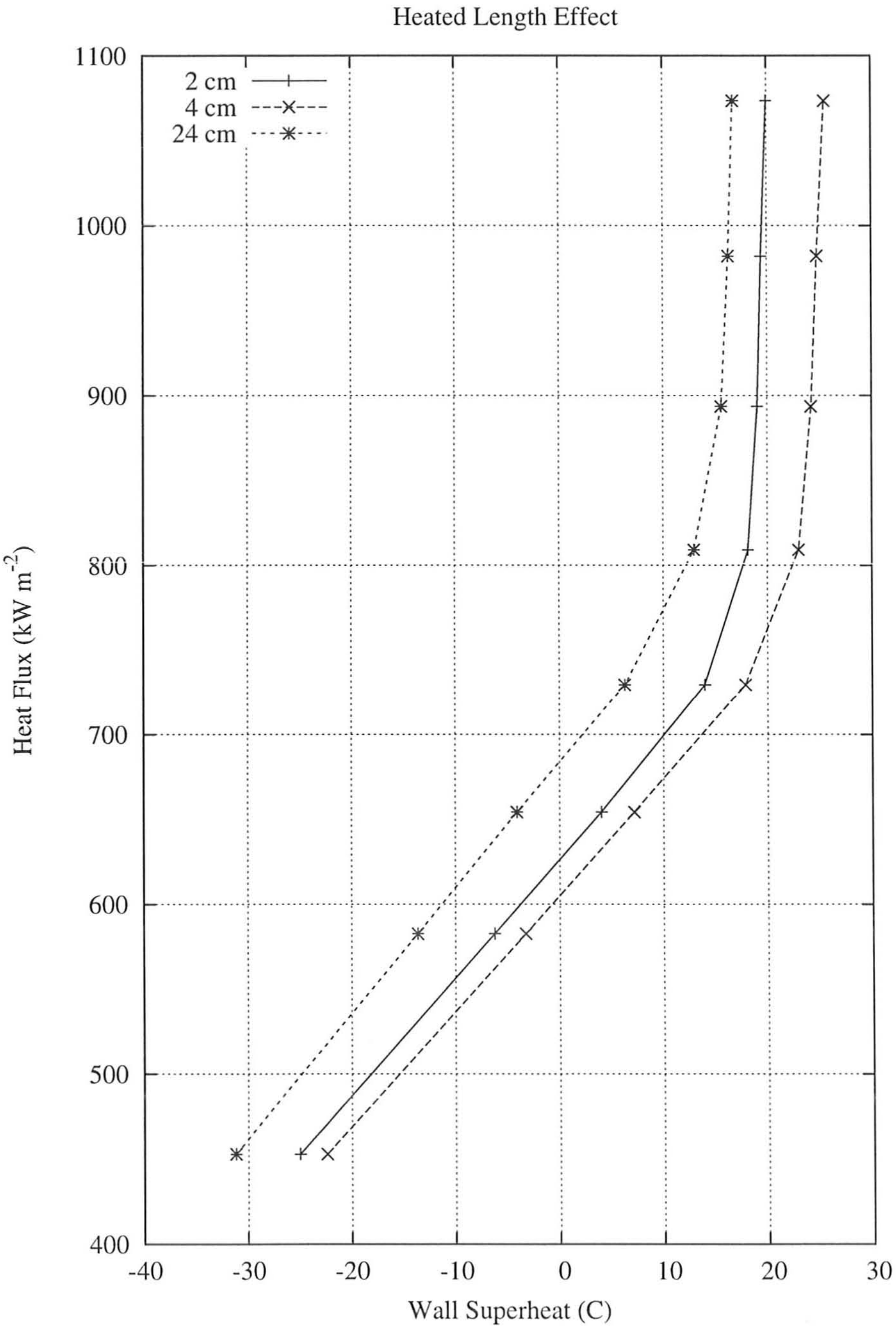

Figure B.11: Boiling curves for four test section positions with T_{in}=126^{o}C and mass flux of 2000 kg m^{-2} s^{-1}

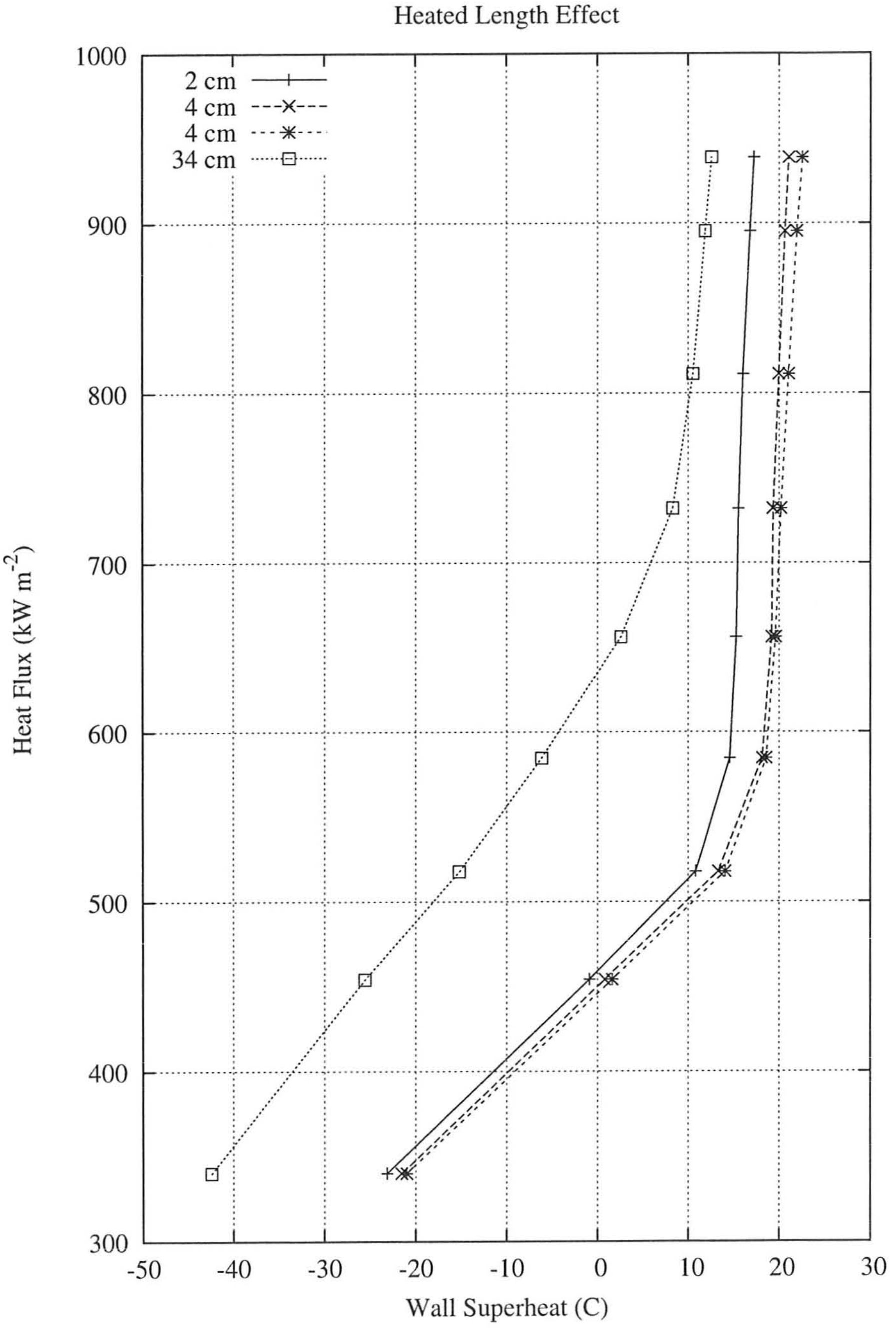

Figure B.12: Boiling curves for four test section positions with T_{in}=126^{o}C and mass flux of 1500 kg m^{-2} s^{-1}

B.3 Constant Inlet Temperature

This section contains data that demonstrates the effect of mass flux on boiling heat transfer while keeping inlet temperature constant.

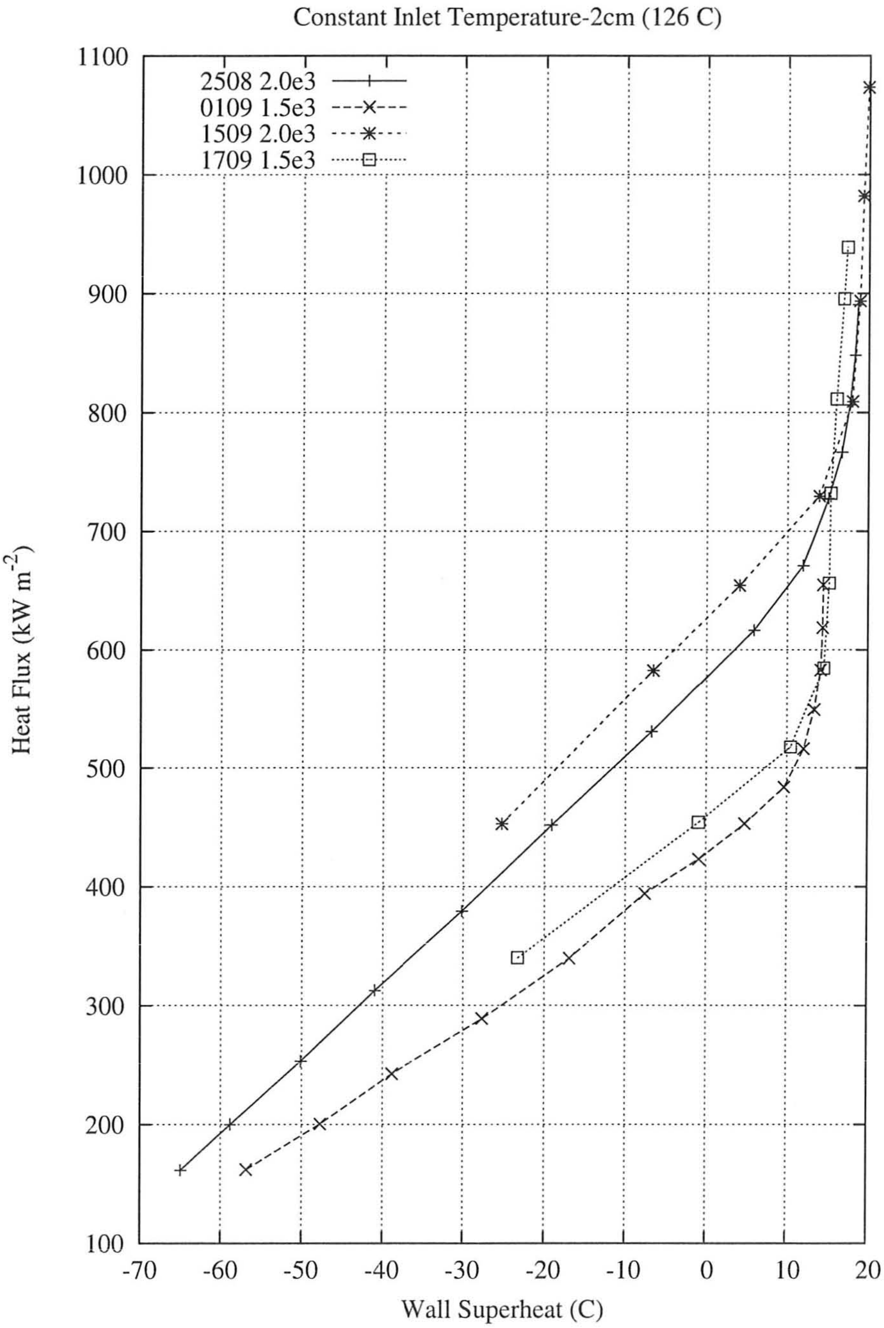

Figure B.13: Boiling curve for constant inlet temperature of 126^{o}C, 2 cm from the TS outlet

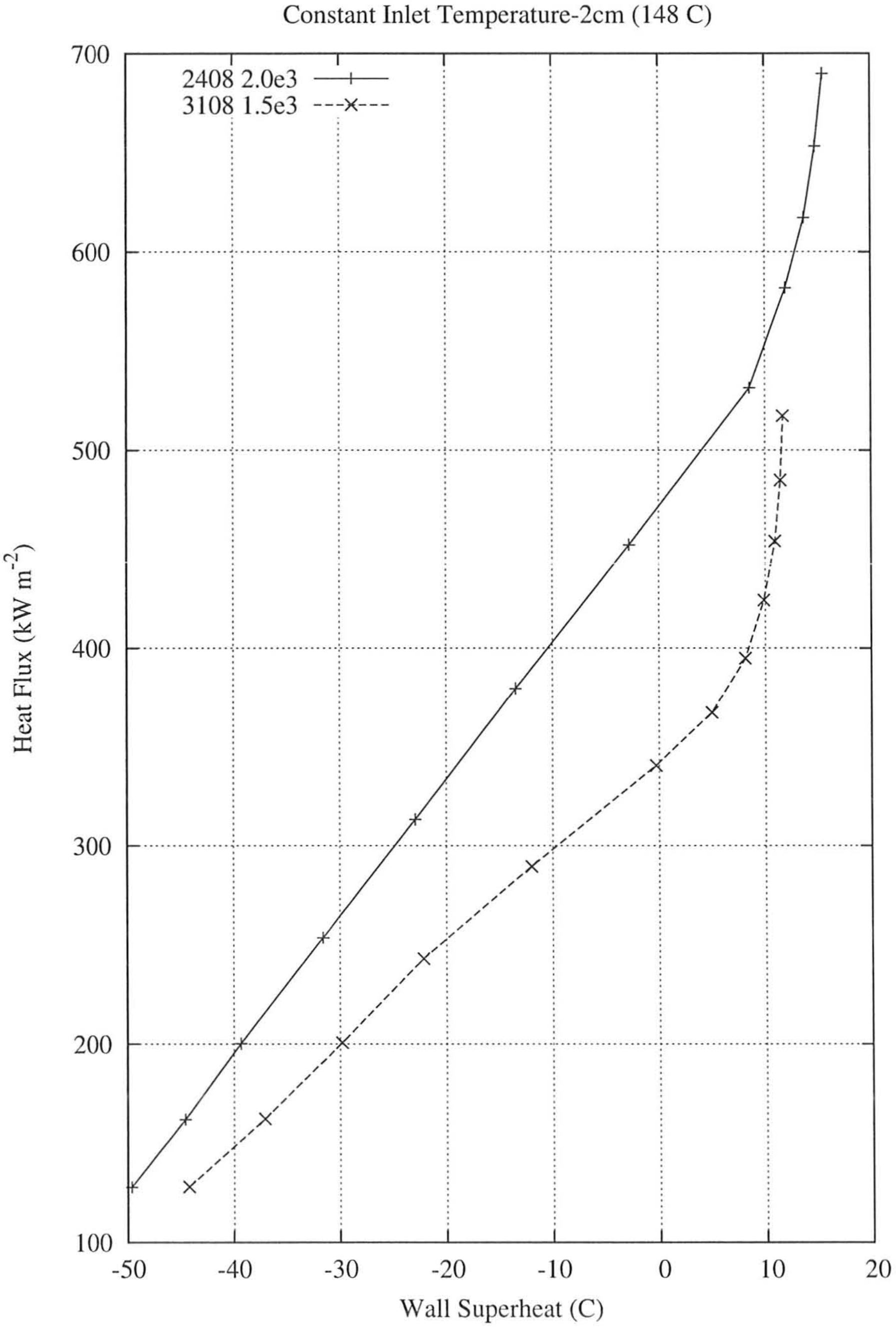

Figure B.14: Boiling curve for constant inlet temperature of 148^{o}C, 2 cm from the TS outlet

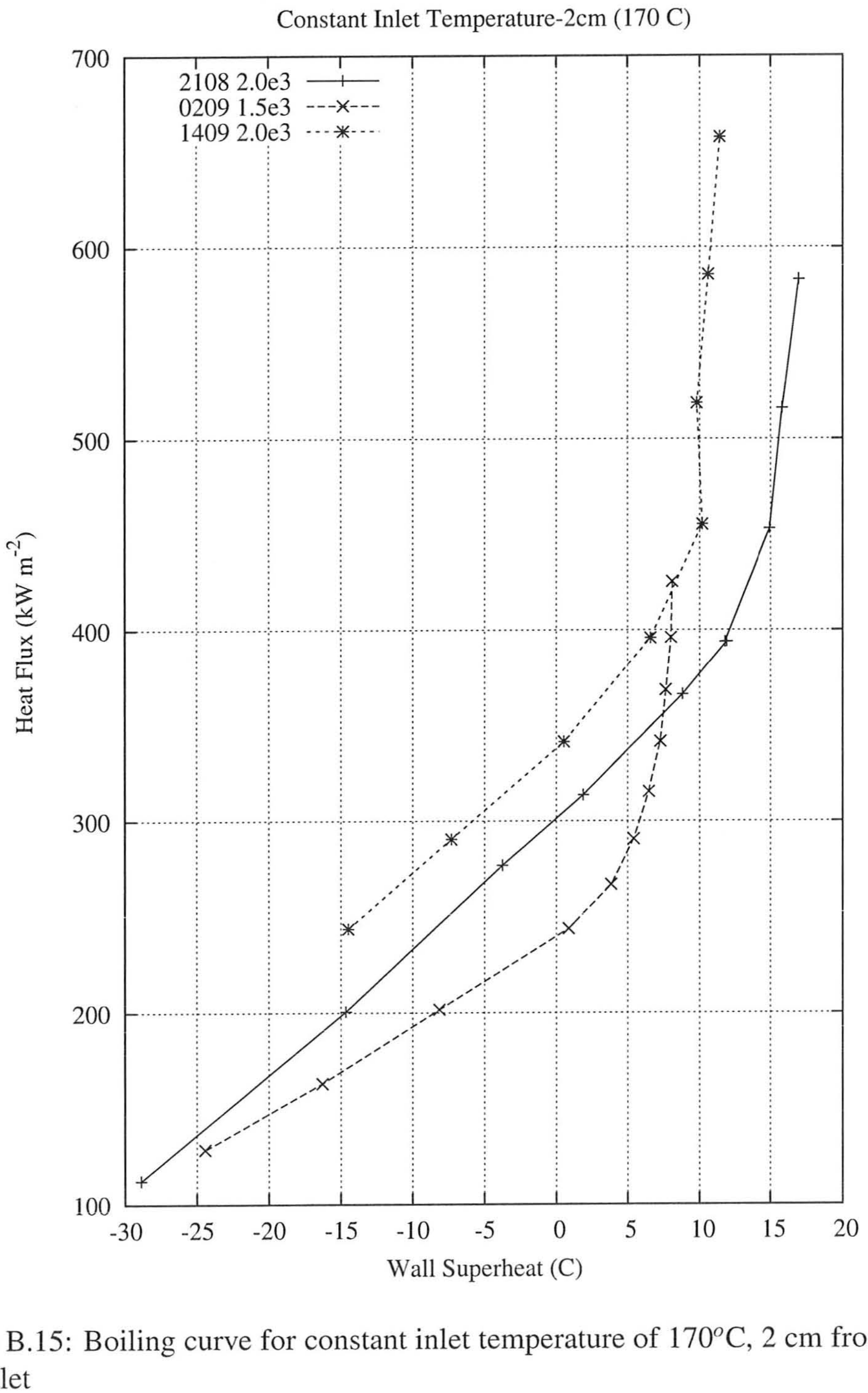

Figure B.15: Boiling curve for constant inlet temperature of 170°C, 2 cm from the TS outlet

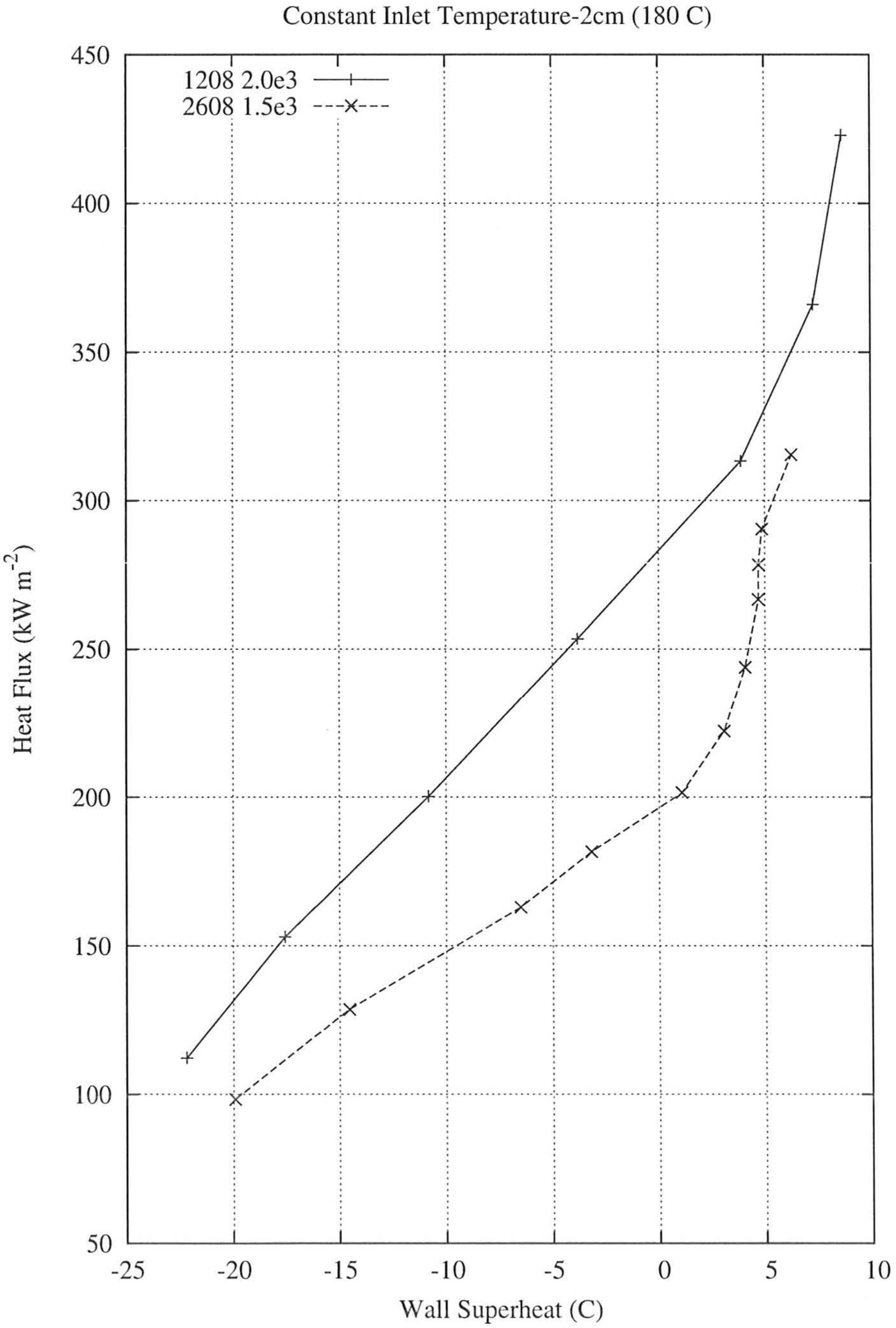

Figure B.16: Boiling curve for constant inlet temperature of 180^{o}C, 2 cm from the TS outlet

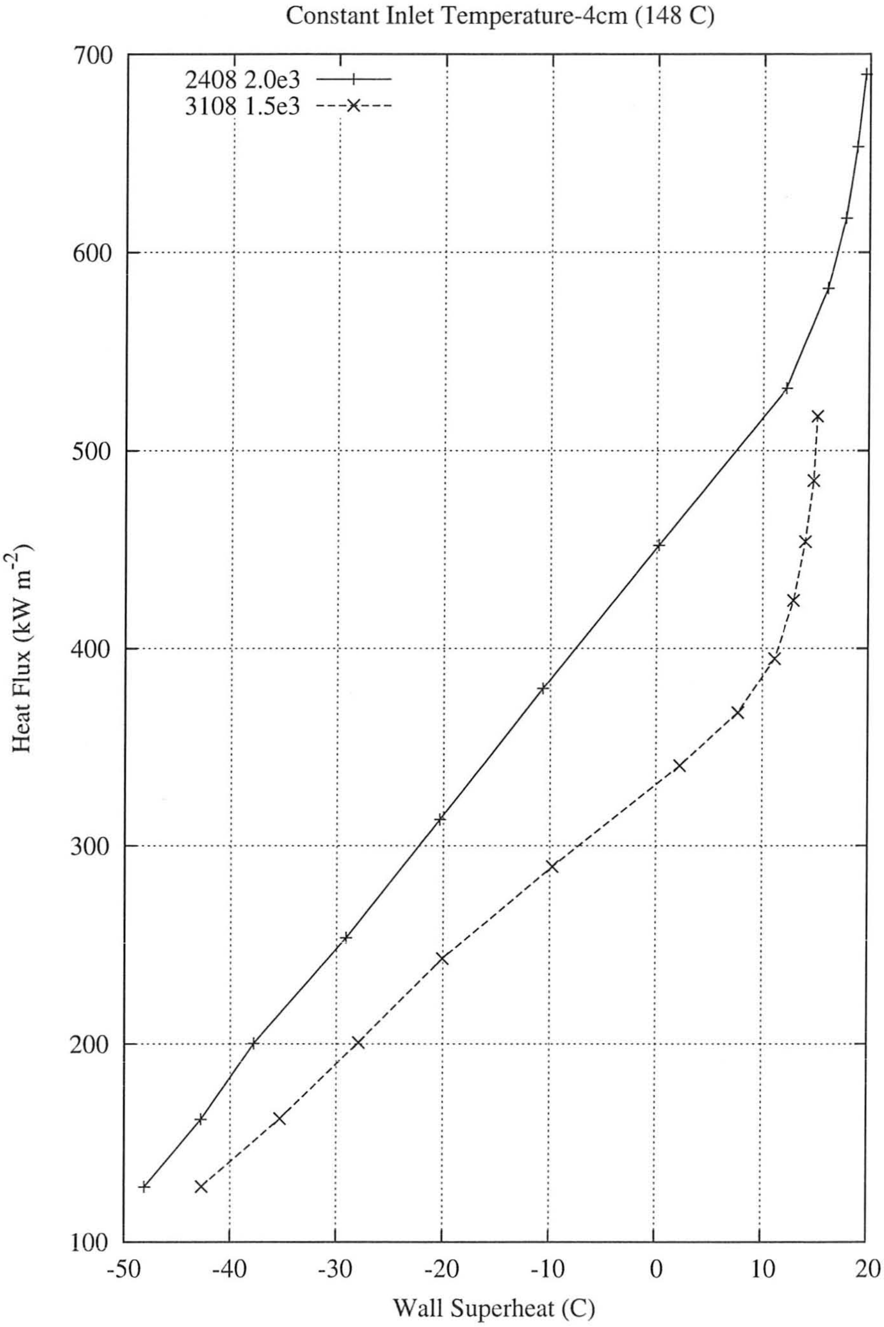

Figure B.17: Boiling curves for constant inlet temperature of 148°C, 4 cm from the TS outlet

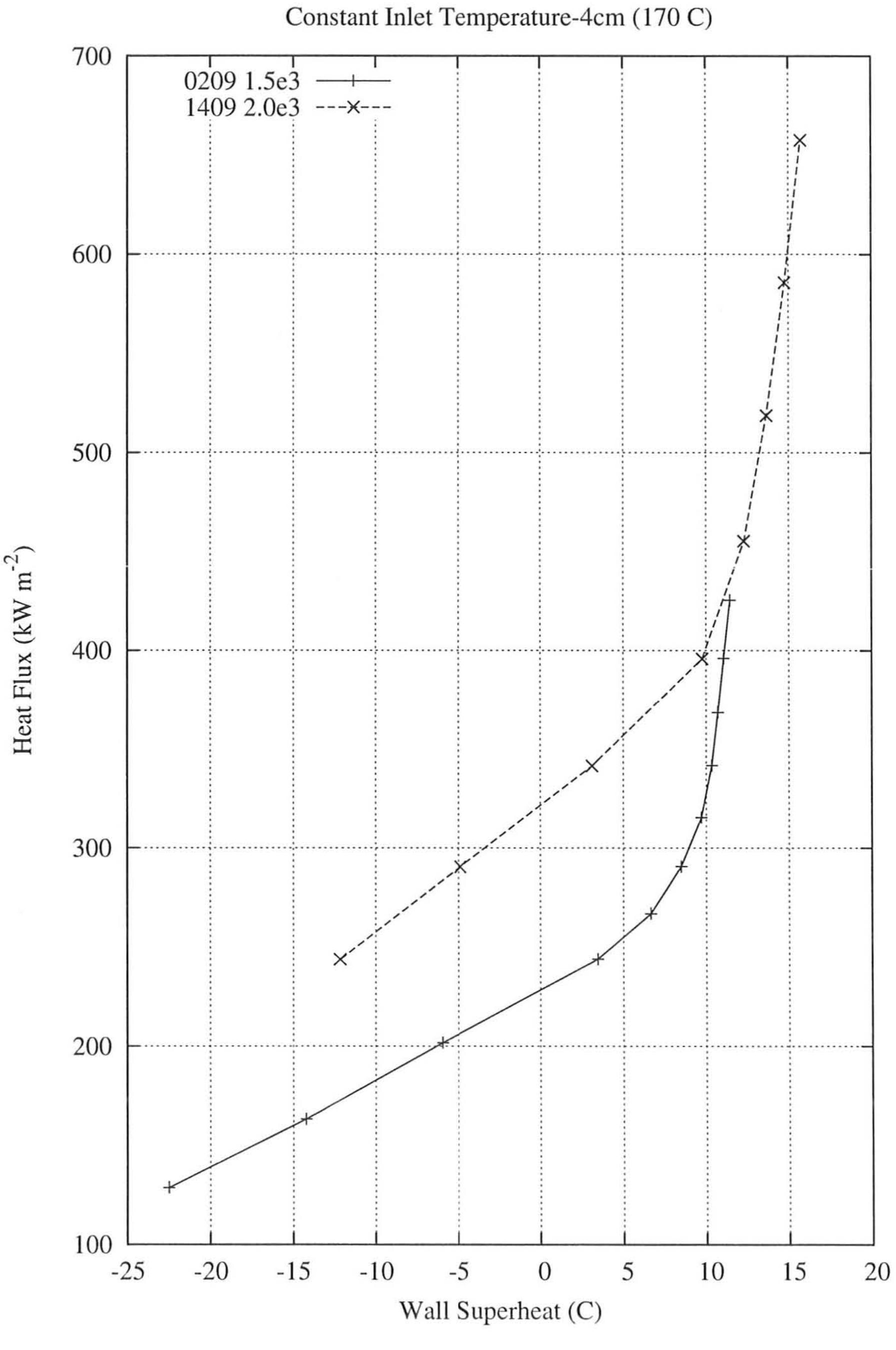

Figure B.18: Boiling curves for constant inlet temperature of 170°C, 4 cm from the TS outlet

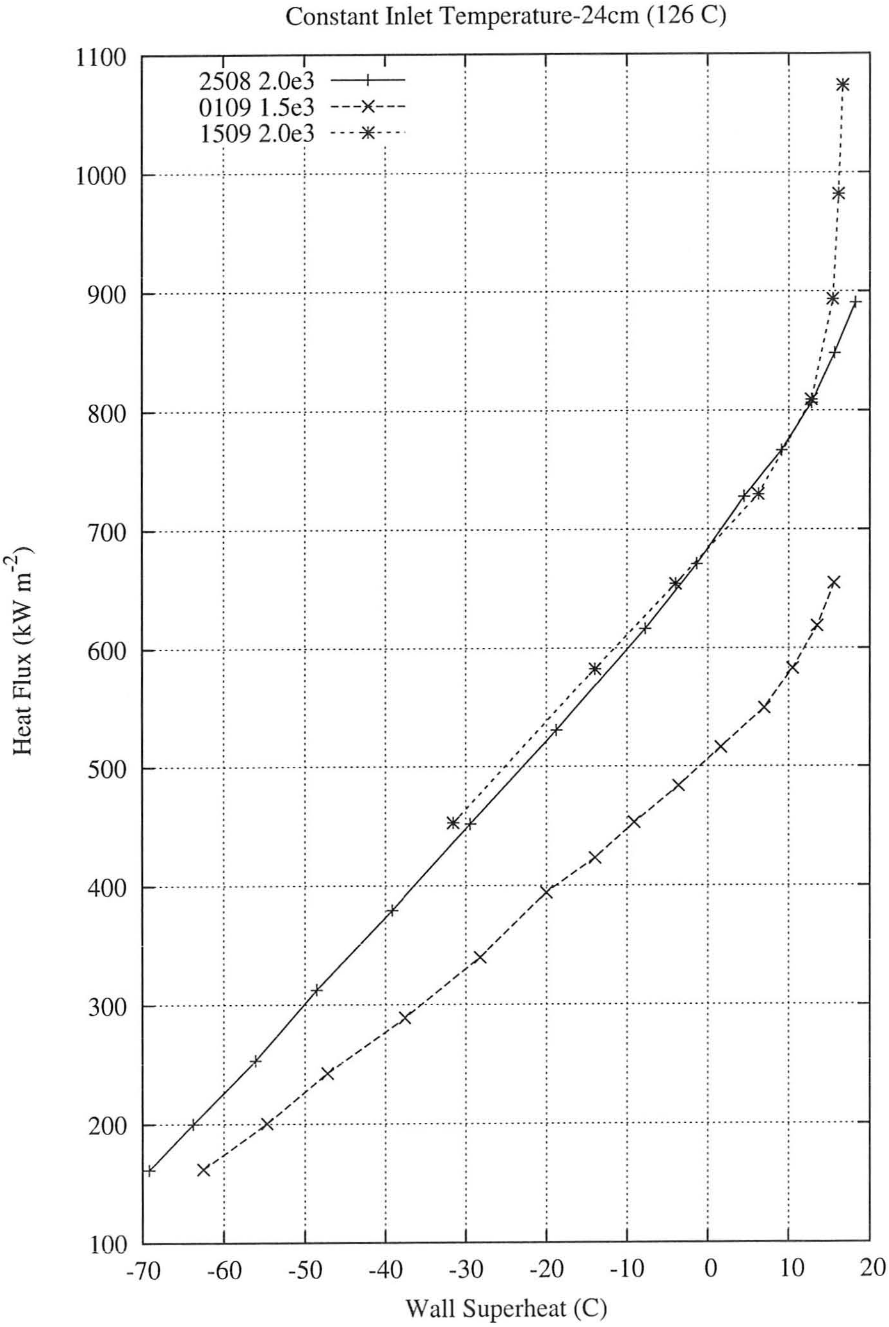

Figure B.19: Boiling curve for constant inlet temperature of 126°C, 24 cm from the TS outlet

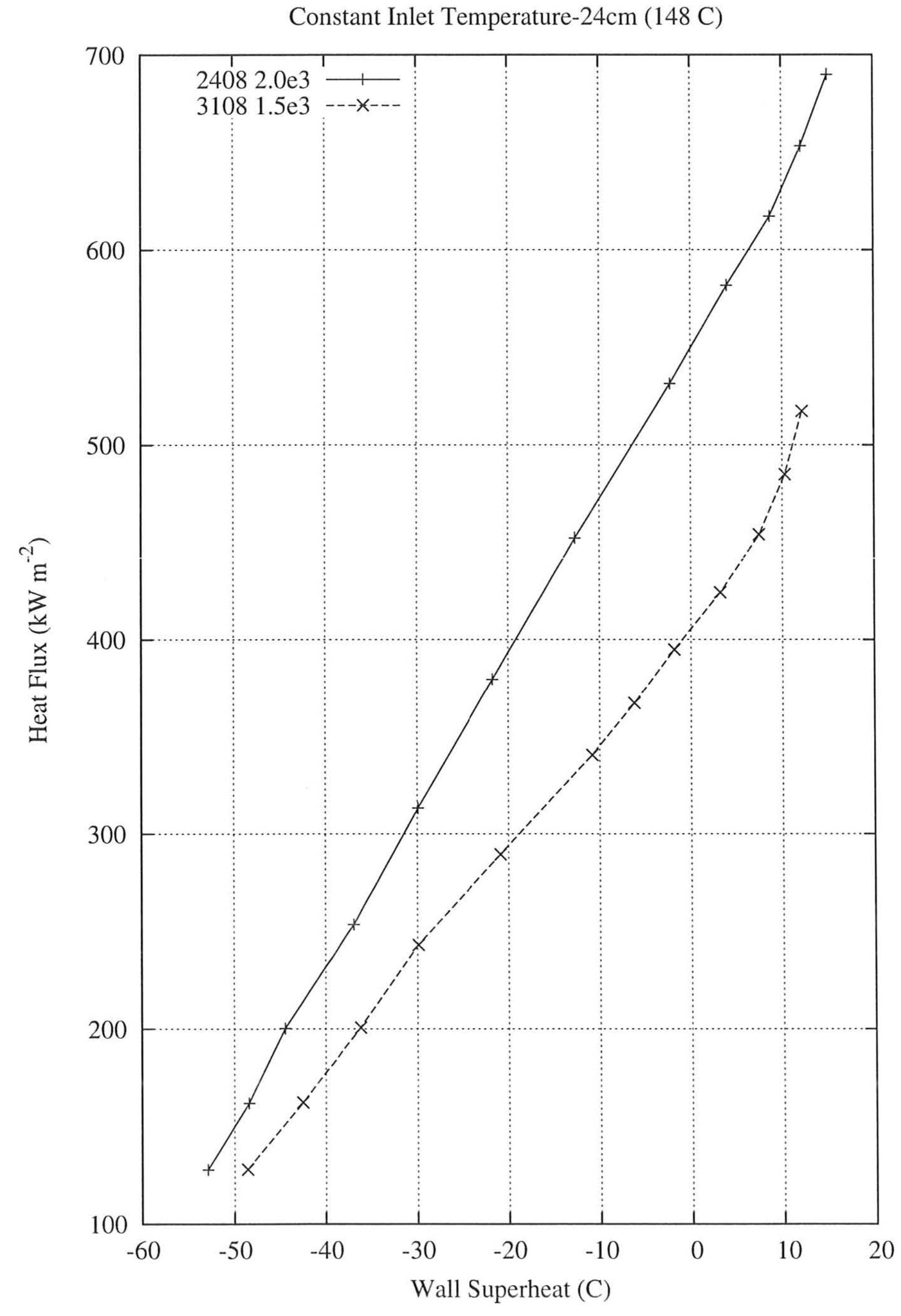

Figure B.20: Boiling curve for constant inlet temperature of 148°C, 24 cm from the TS outlet

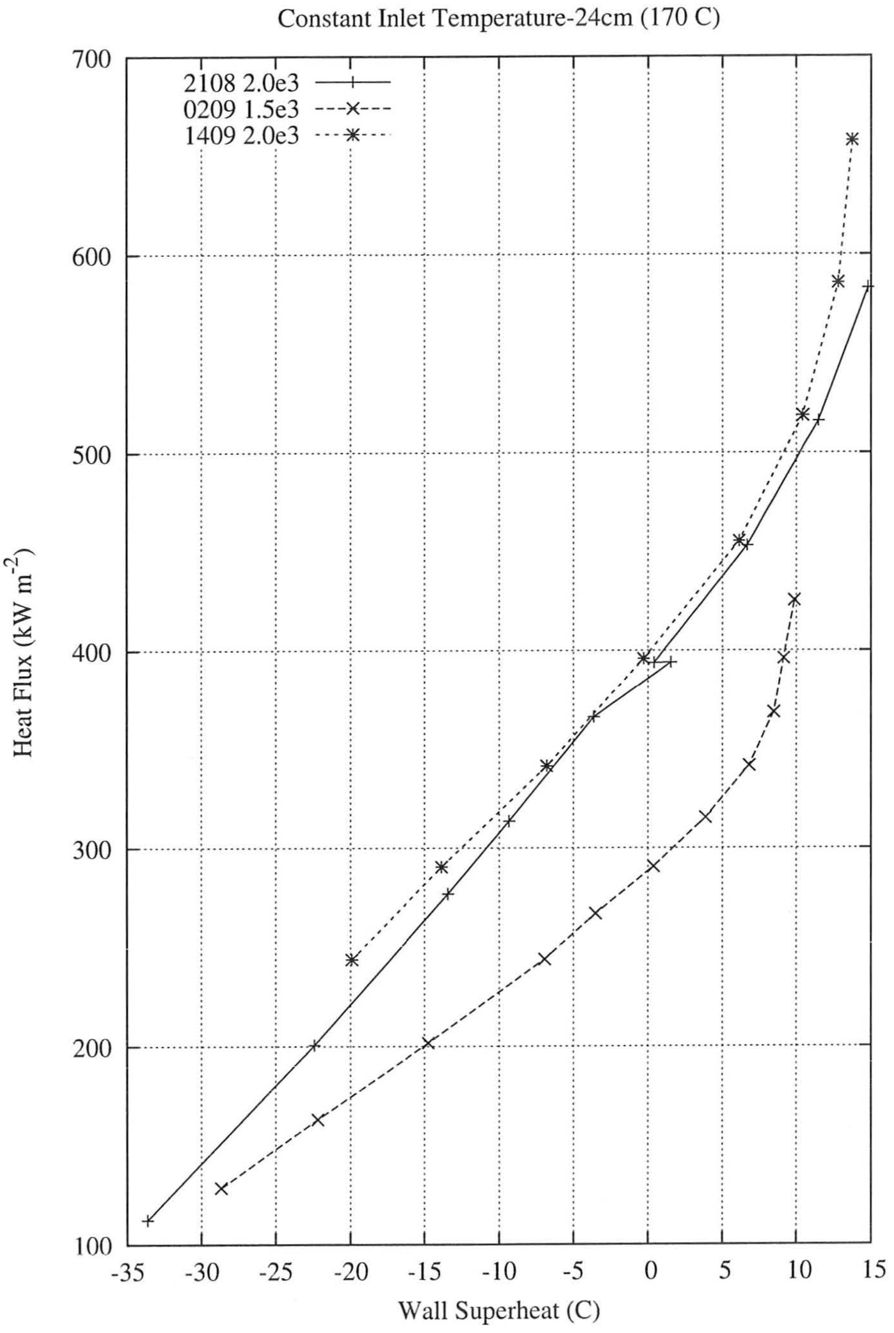

Figure B.21: Boiling curve for constant inlet temperature of 170°C, 24 cm from the TS outlet

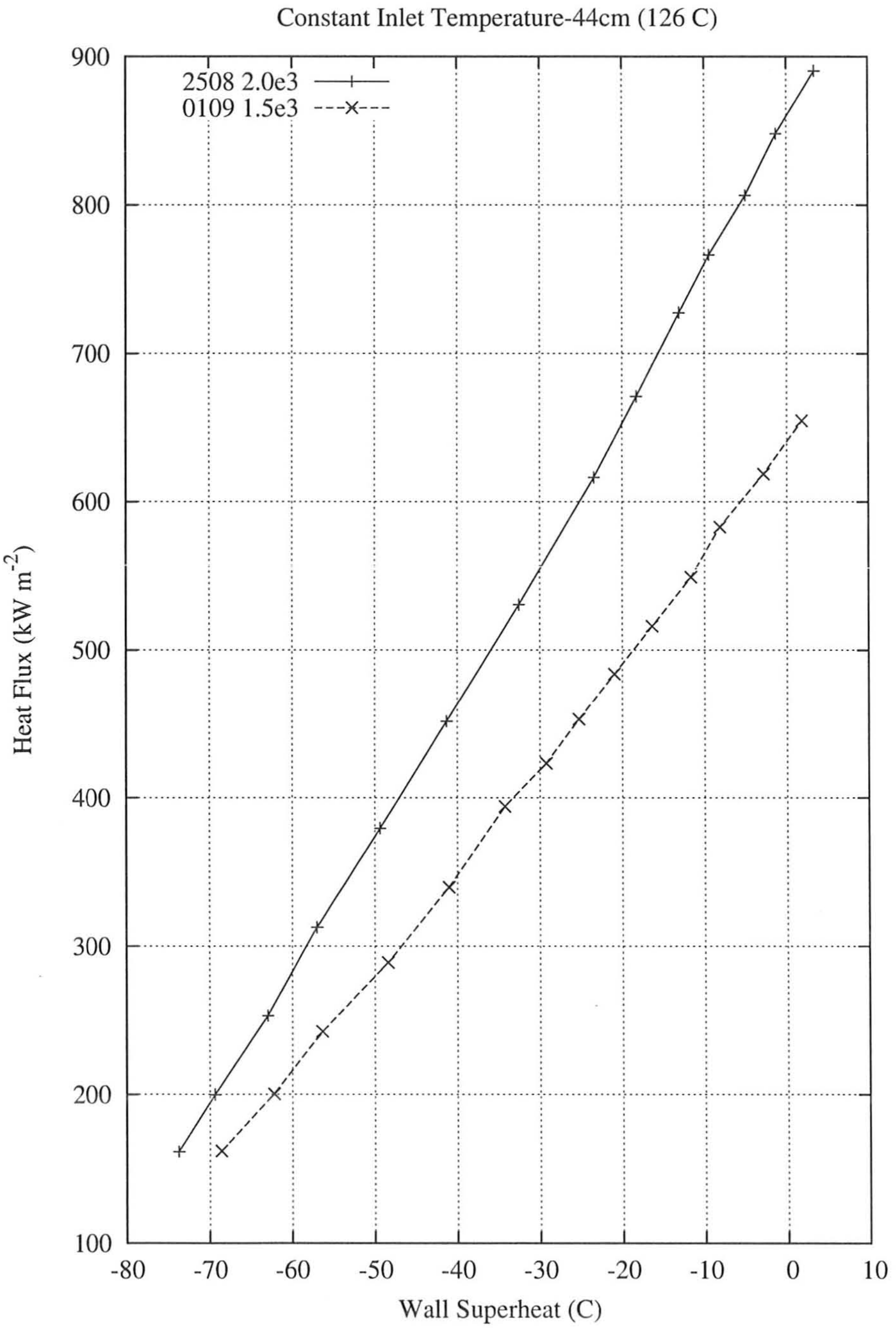

Figure B.22: Boiling curve for constant inlet temperature of 126°C, 44 cm from the TS outlet

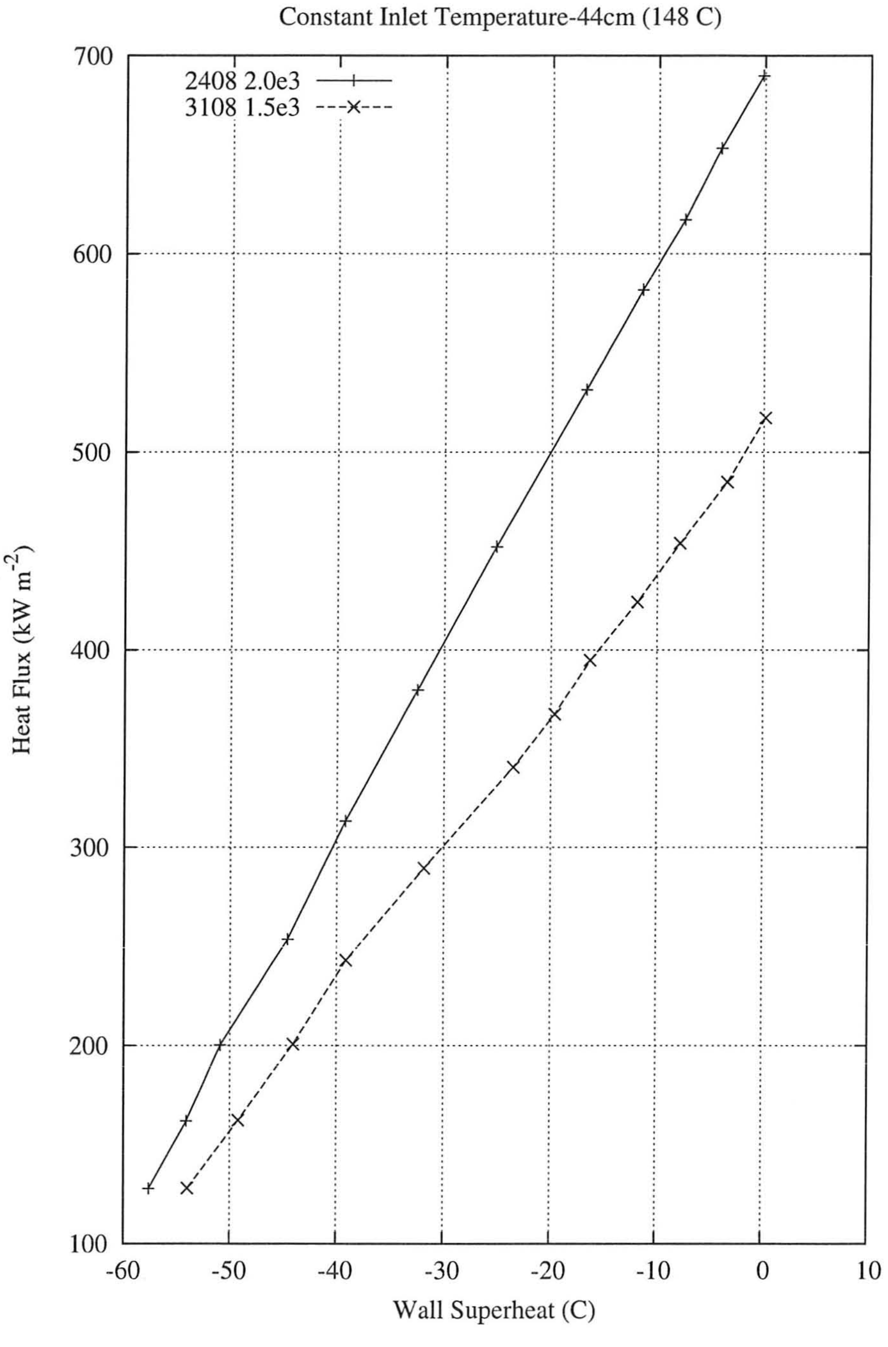

Figure B.23: Boiling curve for constant inlet temperature of 148°C, 44 cm from the TS outlet

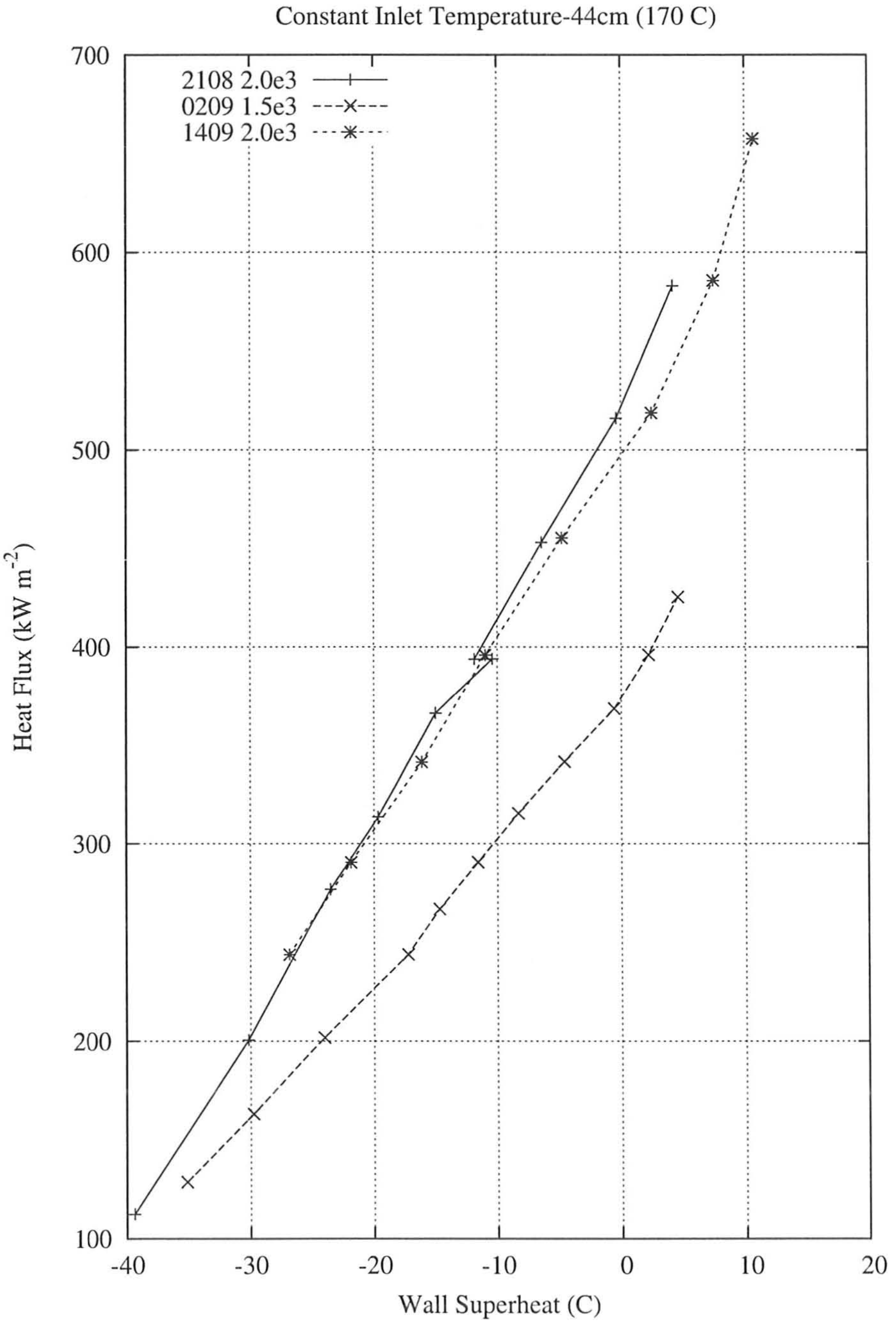

Figure B.24: Boiling curve for constant inlet temperature of 170°C, 44 cm from the TS outlet

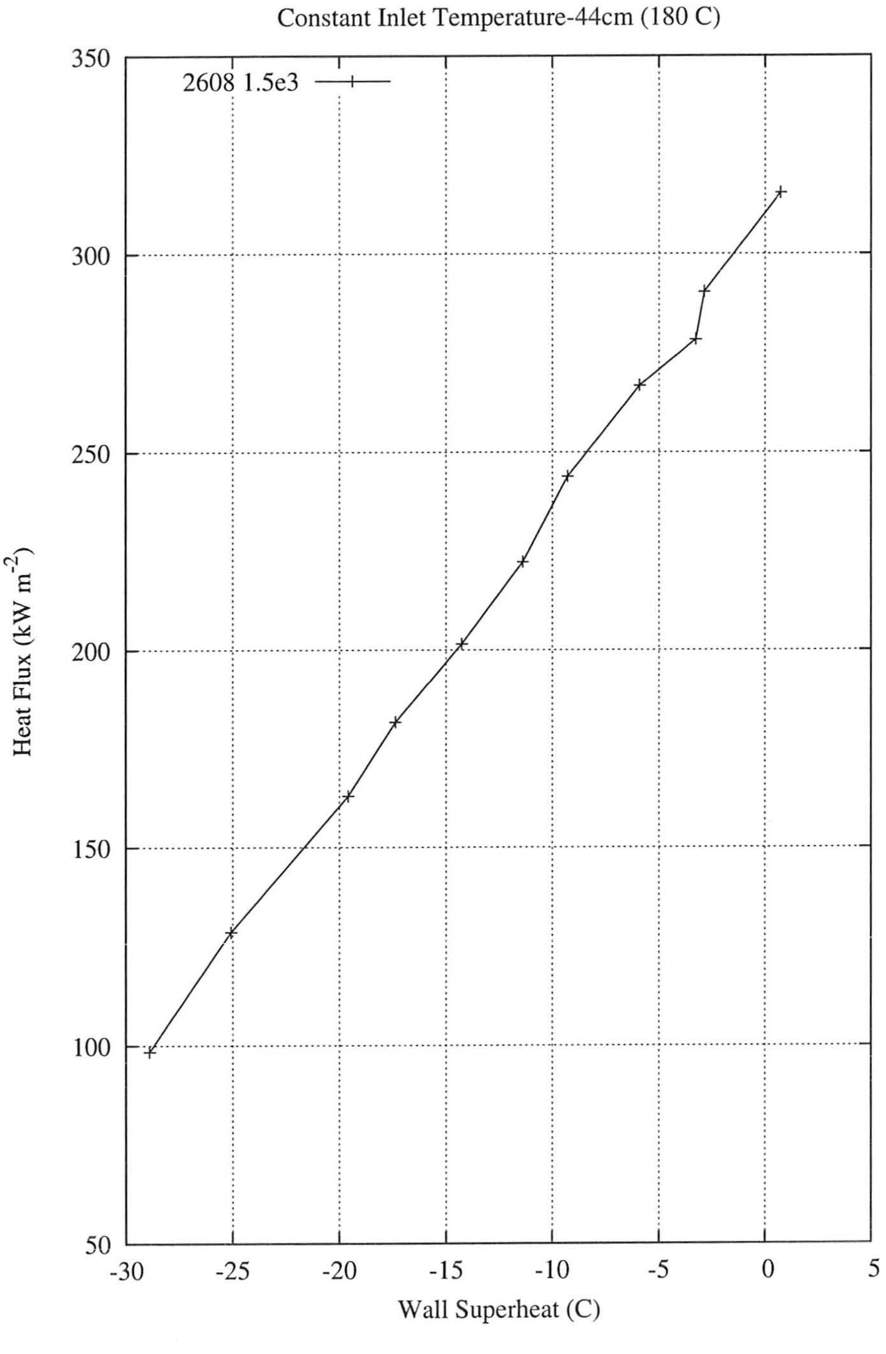

Figure B.25: Boiling curve for constant inlet temperature of 180°C, 44 cm from the TS outlet

B.4 Constant Mass Flux

This section contains figures that show the effect of inlet temperature on boiling heat transfer while keeping mass flux constant. Curves are plotted only for combinations of position and mass flux that were repeated for multiple inlet temperatures are shown.

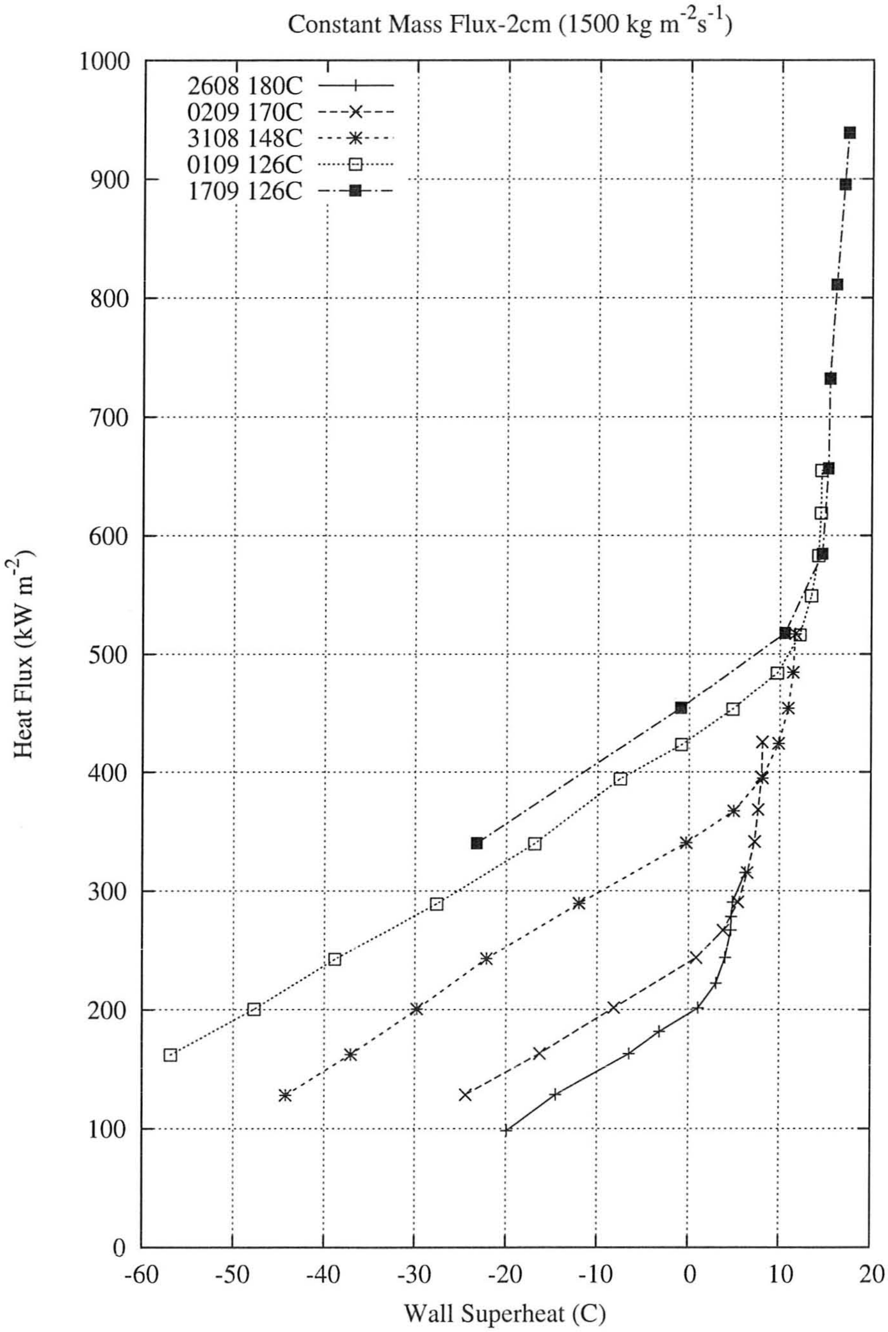

Figure B.26: Boiling curve for constant mass flux of 1500 kg m^{-2} s^{-1}, 2 cm from the TS outlet

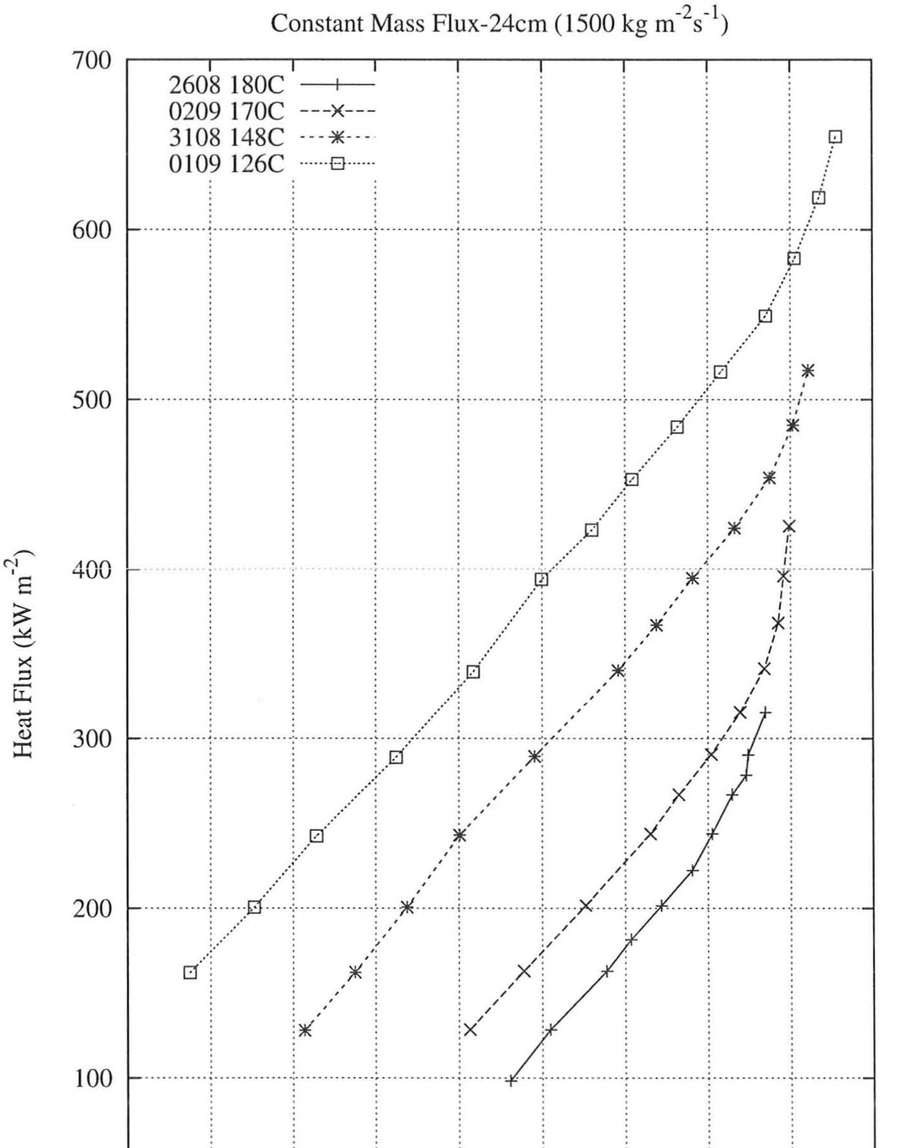

Figure B.27: Boiling curve for constant mass flux of 1500 kg m^{-2} s^{-1}, 24 cm from the TS outlet

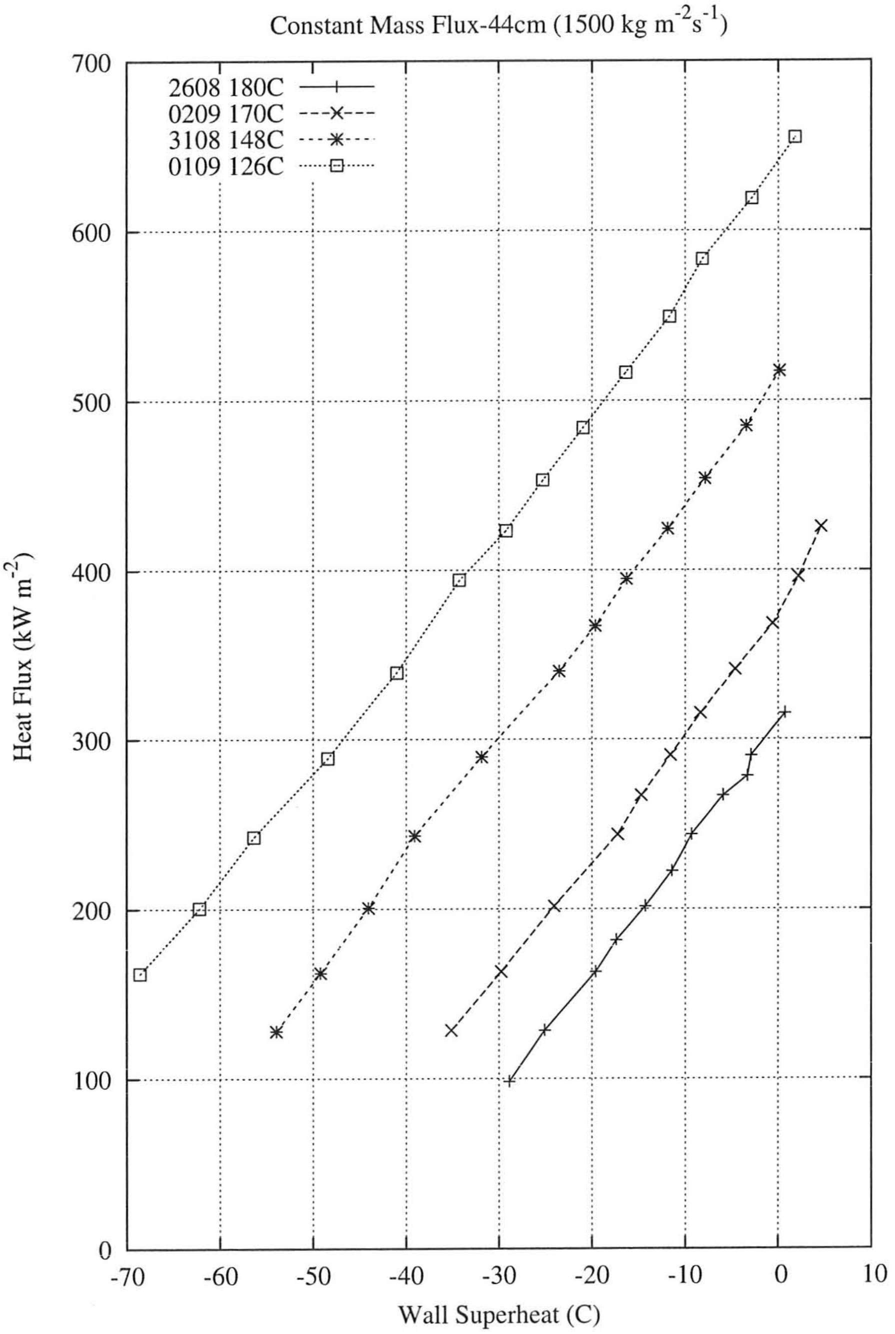

Figure B.28: Boiling curve for constant mass flux of 1500 kg m^{-2} s^{-1}, 44 cm from the TS outlet

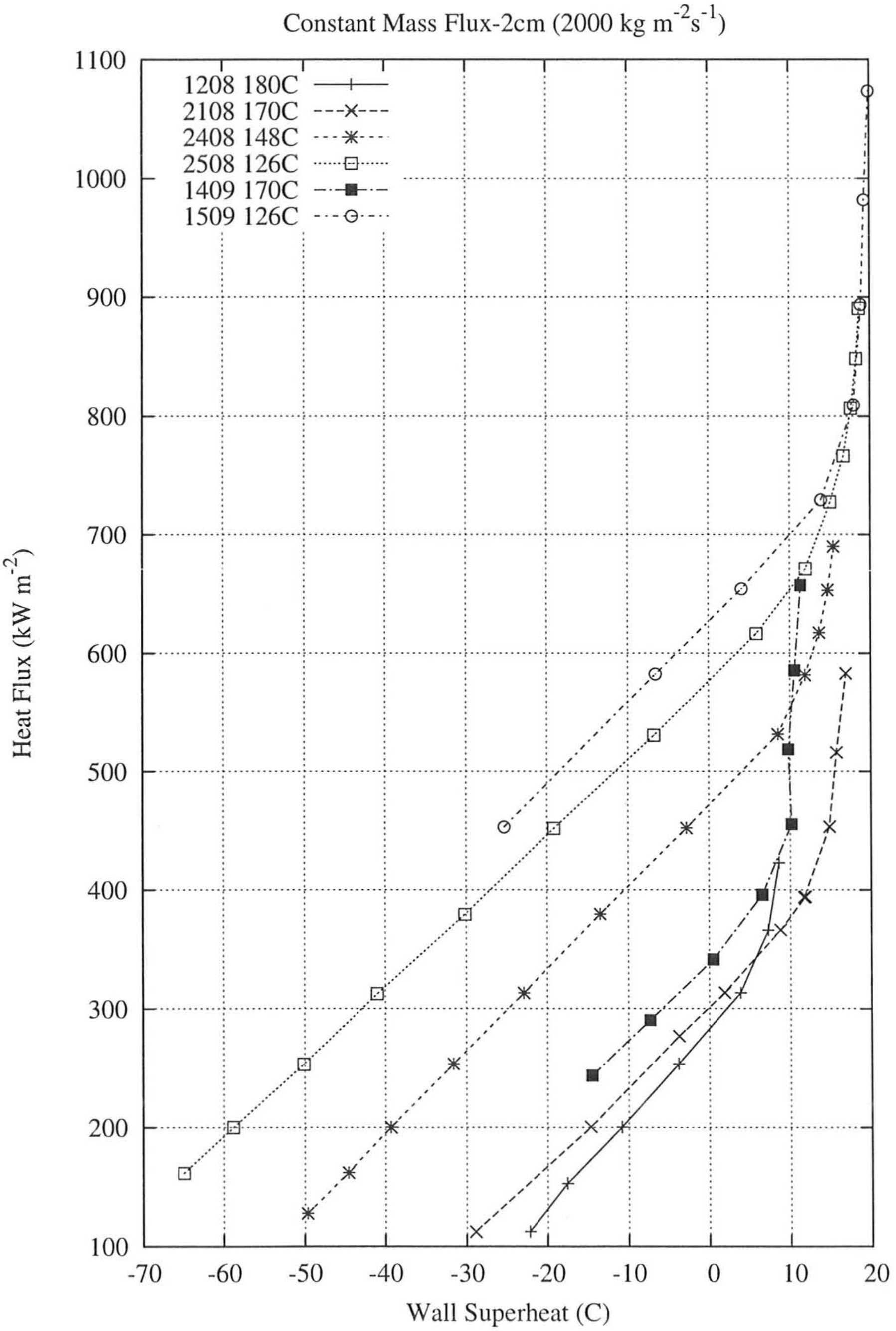

Figure B.29: Boiling curve for constant mass flux of 2000 kg m^{-2} s^{-1}, 2 cm from the TS outlet

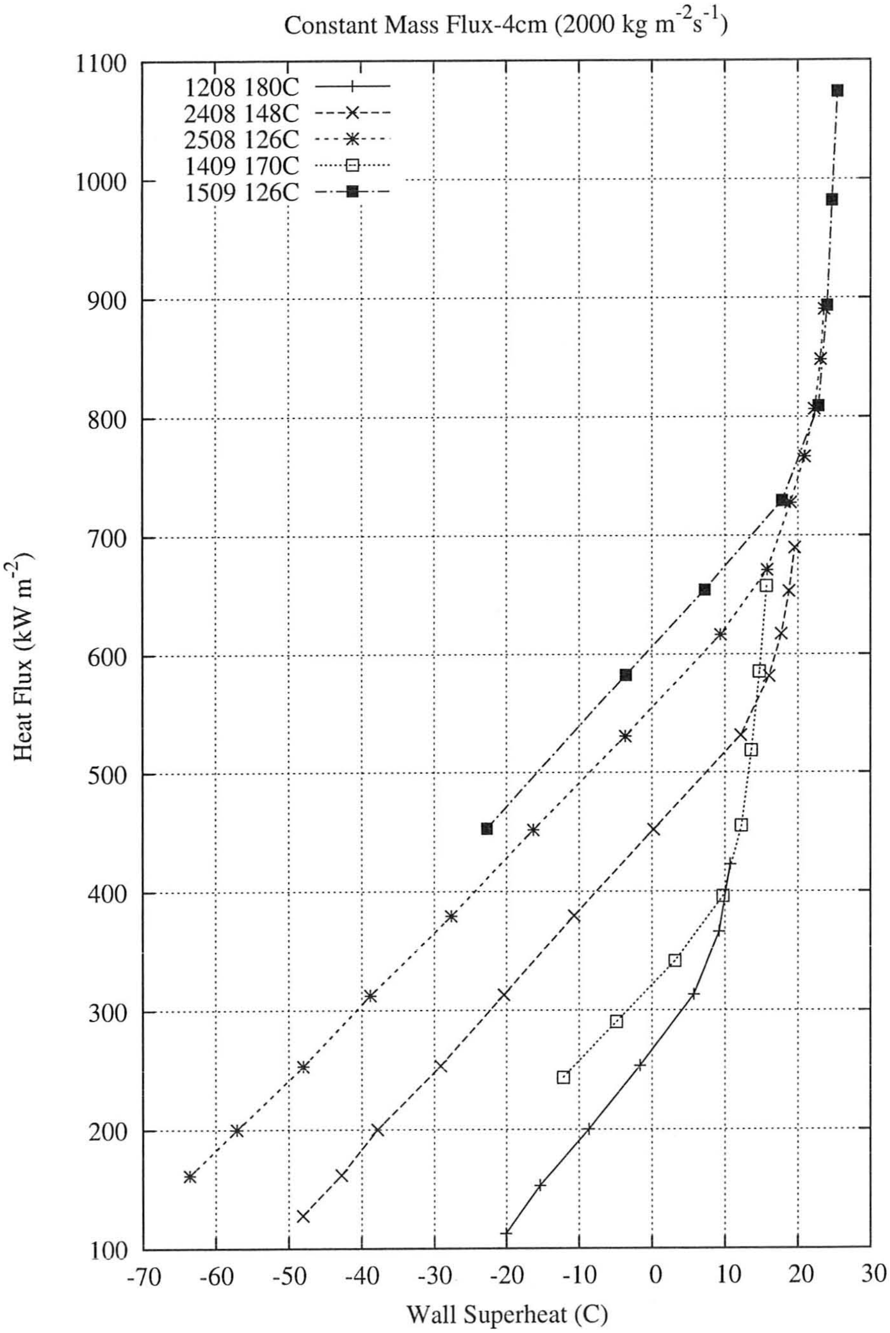

Figure B.30: Boiling curves for constant mass flux of 2000 kg m^{-2} s^{-1}, 4 cm from the TS outlet

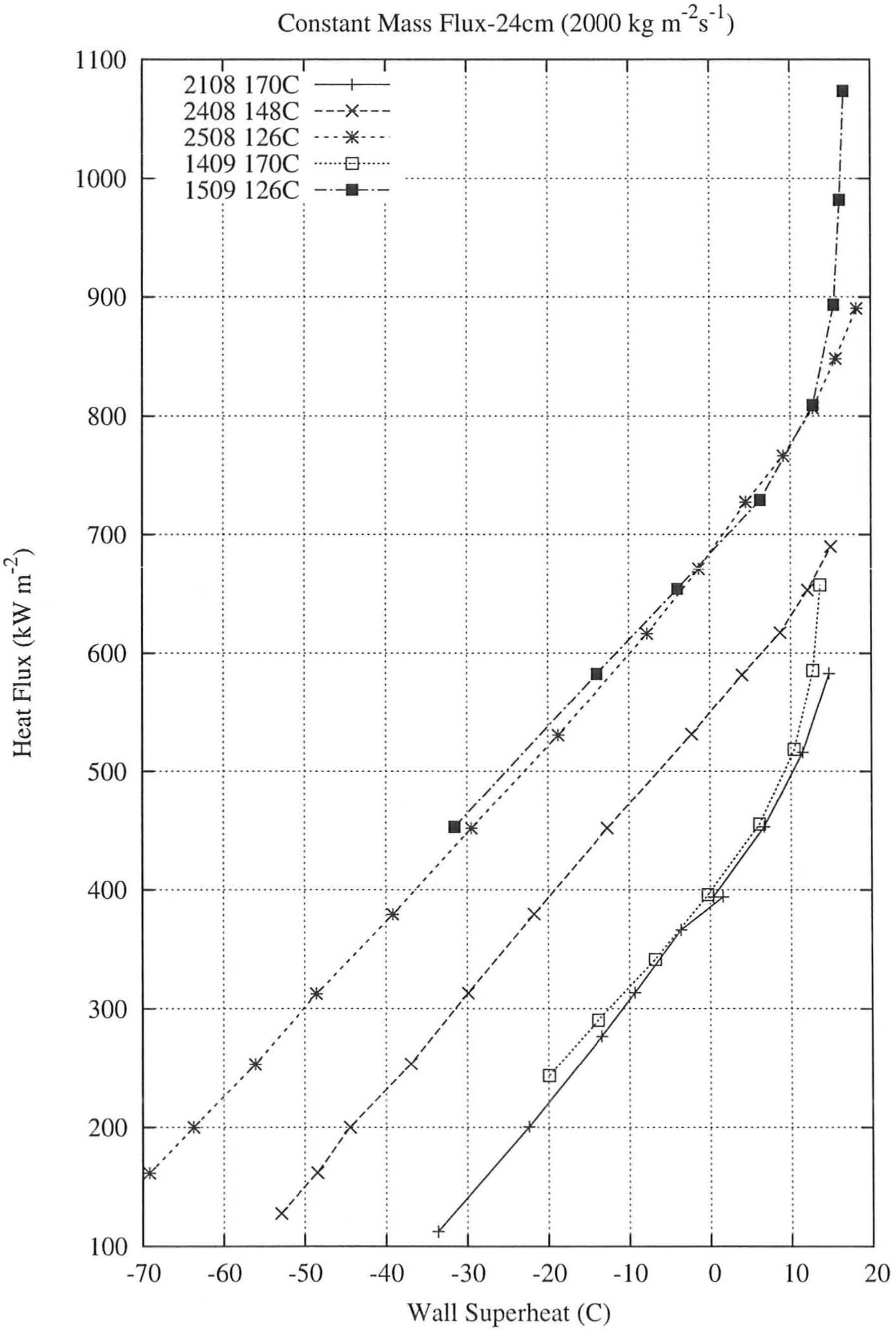

Figure B.31: Boiling curve for constant mass flux of 2000 kg m^{-2} s^{-1}, 24 cm from the TS outlet

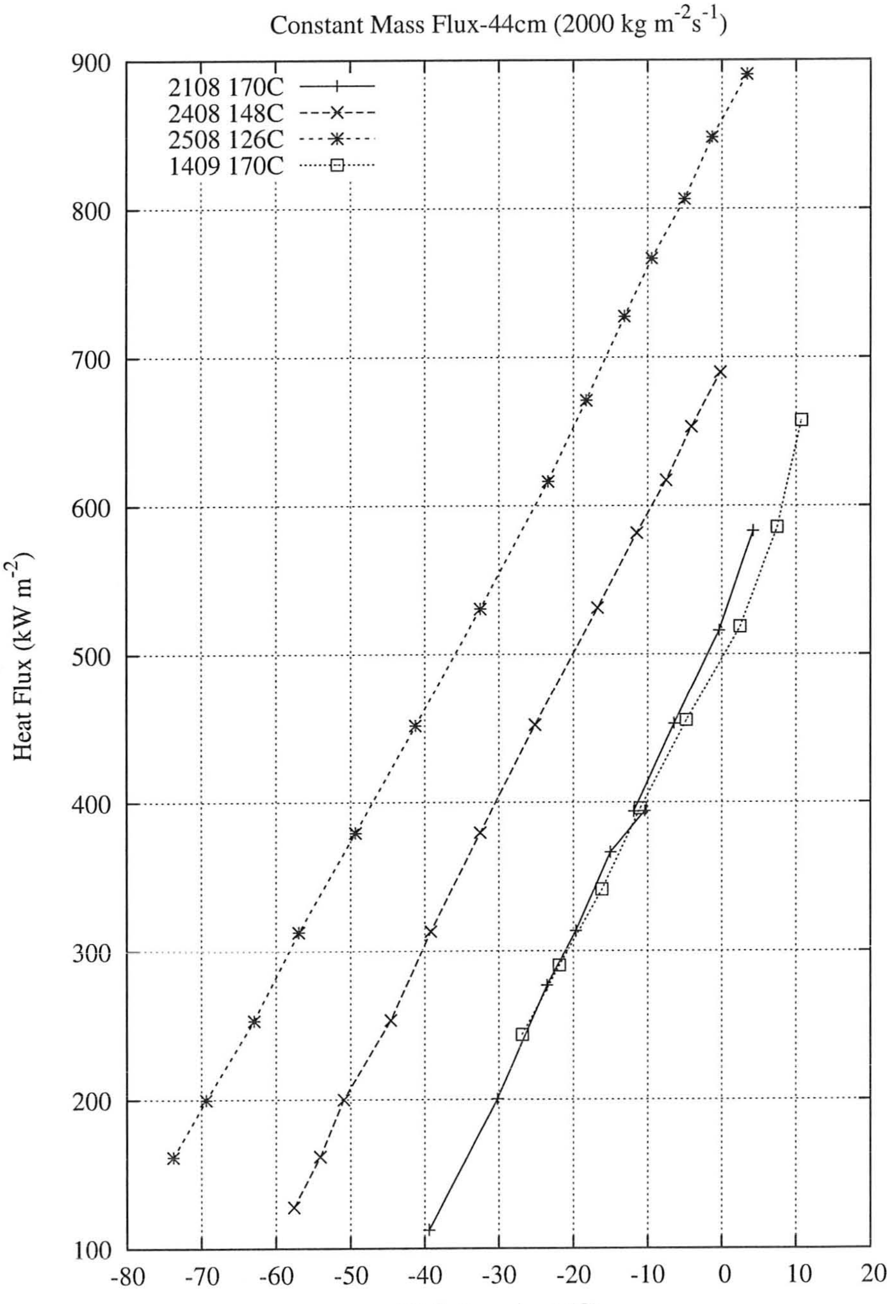

Figure B.32: Boiling curve for constant mass flux of 2000 kg m^{-2} s^{-1}, 44 cm from the TS outlet

Bibliography

[1] Yu. V. Polezhaev. Heat transfer in High Temperature (after 40 years). *High Temperature*, 41(5):563–570, 2003.

[2] Frank P. Incropera and David P. DeWitt. *Introduction to Heat Transfer*. John Wiley & Sons, third edition, 1996.

[3] Joseph A. Schetz. *Foundations of Boundary Layer Theory*. Prentice-Hall, 1984.

[4] Masatoshi Kureta, Toshiyuki Kobayashi, Kaichiro Mishima, and Hideaki Nishihara. Pressure drop and heat transfer for flow-boiling of water in small-diameter tubes. *JSME International Journal*, 41(4):871–879, 1998.

[5] Baduge Sumith, Fumito Kaminaga, and Kunihito Matsumura. Saturated flow boiling of water in a vertical small diameter tube. *Experimental Thermal and Fluid Science*, 27:789–801, 2003.

[6] A. Teyssedou, A. Olekhnowitch, A. Tapucu, P. Champagne, and D. Groeneveld. Critical heat flux in a vertical tube at low and medium pressures. *Nuclear Engineering and Design*, 149:185–194, 1994.

[7] A. Olekhnovitch, A. Teyssedou, A. Tapucu, P. Champagne, and D.C. Groeneveld. Critical heat flux in a vertical tube at low and medium pressures: Part I. experimental results. *Nuclear Engineering and Design*, 193:73–89, 1999.

[8] X. Cheng, F.J. Erbacher, and U. Müller. Critical heat flux in uniformly heated vertical tubes. *International Journal of Heat and Mass Transfer*, 40(12):2929–2939, 1997.

[9] Ra-Min Tain. *An investigation of CHF fluid-to-fluid scaling and multi-fluid prediction techniques*. PhD thesis, University of Ottawa, 1994.

[10] A. Tanase, S.C. Cheng, D.C. Groeneveld, and J.Q. Shan. Diameter effect on critical heat flux. *Nuclear Engineering and Design*, 239:289–294, 2009.

[11] John G. Collier and John R. Thome. *Convective Boiling and Condensation*. Oxford Science Publications, third edition, 1996.

[12] Van P. Carey. *Liquid-Vapor Phase-Change Phenomena*. Taylor & Francis, second edition, 2008.

[13] Phuong M. Le and Dimitrios V. Papavassiliou. A physical picture of the mechanism of turbulent heat transfer from the wall. *International Journal of Heat and Mass Transfer*, 52:4873–4882, 2009.

[14] Franz Ramstorfer, Helfried Steiner, and Günter Brenn. Modeling of the microconvective contribution to wall heat transfer in subcooled boiling flow. *International Journal of Heat and Mass Transfer*, 51:4069–4082, 2008.

[15] P. Saha and N. Zuber. Point of net vapor generation and vapor void fraction in subcooled boiling. In *Proceedings of the 5th International Heat Transfer Conference*, pages 175–179, Tokyo, Japan, 1974.

[16] Kaichiro Mishima and Marmoru Ishii. Flow regime transition criteria for upward two-phase flow in vertical tubes. *International Journal of Heat and Mass Transfer*, 27(5):723–737, 1984.

[17] J.R. Barbosa Jr., G.F. Hewitt, and S.M. Richardson. High-speed visualisation of nucleate boiling in vertical annular flow. *International Journal of Heat and Mass Transfer*, 46(26):5153–5160, 2003.

[18] V.V. Yagov. Generic features and puzzles of nucleate boiling. *International Journal of Heat and Mass Transfer*, 52(22):5241–5249, 2009.

[19] R.H.S. Winterton. Where did the Dittus and Boelter equation come from? *International Journal of Heat and Mass Transfer*, 41(4-5):809–810, 1998.

[20] B.S. Petukhov and V.N. Popov. Theoretical calculation of heat exchange and frictional resistance in turbulent flow in tubes of an incompressible fluid with variable physical properties. *High Temperature*, 1(1):85–101, 1963.

[21] V. Gnielinski. New equations for heat and mass transfer in turbulent pipe and channel flow. *International Chemical Engineering*, 16(2):359–368, 1976.

[22] J.P. Abraham, E.M. Sparrow, and J.C.K. Tong. Heat transfer in all pipe flow regimes: laminar, transitional/intermittent, and turbulent. *International Journal of Heat and Mass Transfer*, 52(3):557–563, 2009.

[23] A.E. Bergles and W.M. Rohsenow. The determination of forced-convection surface-boiling heat transfer. *ASME Journal of Heat Transfer*, 86:365–372, 1964.

[24] G. Guglielmini, E. Nannei, and Pisoni C. Survey of heat transfer in forced convection boiling. *Wärme- und Stoffübertr [Thermo- and Fluid Dynamics]*, 13(3):177–185, 1980.

[25] S.G. Kandlikar. Heat transfer characteristics in partial boiling, fully developed boiling, and significant void flow regions of subcooled flow boiling. *ASME Journal of Heat Transfer*, 120:395–401, 1998.

[26] S.G. Kandlikar. A general correlation for saturated two-phase flow boiling heat transfer inside horizontal and vertical tubes. *Journal of Heat Transfer*, 112(1):219–228, 1990.

[27] M.M. Shah. A general correlation for heat transfer during subcooled boiling in pipes and annuli. *ASHRAE Transactions*, 83:202–217, January 1977.

[28] John C. Chen. Correlation for boiling heat transfer to saturated fluids in convective flow. *Industrial and Engineering Chemistry Process Design and Development*, 5(3):322–329, 1966.

[29] V.V. Klimenko. A generalized correlation for two-phase forced flow heat transfer. *International Journal of Heat and Mass Transfer*, 31(3):541–552, 1988.

[30] Dieter Steiner and Jerry Taborek. Flow boiling heat transfer in vertical tubes correlated by an asymptotic model. *Heat Transfer Engineering*, 13(2):43–69, 1992.

[31] Sergio Edelstein, A.J. Pérez, and J.C. Chen. Analytic representation of convective boiling functions. *American Institute of Chemical Engineers Journal*, 30(5):840–841, 1984.

[32] D.C. Groeneveld, S.C. Cheng, L.K.H. Leung, and C. Nguyen. Computation of single and two-phase heat transfer rates suitable for water-cooled tubes and subchannels. *Nuclear Engineering and Design*, 114:61–77, 1986.

[33] K.E. Gungor and R.H.S. Winterton. A general correlation for flow boiling in tubes and annuli. *International Journal of Heat and Mass Transfer*, 29(3):351–358, 1986.

[34] M.M. Shah. Chart correlation for saturated boiling heat transfer: Equations and further study. *ASHRAE Transactions*, 88:185–195, January 1982.

[35] Idex Health & Science, Inc. Micropump series GC magnetic drive gear pump. `www.micropump.com/pdfs/literature/micropump_web_GC.pdf`.

[36] C.Y. Ho, Harold Mindlin, and William F. Brown Jr., editors. *Aerospace Structural Metals Handbook*, volume 4. CINDAS/Purdue University, 1992.

[37] Omega Engineering. High temperature cements. `http://www.omega.com/Temperature/pdf/OB_BOND_CHEM_SET.pdf`. Online document.

[38] D.R. Novog, S.T. Yin, and J.S. Chang. Recent advances in high heat flux smooth and swirl flow boiling of water. *Fusion Science and Technology*, 52:880–884, 2007.

[39] Philip R. Bevington and D. Keith Robinson. *Data Reduction and Error Analysis for the Physical Sciences*. McGraw-Hill, third edition, 2003.

[40] The RELAP5-3D Code Development Team. Relap5-3d code manual, vol. 4: Models and correlations, revision 2.4. `http://www.inl.gov/relap5/r5manuals/ver_2_4/vol4_v2_4.pdf`, 2005. Online document.

[41] Y. Taitel, D. Bornea, and A.E. Dukler. Modeling flow pattern transitions for steady upward gas-liquid flow in vertical tubes. *American Institute of Chemical Engineering Journal*, 26(3):345–354, 1980.

[42] D.R. Novog. High heat flux subcooled boiling heat transfer and pressure drop in a tubular channel under smooth– and swirl–flow conditions. Master's thesis, McMaster University, 1995.